Low-excess-noise AlInAsSb-based Avalanche Photodiodes for Mid-wave Infrared Detection

---

A Dissertation

Presented to

the faculty of the School of Engineering and Applied Science

University of Virginia

---

in partial fulfillment

of the requirements for the degree of

Doctor of Philosophy

by

Adam A. Dadey

December 2023

APPROVAL SHEET

This dissertation

is submitted in partial fulfillment of the requirements

for the degree of

Doctor of Philosophy

Author: ______________________

Adam A. Dadey

This dissertation has been read and approved by the following committee:

Advisor: Dr. Joe C. Campbell

Committee Chair: Dr. Andreas Beling

Committee Member: Dr. Kyusang Lee

Committee Member: Dr. Olivier Pfister

Committee Member: Dr. Xu Yi

Accepted for the School of Engineering and Applied Science:

Jennifer L. West, School of Engineering and Applied Science

December 2023

To my parents

Acknowledgements

First, I would like to thank my advisor, Joe C. Campbell. He is not only an excellent leader but a great teacher as well. No matter the situation, Joe would always find time to meet in person and discuss anything ranging from problems encountered in the lab to theoretical questions about device physics. I am incredibly fortunate to have had the chance to do a Ph.D. under the advisement of Joe.

Second, I would like to thank my committee members for their time in helping me with the proposal and defense of my dissertation. I hope to stay connected with them in my time after UVA.

Next, I thank my collaborators at the University of Texas at Austin. Collaborating one-on-one with a crystal grower is a unique situation, allowing for quick device turnaround and a level of understanding and precision unmatched by any of the big III-V foundries. Specifically, I thank J. Andrew McArthur and Stephen D. March for their hard work in growing all the devices presented in this thesis.

I want to thank the members of my research group for their friendship and support, particularly in preparation for the qualifying exam. In a particular way, I would like to thank a former member, Andrew H. Jones, for helping me get up to speed when I first joined the group and always being accessible to answer questions. Throughout my time at UVA, Andrew has not only been a great team member, but he has become a close friend. I would not be where I am today without his help, friendship, and memes.

I want to thank the members of the cleanroom staff who have maintained the Innovations in Fabrication facility here at UVA. Additionally, I would like to thank Chris Moore for his suggestions in the cleanroom and his friendship.

Finally, I thank my family for being there for me in the most challenging times when it felt like the easiest solution would be to give up. Their support and inspiration helped me stay levelheaded and focused on the important things in life.

Abstract

In optical receiver systems where the system noise is circuit-limited, avalanche photodiodes (APDs) offer a benefit compared to conventional photodiodes as their internal gain mechanism can lead to an improved system signal-to-noise ratio. The internal gain in APDs comes from the process of impact ionization in which high energy carriers collide with bound electrons within a crystalline material, liberating them to move freely within the lattice. However, this amplification process itself creates noise as it is stochastic. Therefore, the benefit of an APD is limited to the point at which its noise contribution begins to dominate the system.

Applications in the mid-wave infrared (MWIR) are particularly attractive for APDs as high sensitivity is often required to detect the low signal levels present in applications like space imaging or surveillance. In the MWIR, the dark current contribution to noise is particularly problematic as the thermal generation of carriers is high in the narrow bandgap materials required to absorb MWIR light. However, this problem can be relatively easily solved as the devices can be cooled to reduce the thermal generation component of the dark current, albeit at the cost of a physically larger receiver. The second main contributor to noise in the MWIR is the excess noise factor. In an optical receiver, the excess noise factor will fundamentally limit its sensitivity. Therefore, it is crucial to make the excess noise factor as small as possible. For my thesis, I have focused on reducing the detector's excess noise factor to improve receiver sensitivity.

In collaboration with the University of Texas at Austin, I have investigated several devices that fall into three regimes of excess noise: conventional single-carrier ionization ($k \sim 0$), heterojunction-dominated multiplication (excess noise factor ~ 1), and an intermediate between the two. I first started by examining four important considerations when measuring the excess noise of low k-factor materials, like AlInAsSb presented in this thesis. I then designed, fabricated, and characterized a $Al_{0.05}InAsSb$-based separate absorption, charge, and multiplication (SACM) APD for operation out to 3.5 µm. The device achieves a maximum gain of around 850 and has a unity-gain external quantum efficiency of 24% at 3 µm. It is the

first AlInAsSb-based APD capable of efficiently absorbing 3 μm light. The SACM APD has a k-factor of 0.04, meaning it falls in the single-carrier ionization regime of excess noise (regime 1).

In tandem, I experimentally measured the excess noise factor of 2- and 3-step staircase APDs at an operating frequency of 70 kHz. To do so, I first needed to develop a new noise measurement setup capable of operating in the kHz range. I also needed to develop a new measurement methodology for measuring the noise for the staircase APDs, as the one we typically use to characterize conventional APDs did not apply. At a gain of ~4 and ~7.5 for 2- and 3-step devices, respectively, their excess noise factors are near unity as theoretically predicted by Capasso and Teich.

To continue the investigation, I proposed a hybrid device combining the MWIR absorption of an SACM APD with the near-unity excess noise of a staircase APD. The device was designed jointly between our group at UVA and our collaborators at UT Austin. Growth was done at UT Austin. This hybrid "SACMcase" APD has a near unity excess noise factor at a gain of ~4, and it can absorb light out to 3 μm. At a gain of 4, the SACMcase has an excess noise factor nearly three times lower than that of commercial InGaAs/InP SACM APDs.

Finally, I fabricated and characterized a cascaded multiplier structure, combining a single-step staircase multiplier with a bulk conventional multiplier. The idea of this design is to achieve a larger gain than a single-step staircase APD (gain of 2) while maintaining the near-unity excess noise. This device was designed and grown by my collaborators at UT Austin. The resulting device had an excess noise factor of ~1.3 at a gain of ~6. Compared to 2- and 3-step staircase APDs, this device has a dark current density nearly four times lower.

Table of Contents

List of Figures

List of Tables

1 Introduction

1.1 Motivation

A photodiode is a semiconductor device that converts light into an electrical current. These devices work via the photovoltaic effect[a], in which an incoming photon is absorbed in the semiconducting material and converted into an electron and hole pair. Through either the built-in intrinsic or extrinsically applied electric field, these electrons and holes can be collected and form a photocurrent. One of the most straightforward structures is a PIN photodiode in which an intrinsically doped semiconductor is sandwiched between p-type and n-type doped semiconductors. Photodiodes are used for many applications such as telecommunications, spectroscopy, imaging[1], and even barcode scanning[2].

In such applications, the output signal from the photodiode needs to be amplified before it can be further processed. Typically, this amplification occurs with an external post amplifier using either a high-impedance field-effect transistor or a trans-impedance amplifier[3]. These amplifiers introduce a non-negligible noise to the receiving system that is often higher than the noise generated by a photodiode[3]. Therefore, the signal-to-noise ratio (SNR) of a receiver system is often capped by the circuit noise, not the photodiode noise. The SNR of a receiver is directly related to its maximum sensitivity[3], or the minimum incident light power it can detect.

In receivers that are circuit-noise limited, an avalanche photodiode (APD) can prove to be beneficial to the system SNR as APDs have an internal gain mechanism that can electrically boost the received optical signal. This internal gain comes from the process of impact ionization in which free carriers of sufficient energy, provided by a large electric field, can collide with bound electrons in the valence band, giving them enough energy to jump to the conduction band, creating an electron-hole pair. These new carriers can now freely move and gain energy, allowing the process to repeat. This repeating process can lead to an "avalanche" of free carriers, giving the avalanche photodiode its name's sake. In tandem with a

[a] Closely related to the photoelectric effect in which an absorbed photon ejects an electron out of a material.

conventional electronic amplifier, an APD can essentially provide "noise-free" gain in a receiver up until the point where its noise contribution surpasses the system circuit noise. Up to that point, an APD can boost the signal without significantly contributing to the system noise, increasing the system SNR and receiver sensitivity. Because of their ability to improve receiver sensitivity, APDs are used in many applications such as long-haul optical links[4], LIDAR systems[5,6], and confocal microscopy[7], to name a few.

For the highest sensitivity applications, APDs can be utilized as single photon counters with the ability, as the name suggests, to detect single photon light levels. These devices are called single photon avalanche diodes (SPADs) and have been subject to extensive research using Si[8–10] for operation in the visible spectrum (0.4 – 0.7 µm) and InGaAs/InP[11,12] for the short-wave infrared (SWIR) spectrum (0.9 – 1.7 µm). As for commercial products, recently, the company Canon announced a new 3.2 Megapixel camera sensor incorporating an array of Si SPADs targeted for high-precision monitoring systems[13]. They claim that the sensor can detect illuminations as low as 0.001 lux[13]. For reference, the illuminance of a full moon at night is ~0.25 lux[14], and the illuminance of starlight in the night sky is ~0.001 lux[14].

Many of the applications for APDs mentioned above occur in the visible and SWIR spectrum; however, detecting light in the mid-wavelength infrared (MWIR) spectrum (2 – 5 µm) is of growing interest for various scientific and military applications. The recent launch of the James Webb Space Telescope has sparked increased interest in MWIR space imaging due to its inclusion of multiple MWIR-capable detectors[15,16]. MWIR detection under 5 µm is useful in gas sensing systems for environmental monitoring. In particular, detecting water, methane, and ammonia is possible in the 3 – 3.5 µm range[17]. For military applications, MWIR detection is used for night vision systems[18].

In such applications with low signal levels, APDs can provide the added sensitivity required for their detection. However, in the MWIR, the dark current contribution to noise is particularly problematic as the thermal generation of carriers is high in the narrow bandgap materials required to absorb MWIR light. This problem can be relatively easily solved as the devices can be cooled to reduce the thermal generation component of the dark current, typically at the cost of a physically larger receiver. The second main contributor to noise in the MWIR, and all wavelengths in general, is the excess noise factor. In an optical receiver, the excess noise factor fundamentally limits its sensitivity[3]. Therefore, making the excess noise factor as small as possible is crucial. For my thesis, I have focused on reducing the detector's excess noise factor as a way to improve receiver sensitivity.

1.2 APD Noise

All of the previously mentioned applications for APDs rely on their noise contribution to be lower than the system noise such that their added noise has negligible impact on the system SNR. The process of impact ionization is stochastic and is incorporated into the shot noise through the excess noise, $F(M)$. The shot noise is described by

$$\langle i_{\text{shot}}^2 \rangle = 2q\left(I_{\text{photo,unity}} + I_{\text{dark,unity}}\right)\Delta f M^2 F(M) \tag{1}$$

where q is the elementary charge, M is the avalanche gain, $I_{\text{photo,unity}}$ and $I_{\text{dark,unity}}$ are the unmultiplied photo and dark current, and Δf is the system bandwidth. In its most general form, the excess noise factor can be represented by

$$F(M) = \frac{\langle M^2 \rangle}{\langle M \rangle^2} = 1 + \frac{\text{var}(M)}{\langle M \rangle^2} \tag{2}$$

where M is the gain. This quantity is the second moment of the gain, $\langle M^2 \rangle$, normalized by the mean gain squared, $\langle M \rangle^2$. It can also be represented by one plus the variance of the gain, $\text{var}(M)$, normalized by the mean gain squared, $\langle M \rangle^2$.

For the characterization of conventional APDs, it is common to represent the excess noise factor using the McIntyre local field model[19]

$$F(M) = kM + (1-k)\left(2 - \frac{1}{M}\right) \tag{3}$$

where k is defined as the ratio of β, the hole impact ionization coefficient, and α, the electron impact ionization coefficient, such that $k < 1$. As a note, if $\alpha > \beta$ for a given material, it is said to be electron-dominated; a material is said to be hole-dominated if the reverse is true, $\beta > \alpha$. Using this model, an ideal material would have a k-factor equal to zero, in which case the excess noise factor asymptotically approaches two with increasing gain. Physically, $1/\alpha$ and $1/\beta$ in an APD represent the average distance a carrier must travel before it gains enough energy to impact ionize. Figure 1.1 shows an example energy band diagram where $\alpha > \beta$.

Using (2), the excess noise factor is often plotted as a function of gain for different k values. The measured excess noise factor for a given device is usually plotted alongside these reference curves. A k-factor for a given device or materials system can be determined based on the reference curve it most closely follows. Figure 1.2 shows the k-factor for several common materials systems and reference curves for k=0 to k=1 in increments of 0.1. From the plot, Si has the best excess noise performance scaling as k= ~0.02, while Ge has poor excess noise performance, scaling as k= ~0.9 – 1. At a gain of 20, Si has an $F(M)$ of ~2, while Ge has an $F(M)$ of ~20, ten times higher. Looking at these values with respect to (1), holding all values the same except $F(M)$, it is clear that a Si APD is more desirable compared to a Ge one as the shot noise for a Si APD is an order of magnitude lower compared to a Ge one.

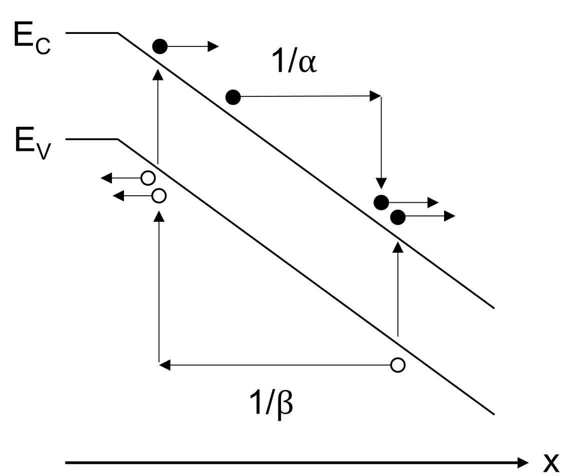

Figure 1.1: Illustration of the physical representation of α and β in an APD.

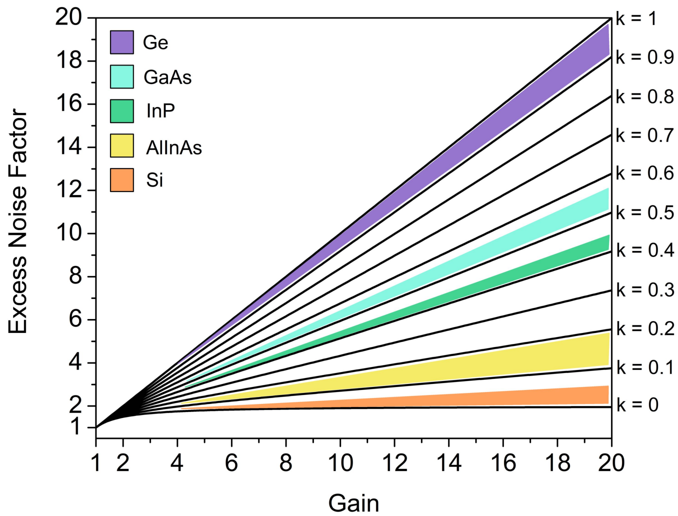

Figure 1.2: The excess noise factor versus gain for several common materials systems.

The signal-to-noise ratio of an APD can be expressed with the following equation incorporating the multiplied signal photocurrent in the numerator and the shot noise and thermal noise contributions in the denominator. In (4), the thermal noise, $\sigma_{\text{thermal}}^2 = 4k_B T \Delta f / R$, where k_B is Boltzmann's constant, T is temperature, and R is the APD series resistance.

$$\mathrm{SNR}_{\mathrm{APD}} = \frac{I_{\text{photo,unity}}^2 M^2}{2q\left(I_{\text{photo,unity}} + I_{\text{dark,unity}}\right)\Delta f M^2 F(M) + \sigma_{\text{thermal}}^2} \tag{4}$$

From (4), $I_{\text{dark,unity}}$ and $F(M)$ are the two terms that contribute significantly and can diminish the SNR of an APD, especially for MWIR detection, where the narrow bandgap materials required to absorb MWIR light have large dark currents due to thermal generation. The thermally generated dark current can be reduced by cooling the devices, often done with multi-stage thermoelectric or cryogenic coolers. For conventional APD structures, the excess noise factor is more or less intrinsic to the material used. However, more complicated structures can be designed to reduce the excess noise factor down to near unity. This thesis will introduce such structures existing below the k=0 lower limit described with the local field model.

1.3 Thesis Organization

This thesis describes my work on AlInAsSb-based APD devices with excess noise factors in three regimes: conventional single-carrier ionization ($k \sim 0$), heterojunction-dominated multiplication (excess noise factor ~ 1), and an intermediate between the two. Figure 1.3 highlights these three regimes. All devices presented are designed with MWIR operation in mind, either being able to absorb MWIR light directly or a building block toward a device that will be able to absorb MWIR light. Chapter 1 describes the motivation for this research as well as background on APDs and the $Al_xIn_{1-x}As_ySb_{1-y}$/GaSb materials system. Chapter 2 provides an overview of four considerations for measuring the excess noise factor of low k-factor materials. A low-frequency excess noise measurement setup is also introduced that was used to measure the excess noise factor of all the presented staircase-step-containing devices (Chapters 5, 6, and 7).

Chapter 3 highlights my characterization of $Al_{0.15}$InAsSb-based PIN photodiodes to gain useful information for my $Al_{0.05}$InAsSb-based SACM APD presented in Chapter 4. This SACM APD has a unity-gain external quantum efficiency of 24% for 3-µm light. The $Al_{0.05}$InAsSb-based SACM APD in Chapter 4 operates in Regime 1 of Figure 1.3. Chapter 5 demonstrates my work on the excess noise factor measurements of Staircase APDs. A near-unity excess noise factor was measured, agreeing with theoretical predictions[20,21]. Chapter 6 describes a hybrid SACM Staircase APD combining the near-unity excess noise of a staircase APD with the MWIR absorption of $Al_{0.15}$InAsSb. Devices from Chapters 5 and 6 operate in Regime 2 of Figure 1.3. Chapter 7 presents the characterization I performed on another staircase-step-containing hybrid device, this time cascading a 1-step staircase multiplier with a conventional high electric field bulk multiplier. The excess noise factor of this device falls into Regime 3 of Figure 1.3.

Chapter 8 summarizes the excess noise factor for all devices presented in the previous chapters. Chapter 9 concludes with two directions for future work in this area. Four appendices have also been provided with details on the device fabrication process, methods to reduce the dark current in $Al_{0.7}$InAsSb PIN APDs, information on the low-frequency noise setup, and select SEM images from my time at UVA.

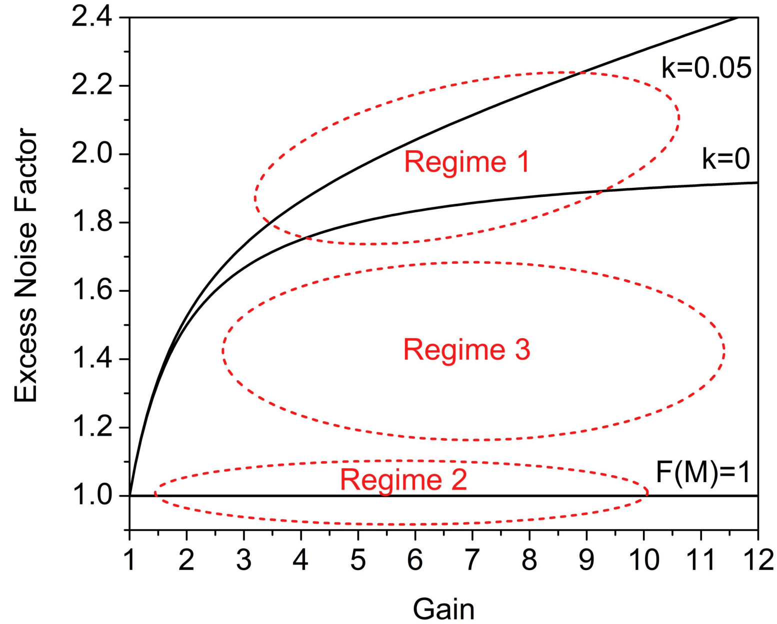

Figure 1.3: The three regimes of operation for the devices presented in this thesis. The $Al_{0.05}InAsSb$-based SACM falls in Regime 1. The 2- and 3-step staircase APDs, as well as the SACMcase APD fall in Regime 2. The cascaded multiplier APD resides in Regime 3.

1.4 Background

1.4.1 Current-voltage & Gain Characteristics

Current-voltage (I-V) measurements are frequently performed under two conditions: dark and light. Under no illumination (inside a dark box or with the room lights off), the dark current of an APD can be determined. After dark measurements, flood illumination with a lamp or, more frequently, focused laser illumination is used to measure the total current under illumination. This total current includes contributions from the light source and the dark current. Subtracting the total current and the dark current yields the photocurrent, the contribution of current that comes solely from photons converted to electrons. This resulting photocurrent is used to calculate the gain in an APD.

The onset of gain only occurs once a substantial electric field has built up in the depletion region of an APD. Because of this, depending on the thickness of the depletion region, there is often a range of reverse bias where the photocurrent is relatively flat. However, after a certain point, the photocurrent starts to increase. A simple method for calculating gain is to choose a point in this flat region and define it as "unity." That unity photocurrent represents a gain of one. Therefore, any photocurrent above unity is considered gain. While this method of calculating gain is simple, it is prone to error, which can affect further measurements, such as ones for the excess noise factor. Better approaches to calculating gain are discussed below in the APD Noise Considerations chapter. Figure 1.4 displays a sample I-V characteristic for a $Al_{0.7}InAsSb$-based PIN APD with a 1-µm thick unintentionally doped (uid) region. For the photocurrent curve, a large flat region is visible between -5 V and -25 V, and gain is visible past -30 V. A unity photocurrent was selected at -25 V and was used to calculate gain in the device. Also, in Figure 1.4, at a bias of -46, the dark current in the device drastically increases by several orders of magnitude. This phenomenon is known as breakdown and occurs at a material-specific electric field strength. For example, the breakdown field strength in $Al_{0.7}InAsSb$ is ~500 kV/cm.

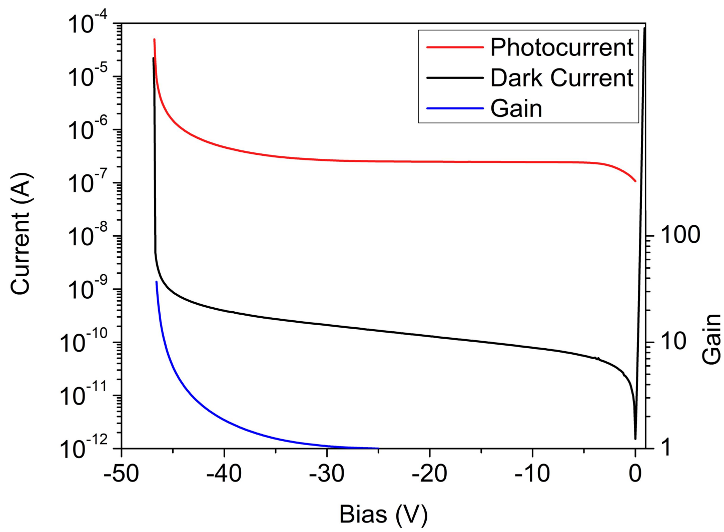

Figure 1.4: A sample current-voltage characteristic for a PIN APD under dark and light conditions. The gain is also calculated starting at -25 V. Device breakdown is visible at -46 V.

Another phenomenon that starts to occur at a characteristic electric field strength is band-to-band tunneling. This phenomenon occurs in narrow bandgap materials when electrons in the valence band can directly tunnel into the conduction band, where they can contribute to the dark current. In an I-V characteristic, band-to-band tunneling is identifiable by a distinctive "kink" in the dark current curve in which the slope of the dark current increases. Band-to-band tunneling is illustrated in Figure 1.5 at a bias of -5 V. It is undesirable to operate an APD when it has begun tunneling as the dark current exponentially increases with increasing bias.

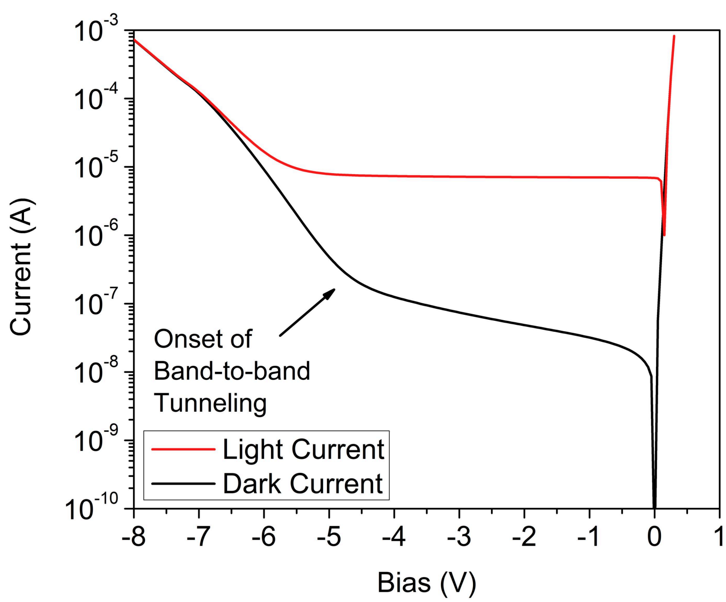

Figure 1.5: A current-voltage characteristic demonstrating band-to-band tunneling.

1.4.2 Capacitance-voltage Characteristics

Capacitance-voltage (C-V) curves are typically performed under dark conditions. This measurement is useful for determining if a particular device is fully depleted, and it can be used to estimate the doping concentration at a certain depletion width. Figure 1.6(a) shows a sample C-V characteristic for a $Al_{0.7}InAsSb$-based PIN APD with a 1-µm thick uid region. This capacitance measurement was performed at 1 MHz. The device is fully depleted around -4 V when the C-V curve has flattened. The depletion width can be calculated using a parallel plate capacitor model,

$$C = \frac{\varepsilon_r \varepsilon_0 A}{W} \rightarrow W = \frac{\varepsilon_r \varepsilon_0 A}{C} \tag{5}$$

where C is capacitance, ε_r is the material-specific relative permittivity, ε_0 is the permittivity of free space, A is device area, and W is the depletion width. The device area can be measured with a microscope, and the experimentally determined relative permittivity of $Al_{0.7}InAsSb$ is ~13.9. The calculated depletion width is also depicted in Figure 1.6(a).

The doping concentration versus depletion width can be calculated using the following equation[22]

$$N(W) = \frac{-2}{q\varepsilon_r \varepsilon_0}\left(\frac{d(1/C_j^2)}{dV}\right)^{-1} \approx \frac{-2}{q\varepsilon_r \varepsilon_0}\left(\frac{\Delta(1/C_j^2)}{\Delta V}\right)^{-1} \tag{6}$$

where $N(W)$ is the doping concentration at a given depletion width, q is the elementary charge, C_j is the area-normalized capacitance, and V is the applied voltage. Using this equation, the doping concentration versus depletion width was calculated and plotted in Figure 1.6(b). From the plot, the uid doping concentration is ~5x10^{15} cm^{-3}, and the contact doping is ~1x10^{18} cm^{-3}.

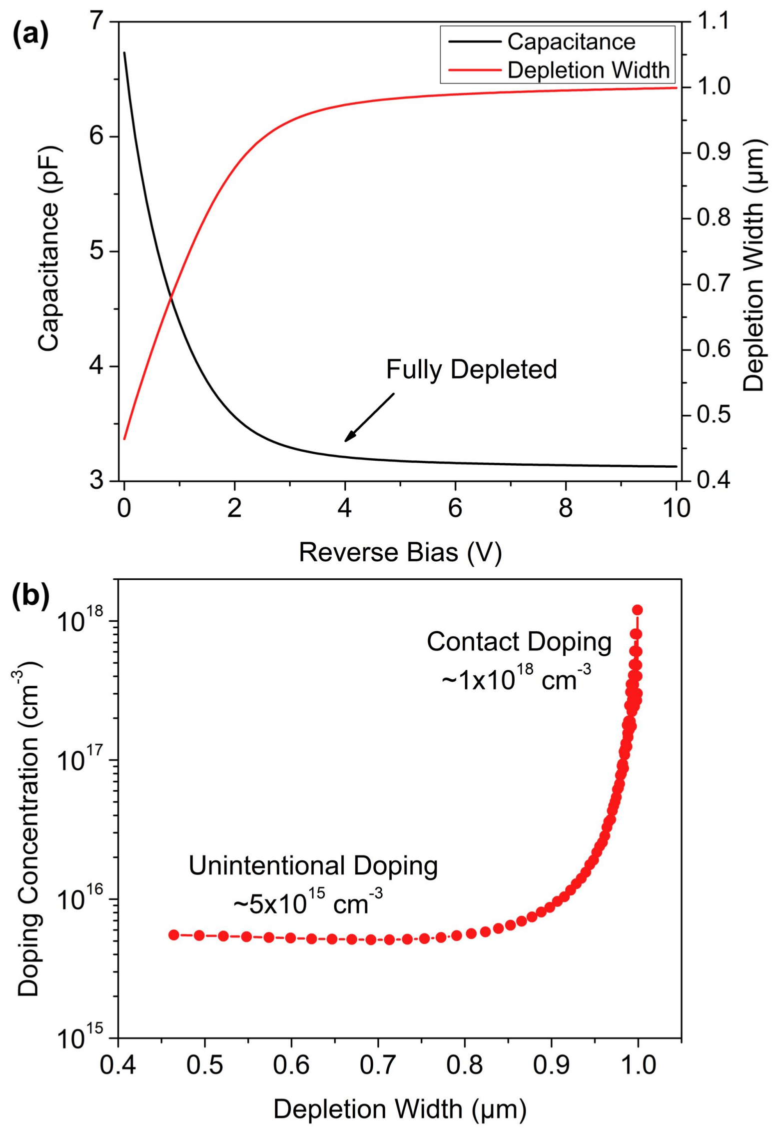

Figure 1.6: (a) A capacitance-voltage characteristic with the calculated depletion width determined from the parallel plate capacitor model. (b) The calculated doping concentration from the C-V in (a).

1.4.3 Quantum Efficiency Measurements

Quantum efficiency is a metric used to characterize how efficient a photodiode is at converting photons into electron-hole pairs. Quantum efficiency is typically measured in terms of internal quantum efficiency (IQE), how efficient a detector is at converting photons that have entered the device into electron-hole pairs, and external quantum efficiency (EQE), how efficient a detector is at converting incident photons into electron-hole pairs. The expression for IQE, η_{int}, is as follows:

$$\eta_{\mathrm{int}} = \xi(1 - \exp(-\alpha W)) \tag{7}$$

where ξ is the fraction of electron-hole pairs collected before recombining, α is the material-specific absorption coefficient, and W is the thickness of the depletion region. External quantum efficiency is similar in form to IQE, except the loss due to surface reflections is introduced. The expression for EQE, η_{ext}, is as follows:

$$\eta_{\text{ext}} = (1 - R)\eta_{\text{int}} = (1 - R)\xi(1 - \exp(-\alpha W)) \quad (8)$$

where R is the reflectance. For normal incident light, $R = (n_\lambda - 1)^2/(n_\lambda + 1)^2$, where n_λ is the refractive index of the absorbing material at a given wavelength. Typically, EQE is determined by first measuring the responsivity, $\Re$, of a photodiode. Responsivity is the ratio of the output photocurrent to the incident light power. It can be determined at a given bias by dividing the measured photocurrent by the measured incident light power. With the responsivity, the EQE can be calculated with the following expression:

$$\eta_{\text{ext}} = \frac{\Re}{\lambda}\frac{hc}{q} \quad (9)$$

where λ is the wavelength of light, h is Planck's constant, c is the speed of light, and q is the elementary charge. With the EQE, the IQE can then be calculated by dividing the EQE by one minus the reflectance, $\eta_{\text{int}} = \eta_{\text{ext}}/(1 - R)$. Figure 1.7 shows the measured EQE and calculated IQE for a $Al_{0.3}InAsSb$-based PIN photodiode with a 1-µm thick uid region.

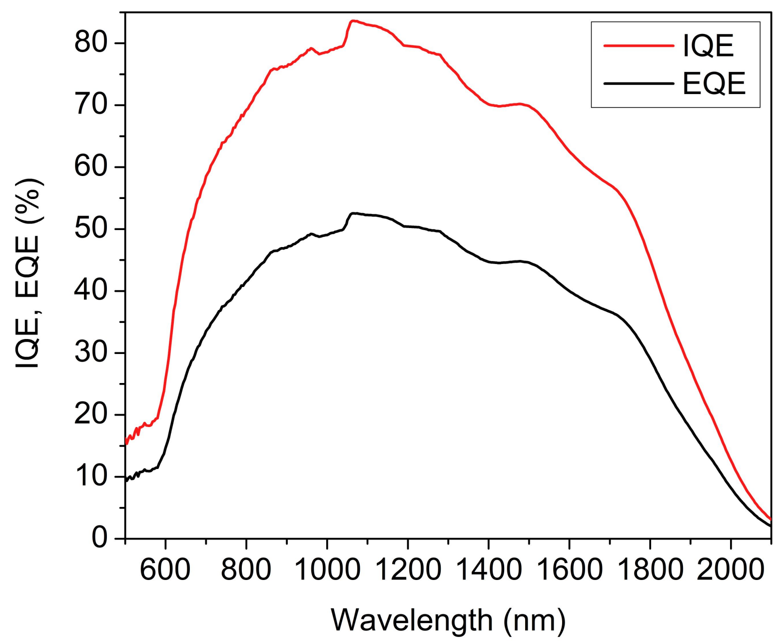

Figure 1.7: The measured external quantum efficiency and calculated internal quantum efficiency of a $Al_{0.3}InAsSb$-based PIN photodiode with a 1-µm thick uid region. The measurement was made at a bias in which the device was fully depleted.

One method for measuring the EQE of a photodiode over a broad spectrum is using a broad-spectrum lamp and a monochromator. Such a setup is used in our lab when measuring the EQE of a device under test (DUT). The monochromator allows a narrow sliver of the broad spectrum (~4 nm) to be reflected and shined on the DUT surface. However, the light from the broad-spectrum lamp is first passed through a long-pass filter to remove higher-order harmonics that would also get reflected on the monochromator's grating and shined on the DUT. The light reflected from the monochromator is focused through a chopper wheel into an optical fiber so it can be illuminated on the DUT. The chopper wheel is attached to a lock-in amplifier that measures the photocurrent of the DUT at a given wavelength. The EQE of the DUT, $\eta_{\mathrm{ext,DUT}}$, is determined by comparing its photocurrent to that of a calibrated detector with a known EQE using the following equation:

$$\eta_{\mathrm{ext,DUT}} = \eta_{\mathrm{ext,cal}} \frac{I_{\mathrm{photo,DUT}}}{I_{\mathrm{photo,cal}}} \tag{10}$$

where $\eta_{\mathrm{ext,cal}}$ is the known EQE of the calibrated detector, $I_{\mathrm{photo,DUT}}$ is the measured photocurrent of the DUT at a given wavelength, and $I_{\mathrm{photo,cal}}$ is the measured photocurrent of the calibrated detector at the same wavelength.

1.4.4 Variable Area Diode Analysis

Variable Area Diode Analysis (VADA) is a technique that can be used to determine the bulk and surface dark current densities for a set of fabricated devices. An accurate understanding of the bulk and surface contributions allows for more accurate predictions of dark current for different-sized devices, especially if a material is prone to having a significant surface leakage current contribution. To perform this analysis, I-V curves for several different-sized devices need to be measured. At each desired bias point, the dark current in a photodiode can be expressed with the following equation[23,24]:

$$I_{\mathrm{dark}} = J_{\mathrm{bulk}}\pi\left(\frac{d}{2}\right)^2 + J_{\mathrm{surface}}\pi d \tag{11}$$

where J_{bulk} is the bulk current density, J_{surface} is the surface leakage current density, and d is the device diameter. To illustrate the utility of this technique, I performed a VADA on a $Al_{0.3}InAsSb$-based PIN photodiode. Figure 1.8 shows I-V curves for several different-sized devices used to perform the analysis.

Using (11), I fitted values for J_{bulk} and J_{surface} by taking a cross-section of Figure 1.8 at a given bias and plotting the diameter current versus diameter. An example fit is shown in the inset of Figure 1.8. The resulting fitted values for J_{bulk} and J_{surface} are plotted versus bias in Figure 1.9(a). Using these fitted values at a specific voltage, the dark current contributions from bulk and surface leakage can be plotted versus diameter. Such a plot is helpful as it illustrates the range of diameters where a given device is bulk current limited or surface leakage current limited. This plot is shown in Figure 1.9(b), where the crossover diameter or 54 µm is labeled. Below 54 µm, the device is surface leakage current dominant, and above the device is bulk current dominant.

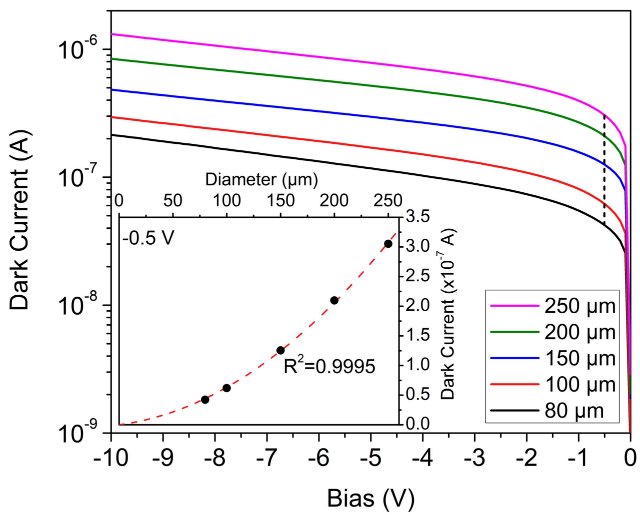

Figure 1.8: Current-voltage characteristics for several different diameter $Al_{0.3}InAsSb$-based PIN photodiodes. The inset shows a sample fitting of (11) by taking a cross-section of the I-V curves at -0.5 V.

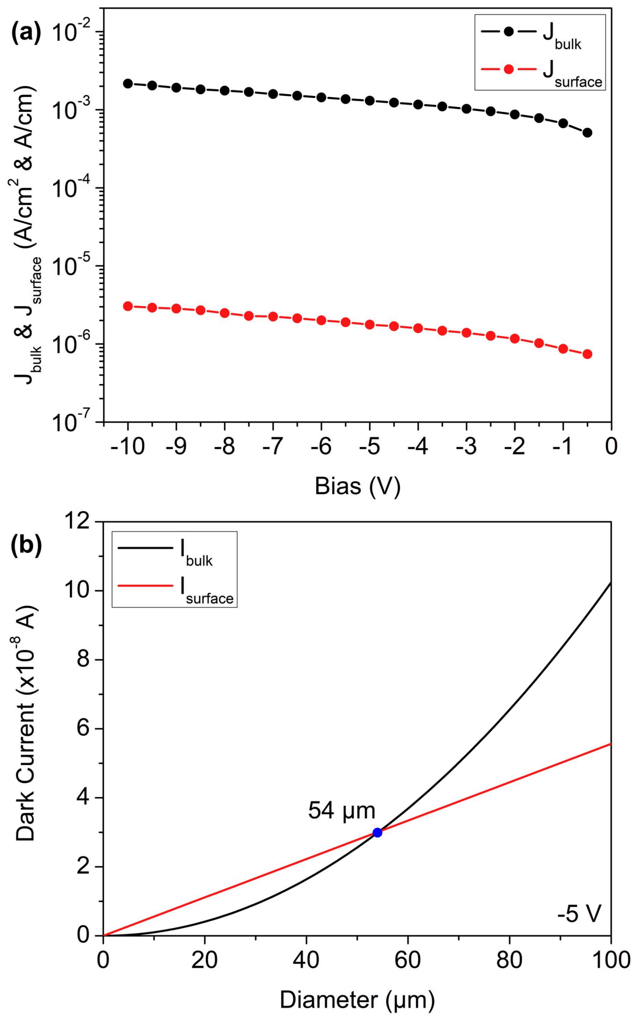

Figure 1.9: (a) The fitted values from J_{bulk} and J_{surface} for the I-V curves in Figure 1.8. (b) The bulk and surface-leakage current contributions versus device diameter at -5 V with the crossover point between the two contributions indicated at a diameter of 54 μm.

1.4.5 Bandwidth

The bandwidth in an APD describes how quickly it can respond to incoming signals. A typical figure of merit for APDs, and many devices in general, is the 3-dB bandwidth, $f_{3\text{dB}}$, or the frequency in which the output signal is half the input signal (attenuated by 3 dB). The two main limiting factors on the bandwidth of an APD are its RC time constant and transit time. The RC bandwidth, f_{RC}, can be represented by

$$f_{\text{RC}} = \frac{1}{2\pi RC} = \frac{W}{2\pi(R_{\text{s}} + R_{\text{L}})\varepsilon_r \varepsilon_0 A} \tag{12}$$

where R_{S} and R_{L} are the series and load resistances, respectively, and C is the junction capacitance that can be represented by (5). For f_{RC}, a thicker device yields a higher bandwidth as the capacitance drops. The transit time bandwidth, f_{t}, can be represented by

$$f_{\text{t}} = \frac{v_{\text{s}}}{2W} \tag{13}$$

where v_{s} is the material-specific average saturation velocity for electrons and holes. For f_{t}, a thinner device yields a higher bandwidth as the carriers travel a shorter distance. Accounting for both contributions, the 3-dB bandwidth can be approximated as the following:

$$f_{3\text{dB}} \approx \left(\frac{1}{f_{\text{RC}}^2} + \frac{1}{f_{\text{t}}^2}\right)^{-\frac{1}{2}}. \tag{14}$$

1.4.6 Excess Noise Factor Measurements

The excess noise factor of an APD can be measured using a Noise Figure Analyzer (NFA) with a setup depicted in Figure 1.10. With this setup, a bias tee provides an isolated DC bias to the APD and couples the RF signal to the NFA. With an NFA, the noise power of the APD is measured relative to a calibrated noise source. The relative noise power of an APD is measured under dark and illumination conditions at a given operating frequency (typically 50 MHz for our group). The relative noise power contribution from the photocurrent can be obtained by subtracting the dark relative noise power from the illuminated relative noise power. At a sufficiently low bias where there is unity gain, and thus unity excess noise, the measured noise power, N_0, represents the terms $2qI_{\mathrm{photo,unity}}\Delta f$ in (1). Subsequent noise measurements at higher reverse bias with gain, N_{gain}, represent the terms $2qI_{\mathrm{photo,unity}}\Delta f M^2 F(M)$ in (1). The excess noise factor in an APD can be calculated by dividing N_{gain} and N_0 and solving for $F(M)$. More information on measurement techniques, as well as several important considerations when measuring excess noise, are discussed in the APD Noise Considerations chapter below.

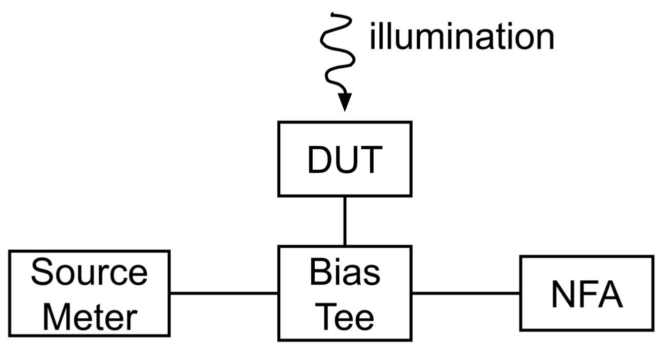

Figure 1.10: Noise-figure-analyzer-based setup for measuring the excess noise factor of APDs.

1.4.7 Separate Absorption, Charge, and Multiplication APD Structures

A separate absorption, charge, and multiplication (SACM) structure can be used to decouple the absorption and multiplication in an APD device. This structure is useful as it alleviates band-to-band tunneling issues that plague narrow bandgap materials required to absorb MWIR light. In an SACM, the intermediate charge layer establishes an electric field profile that is high in the multiplier, promoting impact ionization and low in the absorber, reducing the impact of band-to-band tunneling. Optionally, a grading layer can be added between the charge and absorption region that allows for a smooth transition between the narrow bandgap absorber and the wide bandgap multiplier. Without a grading region, abrupt steps in the energy bands will form that act as a barrier for electrons traveling from the absorber into the multiplier.

Incorporating a grading layer is not always possible, as the intermediate bandgap materials must maintain the same lattice constant as the substrate to ensure proper growth without dislocations.

Additionally, the effectiveness of the grading layer depends on how smooth of a grade is achievable. A constant linear grade is the most desirable, but it can be practically challenging to grow. Smooth grading regions can be approximated by dividing the region into several steps. While barriers between the steps will still be present, it will be easier for electrons to traverse compared to one large energy barrier.

A note on the naming convention of these structures. More correctly, our group typically designs separate absorption, grading, charge, and multiplication (SAGCM) structures. However, we usually drop the G in the abbreviation. It is also common to refer to these structures as separate absorption and multiplication (SAM) structures. SAM, SACM, and SAGCM structures are all distinct, but it is common to just refer to them as SAM structures (pronounced “sam”) as this is the easiest to say.

Figure 1.11(a) shows the electric field strength and energy band diagram for a simple PIN APD structure where absorption and multiplication happen in the same region. The n-contact (n), unintentionally doped (uid), and p-contact (p) regions are labeled. Figure 1.11(b) shows the electric field strength and energy band diagram for an SACM APD structure. The n-contact (n), multiplication (M), charge (C), grading (G), absorption (A), and p-contact (p) regions are labeled. Two distinct regions are visible, distinguished by the higher field in the multiplication region and the lower field in the absorption region. For both plots, the electric field is plotted at an arbitrary bias greater than zero, and the energy band diagram is under zero bias.

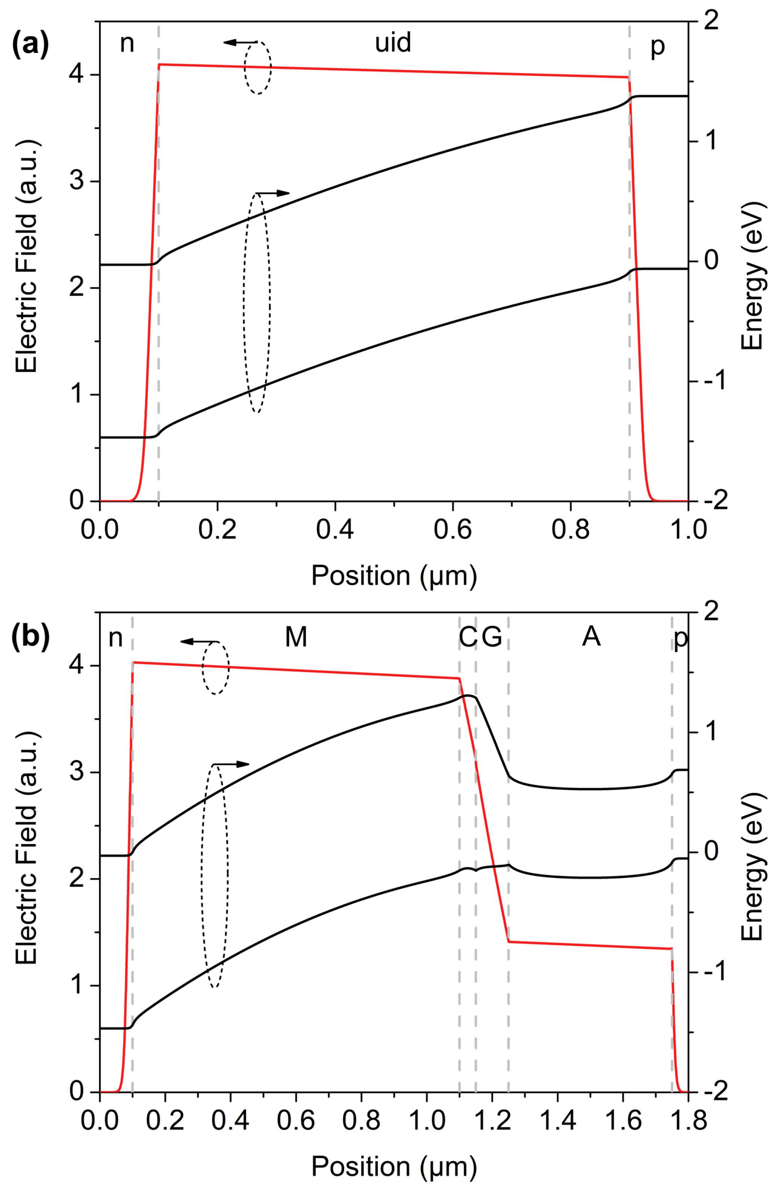

Figure 1.11: (a) The electric field strength and energy band diagram of a simple PIN APD with the n-contact (n), unintentionally doped (uid), and p-contact (p) regions labeled. (b) The electric field strength and energy band diagram of a SACM APD with the n-contact (n), multiplication (M), charge (C), grading (G), absorption (A), and p-contact (p) regions labeled. The electric field is plotted at an arbitrary bias greater than zero, and the energy band diagram is plotted under zero bias.

Figure 1.12 shows a sample I-V characteristic for an SACM APD structure under dark conditions and illumination. The significant increase in dark current and total current at -15 V is known as "punch-through," as the device has depleted through the intermediate charge region into the absorption region. The dark current increases due to the increase in thermally generated carriers in the narrow bandgap absorber. The total current increases because photogenerated electrons in the absorber can travel through the multiplication region and get collected. The increasing curvature in the total current curve indicates multiplication is occurring; breakdown is visible just past -19 V.

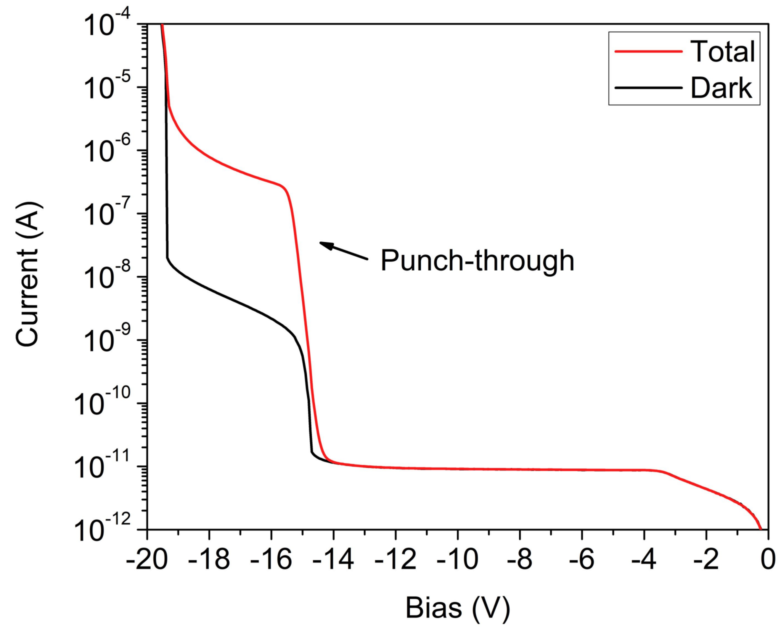

Figure 1.12: A sample I-V characteristic of an SACM APD structure under dark conditions and illumination. Punch-through has been labeled.

Figure 1.13 shows a sample C-V characteristic for an SACM APD structure, the same structure as in Figure 1.12. The initial drop in capacitance before 2 V reverse bias occurs because the device has depleted through the multiplication region. The region from 2 V to 13 V reverse bias is where the device is depleting through the intermediate charge region. The onset of punch-through is visible around 14 V reverse bias. The capacitance quickly drops after punch-through as the device continues depleting through the absorber. The capacitance levels off around 18 V reverse bias, indicating the device is fully depleted.

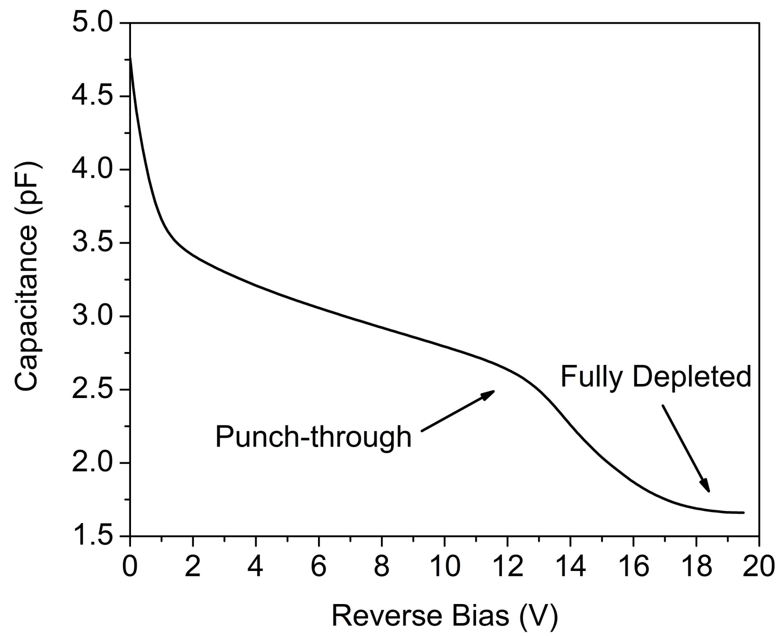

Figure 1.13: A sample C-V characteristic for an SACM APD structure. Punch-through and full depletion have been labeled.

The final main calculation for an SACM APD structure is gain and excess noise, both of which are valid after punch-through has occurred. From the I-V in Figure 1.12, it would be simple to claim that unity gain occurs at ~ -15.5 V once the photocurrent has leveled off. However, there is clearly a positive slope suggesting some level of gain is already present. This is usually the case in an SACM structure where a sufficient field has built up in the multiplication region at punch-through such that the photocurrent has a non-unity gain. This non-unity gain can be calculated by performing an excess noise factor measurement and fitting the resulting measurement to the local field model.

In Figure 1.14, the raw results of such a measurement are displayed in black. The device measured was biased to a point just after punch-through, and, for the purpose of the initial noise measurement, that point is chosen to be a gain of one. Subsequent points were at higher reverse biases until the device entered breakdown. As displayed in the plot, the excess noise scales linearly below k=0, and it appears that only a max gain of ~3 was reached, even though the device was about to break down. This measured excess noise can be corrected by fitting it to (3). Using this fit, the actual value for the gain and k-factor can be obtained. The red points in Figure 1.14 represent the corrected excess noise factor versus gain for the raw black points. From the plot, the actual gain value at the first bias point is ~5.3, and the excess noise factor of the device scales with a k of ~0.04. This technique is explained in greater detail in a previous publication[25].

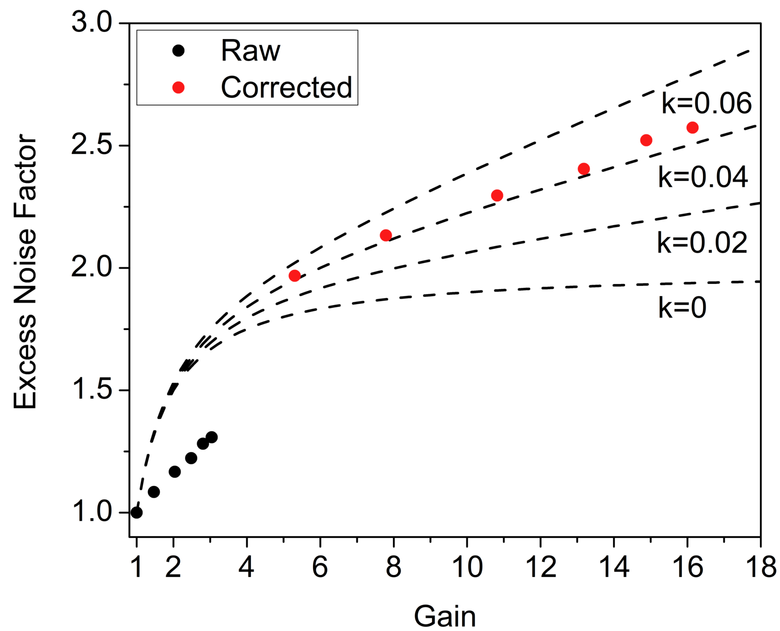

Figure 1.14: The raw and corrected excess noise factor of an SACM APD structure.

1.4.8 $Al_xIn_{1-x}As_ySb_{1-y}$ Materials System

The $Al_xIn_{1-x}As_ySb_{1-y}$ (Al_xInAsSb, or AlInAsSb) materials system grown on GaSb traditionally grown as a random alloy is limited to Al concentrations less than 6% due to a large miscibility gap for higher concentrations[26]. Recently, though, our collaborators at the University of Texas at Austin have grown this material up to Al concentrations of 80% using a digital alloy growth technique[27]. This growth is achieved via Molecular Beam Epitaxy (MBE) by repeatedly growing thin layers of the four binary constituents (AlAs, AlSb, InAs, InSb). Figure 1.15 shows a transmission electron microscope (TEM) image highlighting the four binaries and their repeating pattern[27].

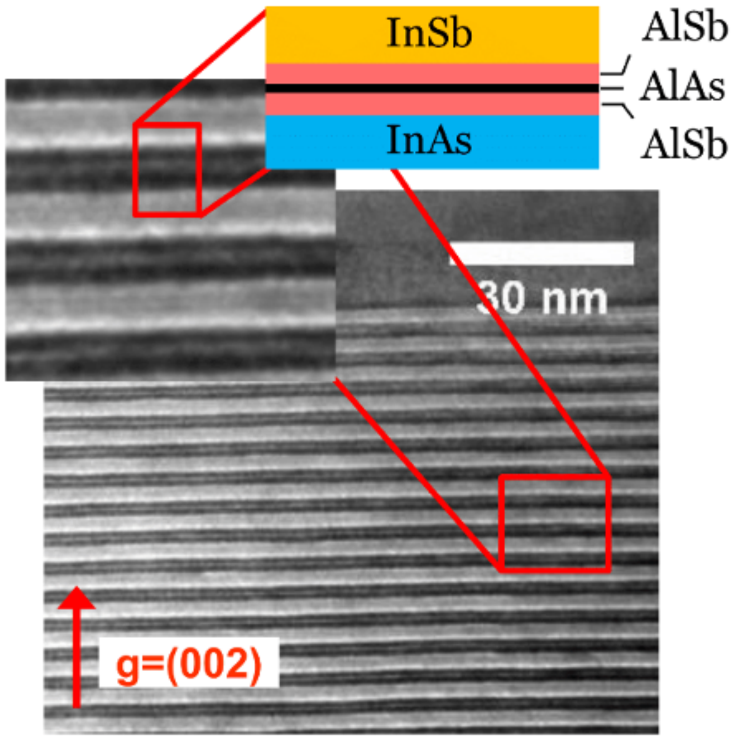

Figure 1.15: A transmission electron microscope image showing the repeating pattern of the four constituent binaries in the digitally grown AlInAsSb crystal[28].

Using this growth technique in collaboration with our research group, PIN APD structures were grown, demonstrating superior APD qualities in terms of dark current, gain, excess noise, and temperature stability[29–32]. An empirical model was developed to describe the change in bandgap with the change in Al concentration:

$$E_{\mathrm{G}}(\mathrm{x}) = 0.247 + 0.97\mathrm{x} + 0.47\mathrm{x}^2 \tag{15}$$

where $E_{\mathrm{G}}(\mathrm{x})$ is the bandgap in eV, and x is Al concentration. Using this equation, the wavelength tunability for AlInAsSb ranges from ~1 μm for 80% Al down to ~5 μm for 0% Al. This large tunability was used to make Separate Absorption, Charge, and Multiplication APD structures tailored for detecting 1.55-μm and 2-μm light[33–35]. Additionally, as the Al concentration increases, it was found that most of the energy increase goes toward increasing the conduction band, while the valence band remains relatively unchanged[36]. This asymmetry in conduction and valance band movement is integral in realizing staircase APDs, a topic to be discussed in subsequent chapters.

It should be noted that we usually refer to $Al_xIn_{1-x}As_ySb_{1-y}$ with only its composition of Al ($Al_{0.7}InAsSb$). It is assumed that the relative compositions of As and Sb have been adjusted to ensure a lattice match to GaSb. To calculate the composition of As required for a lattice match, a linear interpolation of the lattice constants of the binary constituents can be used. This is (16) below, a generalization of Vegard's Law[37,38],

$$\mathrm{xy}a_{\mathrm{AlAs}} + \mathrm{x}(1-\mathrm{y})a_{\mathrm{AlSb}} + (1-\mathrm{x})\mathrm{y}a_{\mathrm{InAs}} + (1-\mathrm{x})(1-\mathrm{y})a_{\mathrm{InSb}} = a_{\mathrm{GaSb}} \tag{16}$$

where a_{XY} is the lattice constant of the constituent binary. With a given concentration value for x, y can be calculated by solving (16) for y.

$$\mathrm{y} = \frac{-a_{\mathrm{AlSb}}\mathrm{x} + a_{\mathrm{InSb}}(\mathrm{x}-1) + a_{\mathrm{GaSb}}}{\mathrm{x}(a_{\mathrm{AlAs}} - a_{\mathrm{AlSb}}) - a_{\mathrm{InAs}}\mathrm{x} + a_{\mathrm{InAs}} + a_{\mathrm{InSb}}(\mathrm{x}-1)} \tag{17}$$

Table 1.1 includes the lattice constants for the four binary constituents of $Al_xIn_{1-x}As_ySb_{1-}$y and the lattice constant for GaSb. Substituting these values into (17) yields a simplified relation for calculating the y value required for maintaining a lattice match to GaSb.

$$\mathrm{y} = \frac{0.383 - 0.343\mathrm{x}}{0.421 + 0.055\mathrm{x}} \tag{18}$$

Table 1.1: Lattice constants of $Al_xIn_{1-x}As_ySb_{1-y}$/GaSb constituent binaries[38]

Binary	**Lattice Constant, *a* (Å)**
AlAs	5.660
AlSb	6.136
InAs	6.058
InSb	6.479
GaSb	6.096

As an example, if we take x = 0.7 ($Al_{0.7}InAsSb$), using (18) yields y = 0.31. Therefore, the overall composition of $Al_{0.7}InAsSb$ required for a lattice match to GaSb is $Al_{0.7}In_{0.3}As_{0.31}Sb_{0.69}$. This is nearly identical to what was grown for the original $Al_{0.7}InAsSb$ PIN APD[33].

2 APD Noise Considerations

In this chapter, I will discuss four considerations for measuring the excess noise of low-k-factor Sb-based materials with a specific focus on AlInAsSb/GaSb. In the past several years, our group has studied AlInAsSb grown as a digital alloy on GaSb, as discussed in the background section. There have also been examples of AlInAsSb PIN APDs grown on InP exhibiting a low k-factor[39,40]. Another Sb-based materials system with growing popularity is AlGaAsSb grown on InP[32,41–43], again showing low k-factor excess noise scaling.

For such low k-factor materials, I have compiled four crucial considerations for properly measuring the excess noise factor. The first consideration compares the calculation of $F(M)$ using a single reference point versus a calculation based on a reference line. Second, three measurement setups are provided for performing measurements at different RF operating frequencies. Third, the wavelength dependence on $F(M)$ is explored. Finally, two gain correction methods are shown to compensate for bias-dependent responsivity in APD structures.

2.1 Growth, Fabrication, and Initial Characterization

To perform this study, $Al_{0.7}InAsSb$ epitaxial layers were grown as a digital alloy on an n-type GaSb substrate via molecular-beam epitaxy, as described in a previous publication[27]. Figure 2.1 shows a schematic cross-section of the device. Devices were made using the process described in Appendix 1: Device Fabrication. I-V measurements were performed with a Keithley 2400 SourceMeter. Figure 2.2(a) shows the dark current, measured under blackout conditions, and photocurrent, under ∼46 μW of 543-nm He–Ne laser illumination for a 100 μm diameter device. C-V measurements were performed with an HP 3275A LCR meter at 1 MHz under blackout conditions. Figure 2.2(b) shows a C-V curve and a depletion width versus the voltage curve for a 200-μm diameter device. The depletion width was calculated assuming a parallel plate capacitor model with a relative permittivity of 13.9. The inset of Figure 2.2(b) shows the calculated doping concentration versus the depletion width extracted from the measured C-V, using a method described in the Capacitance-voltage Characteristics section above. The inset shows that the uid concentration in the "intrinsic" region is ~$5x10^{15}$ cm^{-3}.

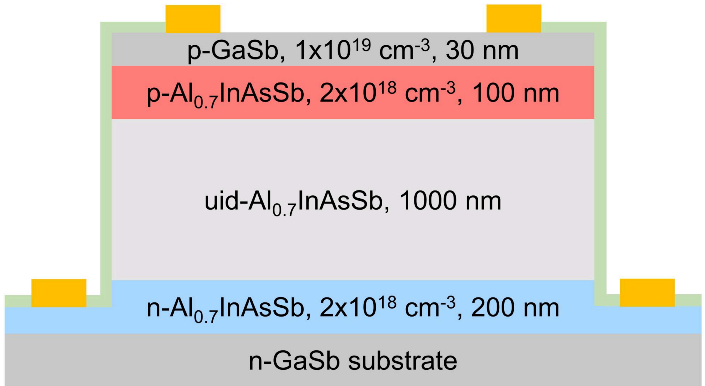

Figure 2.1: The schematic cross-section of the $Al_{0.7}InAsSb$ PIN APD structure in this paper.

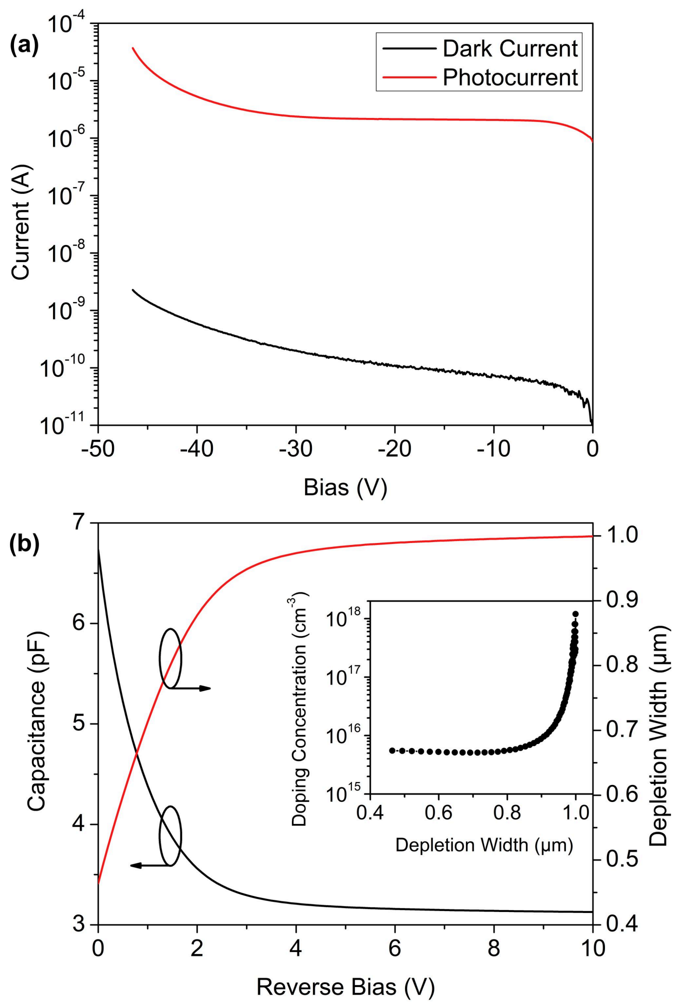

Figure 2.2: (a) Current-voltage curves under blackout conditions and ~46 µW of 543-nm illumination for a 100-µm diameter device. (b) A capacitance-voltage curve (black) and depletion width versus voltage curve (red) for a 200-µm diameter device under blackout conditions, and (inset) the doping concentration versus depletion width calculated from the C-V curve.

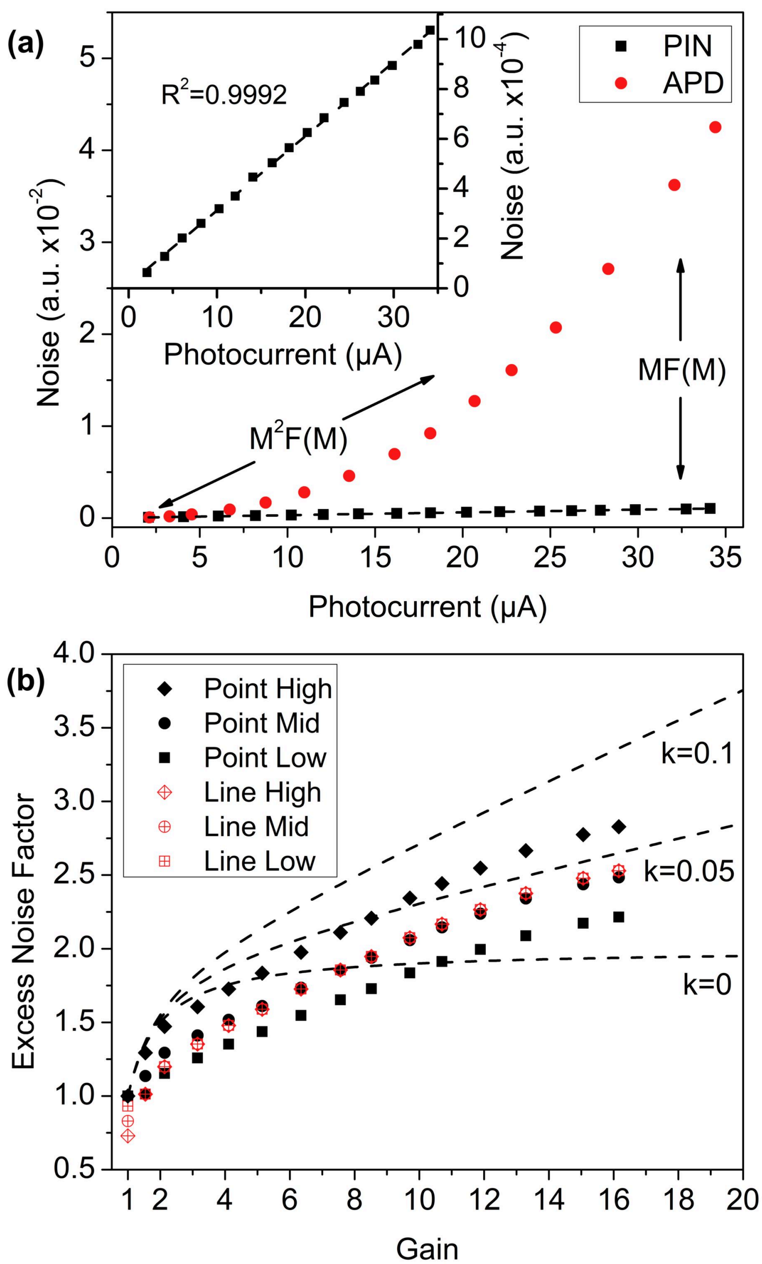

Figure 2.3: (a) Measured noise of a 100-μm diameter device under a fixed illumination intensity with increasing bias (APD curve), the measured noise under fixed bias (-10 V) and varying illumination intensity (PIN curve), and (inset) a blown-up plot of the PIN curve. (b) The excess noise factor from the point method for different first-point uncertainties is in black, and the excess noise factor from the line method for different first-point uncertainties is in red.

2.2 $F(M)$ Calculation: Single Point versus Reference Line

Unless otherwise noted, all excess noise measurements in the remainder of this chapter were performed with an Agilent 8973 noise figure analyzer at 50 MHz with a 4-MHz bandwidth under 543-nm He-Ne laser illumination on 100-μm diameter devices.

Typically, the excess noise of an APD can be measured by taking a fixed light intensity and varying the bias to achieve increased gain. At each bias point, the noise is measured without illumination and is subtracted from the noise measured under illumination—such a measurement results in a curve such as the red points in Figure 2.3(a). If the first bias point is at a sufficiently low bias such that there is no gain (M = 1) and $F(M)$ = 1, that point can be used as a reference. Neglecting dark current, this first point (N_{unity}) represents the terms $2qI_{\mathrm{unity}}\Delta f$, where I_{unity} is the photocurrent with unity gain. The gain is determined by increasing the bias and taking the ratio of the photocurrent to that of the unity gain point. $F(M)$ can then be calculated using the following expression:

$$F(M) = \frac{N_{\mathrm{measured}}}{N_{\mathrm{unity}} M^2} \tag{19}$$

where $N_{\mathrm{measured}} = 2qI_{\mathrm{unity}}\Delta f M^2 F(M)$ is the measured noise under higher bias with gain, M, and N_{unity} is the noise of the first unity gain point. This method works if there is little error in measuring the first point. However, since every subsequent measured bias point relies on the accuracy of the first point, any uncertainty in the noise of the first point affects the results of every other point along the line. With the noise figure meter setup, the noise can vary on the order of ±0.004 dB. This uncertainty is represented in Figure 2.3(b). The three black curves represent the effect on the measured excess noise at the upper end (+0.004 dB), middle, and lower end (−0.004 dB) of the uncertainty range. A significant change in the measured $F(M)$ is visible.

An approach to circumvent this issue is to use a reference line so that the measured points are independent of each other. This approach is similar to one presented by Bulman et al.[44]. The APD is biased at a low voltage (-10 V) to ensure unity gain and unity $F(M)$ and to ensure the device is fully depleted, as seen in Figure 2.3(b). Then, at this fixed bias, the intensity of incident light is increased, and the noise is measured. This measurement is shown by the black points in Figure 2.3(a) and represents only the I_{photo} contribution to the noise. The inset of Figure 2.3(a) shows a blown-up plot of this measured line. These points are then fit with a line, and those fit values are used to calculate $F(M)$ from the points in red in Figure 2.3(a) using the following equation:

$$F(M) = \frac{N_{\text{measured}}}{N_{\text{line}} M}. \tag{20}$$

In (20), $N_{\text{line}} = 2qI_{\text{photo}}\Delta f$ and $N_{\text{measured}} = 2qI_{\text{photo}}\Delta f M F(M)$. It should be noted that this representation of N_{measured} only contains one factor of M. The other factor of M was used to convert $I_{\text{photo,unity}}$ to I_{photo} where $I_{\text{photo}} = I_{\text{unity}}M$. The shot noise of an APD is typically calculated with reference to unmultiplied photocurrent, I_{unity}; however, the shot noise can also be calculated with reference to the measured output photocurrent, which includes the increase in photocurrent due to gain. Overall, for an APD the shot noise can be represented as either $2qI_{\text{unity}}\Delta f M^2 F(M)$ or $2qI_{\text{photo}}\Delta f M F(M)$, both forms are equivalent. The calculated $F(M)$ using the reference line method, with the same uncertainty in the first point as with the "point" method, is plotted as the red points in Figure 2.3(b). For the red curves, as the noise of the first point changes, none of the subsequent points are affected. Therefore, this line reference method offers a more robust $F(M)$ calculation than calculating $F(M)$ based solely on the first point.

2.3 Operating Frequency Dependence of $F(M)$

For "high frequency" noise measurements above 15 MHz (the lower frequency limit of an Agilent 8973 NFA), an NFA can be used in a configuration shown in Figure 2.4(a) in which a bias tee is used to simultaneously provide an isolated DC bias to a DUT and couple the AC response to the NFA. Additionally, above 10 MHz, a group from the University of Sheffield has demonstrated a noise measurement setup using a trans-impedance amplifier (TIA) that can provide accurate measurement results for high dark current and high capacitance APDs[45]. However, neither design is suitable for measuring devices under 10 MHz. A setup that can measure below 10 MHz is useful if, for instance, the DUT has a bandwidth of less than 10 MHz. Examples of such devices are presented in Chapters 5 and 6.

Figure 2.4(b) shows the schematic for such a setup that can measure the $F(M)$ of a device at as low as ~20 kHz. In this setup, the DUT is probed with a ground-signal probe with the positive link connected to the input of a Femto DLPCA-200 TIA and the negative link connected to the positive port on a Keithley 2400 SourceMeter. The negative port of the SourceMeter is attached to the metal case of the TIA. The output of the TIA is routed to the input of an Agilent E4440A spectrum analyzer (SA). Since the TIA has a built-in AC couple, a DC bias can be applied across the DUT, and the DC signal is isolated from the SA. This configuration acts as a crude bias-tee. The TIA is set to the low-noise performance range with a trans-impedance of 10^5 V/A. This gain was chosen to ensure the TIA was not overloaded. The upper limit of measurement frequencies for this setup is ~400 kHz and is limited by the bandwidth of the TIA. This setup will be essential for many of the excess noise measurements made in subsequent chapters. It was used to measure the excess noise of staircase APDs, SACM staircase APDs, and cascaded multiplier APDs presented in the following chapters.

To confirm the viability of this setup, a 100-µm diameter AlInAsSb APD was measured with the “high frequency” NFA-based setup in Figure 2.4(a) and the “low frequency” SA-based setup in Figure 2.4(b). The SA was centered at 68.7 kHz with a resolution bandwidth of 47 Hz. This measurement frequency was selected because the system noise floor was low enough to detect the noise of the DUT and avoid ambient noise sources. The results of these measurements are shown in Figure 2.4(c). Aside from the first point, which is prone to increased uncertainty due to its close proximity noise floor, as previously discussed, there is an 8% difference between the two measurements at most.

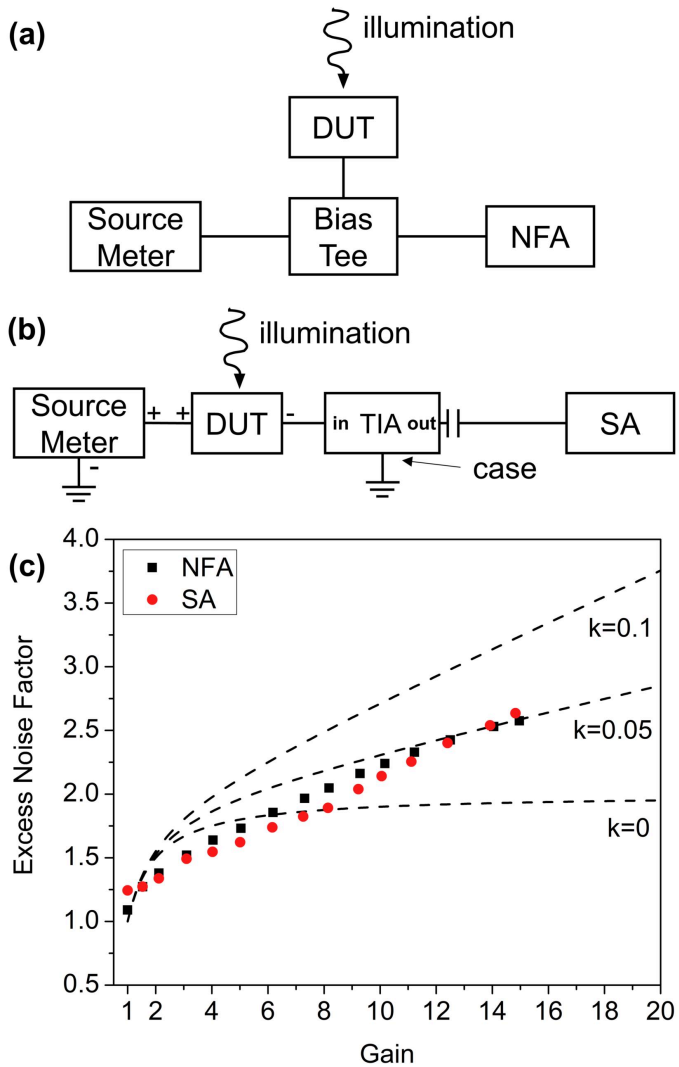

Figure 2.4: (a) The noise-figure-analyzer-based setup for measurements above 10 MHz. (b) The spectrum-analyzer-based setup for measurements between ~20 kHz and ~400 kHz. (c) The excess noise factor versus gain for the same 100-µm diameter device using the two different setups in (a) and (b).

2.4 Wavelength Dependence of $F(M)$

Another factor to consider when measuring $F(M)$ is the wavelength of light used, as different wavelengths can lead to drastically different $F(M)$ measurements. The difference originates from wavelength-dependent absorption, which can lead to different carrier injection profiles. Typically, from the infrared to the visible, the absorption coefficient in a semiconductor material increases as the wavelength decreases. For short wavelengths, such as 445 nm, the light is absorbed very near the incident surface. This quick absorption enables pure electron injection into the multiplication region in a top-illuminated PIN structure. In many semiconductors, pure electron injection is favorable because the impact ionization coefficient for electrons is greater than that for holes. This, in turn, results in a lower k-factor, resulting in lower $F(M)$ at a given gain. For longer wavelengths such as 633 nm, much of the light is absorbed throughout the multiplication region, resulting in mixed injection with higher k-factors and higher $F(M)$ at a given gain, as both electrons and holes are injected into the multiplication region.

Specifically, for the devices used in this chapter, 445-nm (laser diode), 543-nm (He-Ne laser), and 633-nm (He-Ne laser) light was used to measure $F(M)$ under different injection regimes. The approximate thickness, x, to absorb a fraction η of the incident light (ignoring surface and interface reflections) can be calculated using the following expression:

$$x = -\frac{(\ln(1-\eta) + \alpha_{\mathrm{GaSb}} x_{\mathrm{GaSb}})}{\alpha_{70\%}} + x_{\mathrm{GaSb}} \tag{21}$$

where $\alpha_{70\%}$ is the absorption coefficient of $Al_{0.7}InAsSb$ at a given wavelength, α_{GaSb} is the absorption coefficient of GaSb at a given wavelength, and x_{GaSb} is the thickness of the GaSb cap layer (30 nm). Using previously published absorption coefficients for $Al_{0.7}InAsSb$[46] and GaSb[47], the approximate thickness to absorb 99% of the incident light is 106 nm, 397 nm, and 706 nm for 445-nm, 543-nm, and 633-nm light, respectively. Comparing these lengths to the structure from Figure 2.1 shows that 445-nm light should give essentially pure electron injection, whereas 633-nm light results in a more uniform mixed injection. $F(M)$ was measured for these three wavelengths and is plotted in Figure 2.5. It should be noted that the light power for the three wavelengths was chosen to ensure that the same photocurrent, ~2 µA, was measured at -20 V. The light powers needed were ~202 µW, ~46 µW, and ~21 µW for 445 nm, 543 nm, and 633 nm light, respectively. For these three wavelengths, the k-factor ranges from ~0.01 for 445 nm light to ~0.09 for 633 nm light. For the 445-nm curve, $F(M)$ scales below the k=0 curve to a gain of ~10, a phenomenon commonly seen in Sb-based APDs[43,48,49].

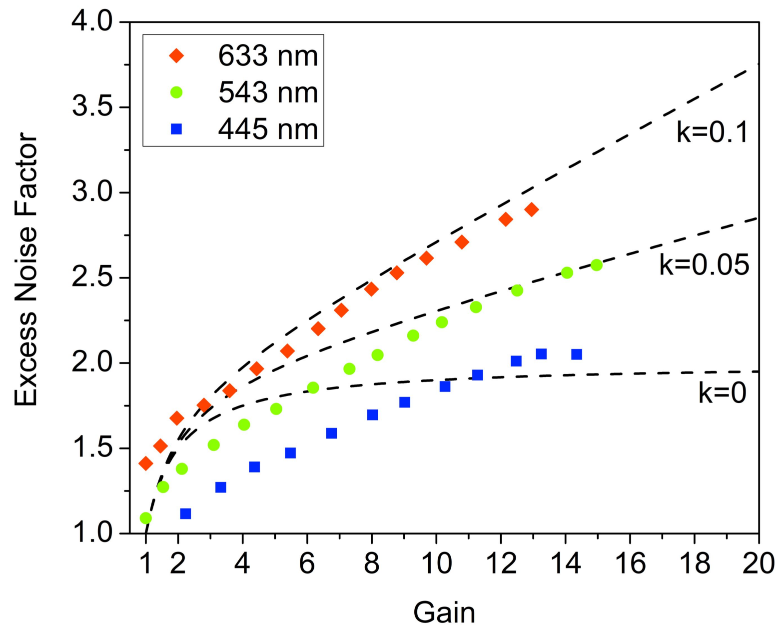

Figure 2.5: The excess noise factor versus gain for ~21 µW of 633-nm light, ~46 µW of 543-nm light, and ~202 µW of 445-nm light.

2.5 Gain Corrections

The final consideration with excess noise factor measurements is the correct determination of device gain. The easiest way to calculate the gain in an APD is to designate a point in the "flat" region of the I-V as the unity gain point. With this definition, all current values above that unity point are considered gain. In Figure 2.2(a), there appears to be a broad flat region in the photocurrent of the I-V after the device has fully depleted from -5 V to -25 V. However, when the I-V is plotted on a linear scale and “zoomed in” around the flat region, as plotted in Figure 2.6(a), there is a slight slope in the photocurrent plot. This small increase in current is attributed to the slight increase in carriers diffusing from the p-contact region into the high-field uid region as the depletion width increases into the contact layers under higher bias.

It should be noted that the slope of this flat region will increase as the background concentration of the intrinsic region increases and as the doping concentration of the contact layer decreases. Without taking this slight bias-dependent responsivity into account, the gain can simply be calculated by calling the current at -20 V “unity” and calculating the gain with this reference point. The black curve titled “point method” is shown in the inset of Figure 2.6(a). Using this approach, the highest gain at -46.5 V is ~17.3.

A straightforward method to account for this bias-dependent responsivity is to fit a line to the flat region and define the current along that line as "unity." With this method, any current above the line is considered gain. This method was used to fit a line between -10 V and -20 V. The result is the "Linear Fit" line in Figure 2.6(a), and the resulting gain is plotted in the inset. It should be noted that the max gain has been reduced to ~15.9. A more precise way to account for this bias-dependent responsivity is to use a fit presented by Woods et al.[50]. The equation is as follows:

$$I = A + B\left(V + V_D - \frac{k_B T}{q}\right)^{1/4} \tag{22}$$

where I is the photocurrent, A and B are fitting constants, V is voltage, k_B is Boltzmann's constant, T is temperature, and q is the elementary charge. V_D is the diffusion voltage expressed as

$$V_D = \left(\frac{k_B T}{q}\right)\ln\left(\frac{N_A N_D}{n_i^2}\right) \tag{23}$$

where N_A and N_D are the p- and n-contact doping concentrations, respectively, and n_i is the background concentration of the intrinsic region. For this device, N_A and N_D are $2\text{x}10^{18}$ cm^{-3}, and, from the inset of Figure 2.2(b), n_i is ~$5\text{x}10^{15}$ cm^{-3}. This method was used to fit a curve between -10 V and -20 V. The result is the "Woods Fit" line in Figure 2.6(a), and the resulting gain, extracted from the current above the fit line, is plotted in the inset. With this fitting approach, the maximum gain was ~16.5.

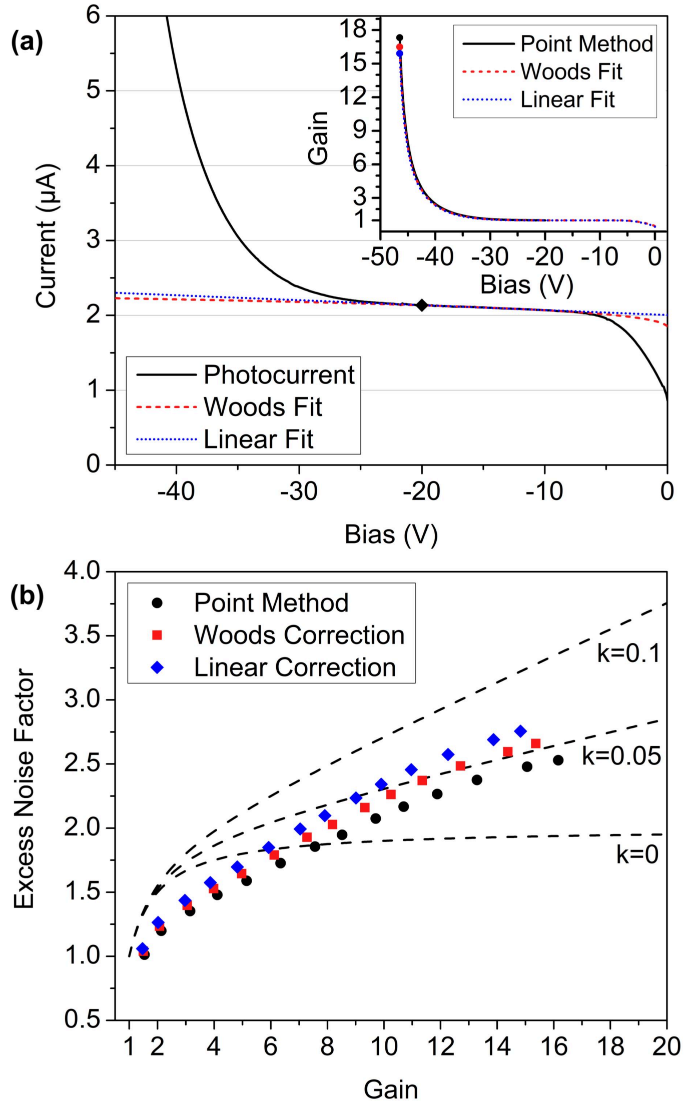

Figure 2.6: (a) The photocurrent from Figure 2.2(a) plotted on a linear scale with both the Woods fits and Linear fit, and (inset) the resulting gain from a simple point fit, Woods fit, and Linear fit. (b) The excess noise factor versus gain for the three gain calculation methods.

Figure 2.6(b) shows the resulting $F(M)$ when using the point method, the Woods correction, and the linear correction. The point method gives the highest gain and the lowest $F(M)$ since the bias-dependent responsivity is treated as gain here. The linear correction gives the lowest gain and highest $F(M)$ as it is a simple fit that attributes some of the gain above -20 V to bias-dependent responsivity. The Woods correction gives both intermediate gain and $F(M)$ and is the preferred choice for calculating gain as the fit accounts for the physical parameters of the structure and better captures the bias-dependent responsivity compared to the linear correction.

In this chapter, I have introduced and discussed four important considerations that need to be made when measuring $F(M)$ for low-k-factor materials. Calculating $F(M)$ from a reference line offers a more robust measurement less susceptible to equipment-based uncertainties. Two setups for RF operating frequencies above 10 MHz were presented, and a new setup for frequencies as low as ~20 kHz was introduced. This low-frequency setup I developed will be integral for noise measurements for several devices presented in future chapters. The wavelength dependence on $F(M)$ was explored, where shorter wavelengths yielded the lowest measured $F(M)$. Finally, two gain correction methods were introduced to help account for bias-dependent responsivity, each impacting the measured $F(M)$.

3 $Al_{0.15}In_{0.85}As_{0.77}Sb_{0.23}$-based PIN Photodiodes

In this chapter, I will present results for $Al_{0.15}$InAsSb-based PIN photodiodes that will be useful for the designs of future devices in the MWIR. Previously, the longest wavelength detector reported by our group used $Al_{0.3}$InAsSb as the absorption material and was designed to detect 2-μm light[34]. To design an APD capable of working in the MWIR, it was first essential to examine some of the material properties of Al_xInAsSb with lower Al compositions; as the bandgap is reduced, the cutoff wavelength is increased[27]. The composition of choice was $Al_{0.15}$InAsSb, as by using (15), the predicted cutoff wavelength is around 3-μm.

3.1 Material Characterization

To characterize $Al_{0.15}$InAsSb, simple PIN detectors were grown to determine materials and device properties that could be useful for future MWIR device designs. Figure 3.1(a) shows the schematic cross-section of the device grown on a GaSb substrate by our collaborators at the University of Texas at Austin. Figure 3.1(b) shows an X-ray diffraction pattern of the grown epitaxial layers with the substrate and superlattice fringe peaks labeled. The 0^{th}-order superlattice peak and the peak of the GaSb substrate nearly overlap, indicating a minimal lattice mismatch. Figure 3.2 shows the photoluminescence of the crystal measured at several temperatures. At 78 K, the peak is at 2.89 μm with a full width at half maximum of 45 meV (6.7 kT). At 300 K, the peak is at 2.94 μm with a full width at half maximum of 81 meV (3.1 kT). The peak at 300 K falls between previously reported PL intensity peaks for $Al_{0.09}$InAsSb (3.35 μm) and $Al_{0.19}$InAsSb (2.64 μm)[27]. The peak in the PL spectrum around 3.25 μm is likely due to atmospheric absorption.

Ellipsometry was performed with a J.A. Woollam VASE Ellipsometer on the bare epitaxy prior to device fabrication. The wavelength range extended from 280 to 2900 nm with measurement angles from 65° to 75° in 5° increments. Figure 3.3(a) shows the measured Ψ and Δ at three angles and their corresponding fits obtained using a B-spline fitting approach. Refractive indices, extinction coefficients, and absorption coefficients were extracted from the fits and are displayed in Figure 3.3(b).

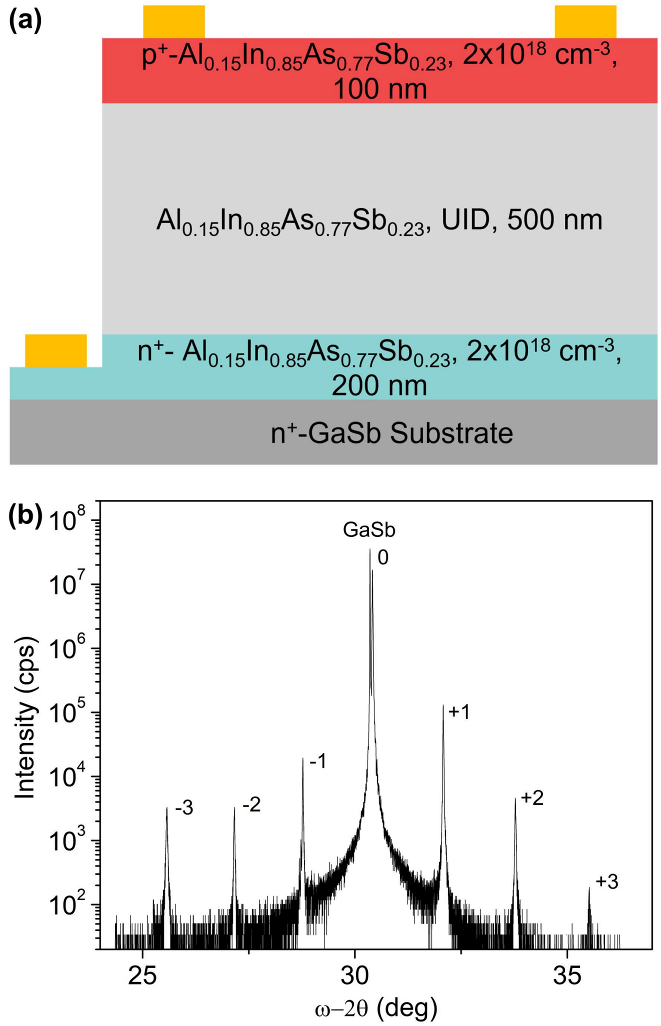

Figure 3.1: (a) The schematic cross-section for the $Al_{0.15}InAsSb$ PIN and (b) the X-ray diffraction pattern for $Al_{0.15}InAsSb/GaSb$.

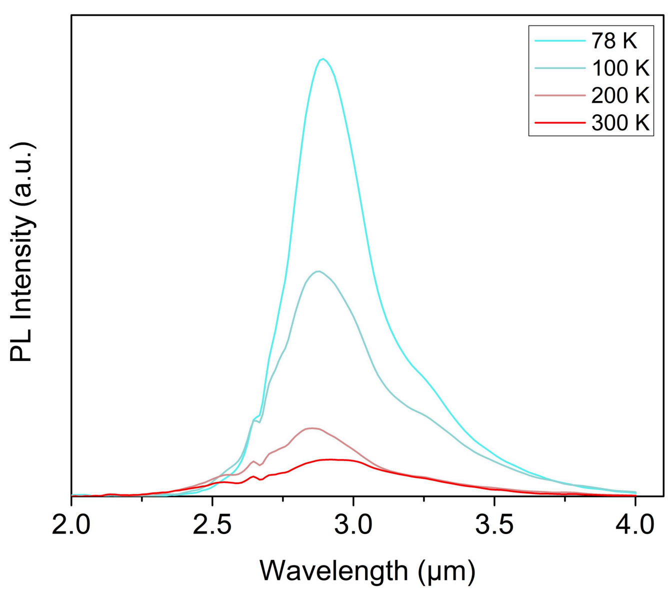

Figure 3.2: The photoluminescence versus wavelength for $Al_{0.15}InAsSb/GaSb$ at different temperatures.

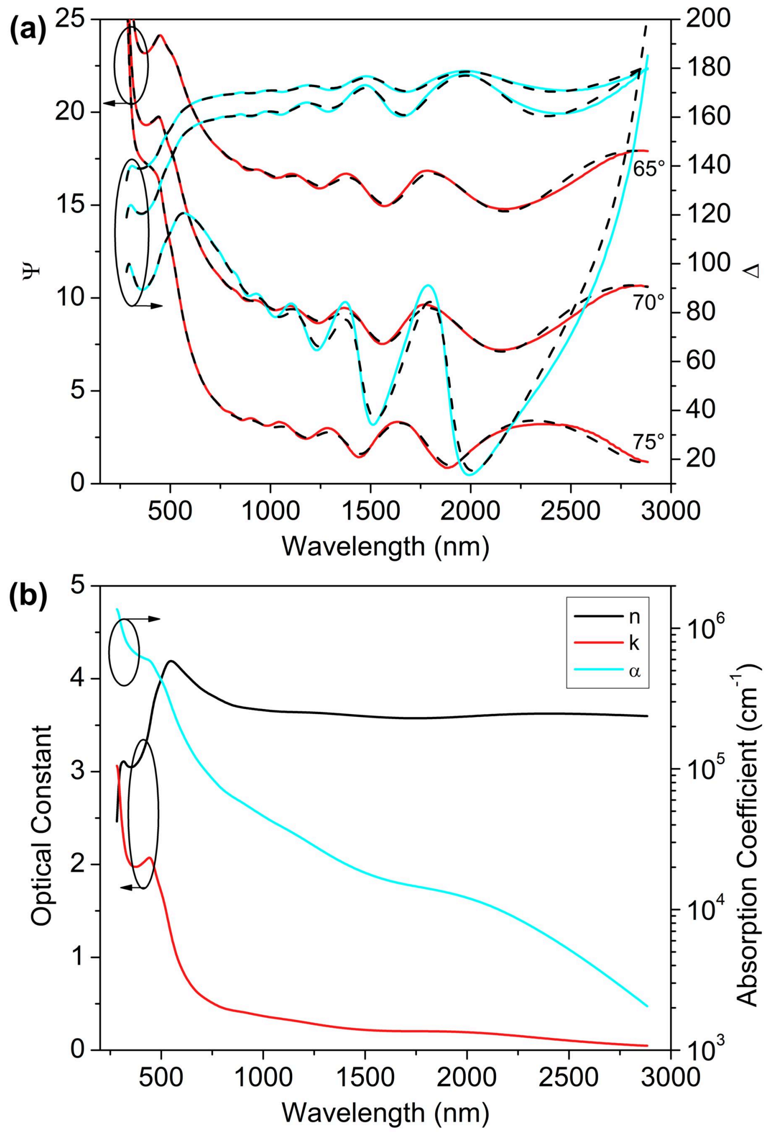

Figure 3.3: (a) Measured Ψ and Δ with their corresponding fits (dashed), and (b) the extracted refractive indices, extinction coefficients, and absorption coefficients for $Al_{0.15}InAsSb/GaSb$.

3.2 Device Characterization

Devices were fabricated using the process outlined in Appendix 1: Device Fabrication. I-V curves were measured with an HP 4145 Semiconductor Parameter Analyzer in a cryogenic chamber cooled with liquid nitrogen. Figure 3.4(a) shows the dark current and photocurrent obtained using a temperature-stabilized 2-μm fiber-coupled laser diode at 200 K. For the photocurrent curve, ~27 μW of light was incident on the top of the mesa. The light was focused with a fiber lens to a spot size smaller than the mesa diameter to ensure no sidewall illumination. A characteristic kink in the dark current curve is visible at -4.5

V, indicating the onset of tunneling. Assuming a uniform electric field in the depletion region, the onset of tunneling occurs at an electric field strength of ~0.9 kV/cm at 200 K. The photocurrent is constant out to the intersection of the photocurrent and dark current curves. Figure 3.4(b) shows the C-V curve for a 200-µm-diameter device measured with an HP 3275A LCR meter at room temperature under dark conditions. The capacitance has leveled off at a reverse bias of 2 V, indicating the device is fully depleted. Dark current was measured in 20-K increments from 100 K to 300 K and is plotted as dark current density in Figure 3.5.

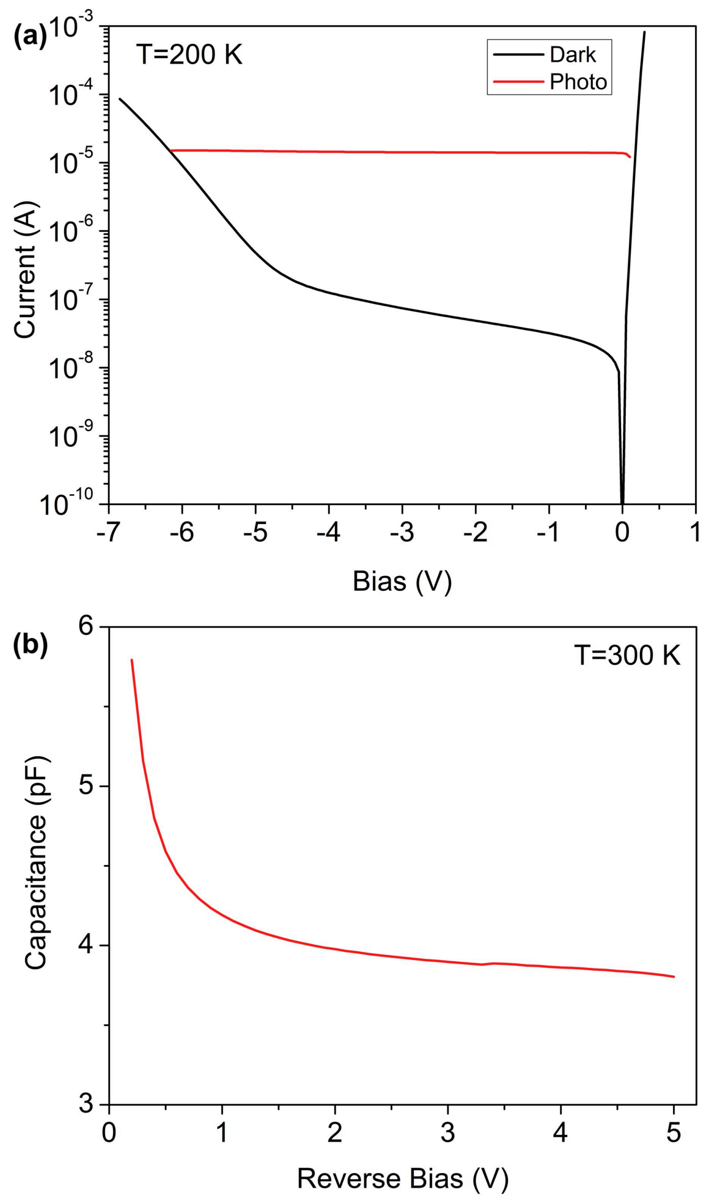

Figure 3.4: (a) I-V characteristic at 200 K for a 150-µm diameter $Al_{0.15}InAsSb$ PIN with photocurrent, under ~27 µW of 2-µm illumination, and dark current. (b) A C-V curve at 300 K for a 200-µm diameter device.

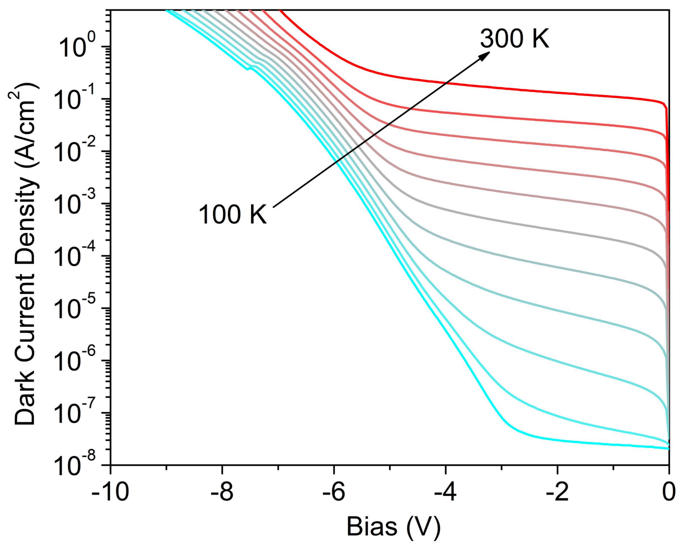

Figure 3.5: Dark current density versus temperature curves from 100 K to 300 K in 20-K increments for the $Al_{0.15}InAsSb$ PIN.

Responsivity was measured at 300 K at 1.55 μm and 2 μm with temperature-stabilized fiber-coupled laser diode illumination. A reverse bias of 2 V was used to ensure full depletion of the device. At 1.55 μm and 2 μm, the responsivity was 0.49 A/W and 0.53 A/W, respectively, corresponding to 39% and 33% external quantum efficiencies, respectively. The theoretical external quantum efficiency was calculated using (8). Using the refractive index and absorption coefficient in Figure 3.3(b) at 1.55 μm and 2 μm, the theoretical external quantum efficiencies are 39% and 31%, respectively. The difference between the theoretical and measured quantum efficiencies is likely due to uncertainty with fitting the optical constants. A B-spline approach for fitting was used because there is no reference model for $Al_xIn_{1-x}As_ySb_{1-y}$. Also of note, the depletion region is only 500 nm thick, with no anti-reflection (AR) coating. From the optical constants in Figure 3.3(b), a normal incidence surface reflection can be calculated at 1.55 μm and 2 μm of ~31%. Therefore, with a proper 1%-reflectivity AR coating, quantum efficiencies can be expected up to ~57% and ~48% at 1.55-μm and 2-μm illumination, respectively.

The activation energy was extracted from the measurements in Figure 3.5 using the relation,

$$I_{\mathrm{dark}} \propto T^2 \exp\left(\frac{-E_a}{k_B T}\right) \tag{24}$$

where I_{dark} is the measured dark current, T is the temperature in kelvin, E_a is the activation energy, and k_B is the Boltzmann constant. Figure 3.6 shows dark current density plotted against inverse temperature for reverse bias voltages from 1 V to 5 V in 1-V increments for a 150-µm-diameter device. Equation (24) was used to fit curves to the measured values and extract an activation energy for each bias voltage. The extracted activation energies are plotted in the inset. The bandgap for $Al_{0.15}InAsSb$ is known to be ~0.4 eV[27]. These activation energies are approximately half the bandgap energy, which indicates that thermal generation dominates. At low temperatures under 4 V and 5 V reverse bias, trap-assisted tunneling current likely dominates the activation energy[51].

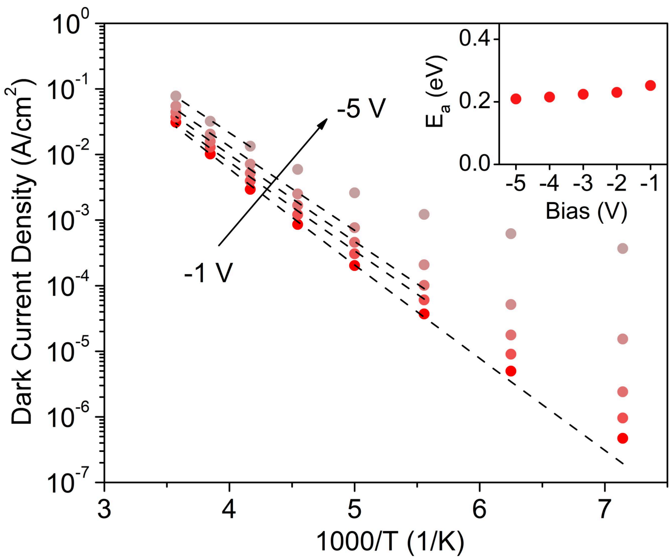

Figure 3.6: Dark current density versus inverse temperature for the $Al_{0.15}InAsSb$ PIN from -1 to -5 V in -1-V increments with (24) fits (dashed). The inset shows the extracted activation energy versus bias.

The forward I-V characteristic was measured from 200 K to 380 K in 20-K increments using a Keithley 2400 SourceMeter. The measured curves were fitted with (25) at each temperature to extract the ideality factor. J is the measured forward current density, J_S is the reverse saturation current density, q is the elementary charge, V is the applied voltage, n is the ideality factor, k_B is the Boltzmann constant, and T is the temperature in kelvin.

$$J = J_S\left(\exp\left(\frac{qV}{nk_BT}\right) - 1\right) \tag{25}$$

Both J_S and n were fit to the measured data using (25). Figure 3.7(a) shows the measured forward current density for a 200-μm-diameter device with fits shown as dashed lines. There is excellent agreement between the measured data and the fit curves. Figure 3.7(b) shows the extracted ideality factor plotted against temperature for two different mesa diameters, 150 μm and 200 μm. Two different-sized devices were measured to assess the role of surface effects. From 200 K to 300 K, the ideality factors for the two sizes are the same and decrease with increasing temperature. This inverse trend between ideality factor and temperature has been previously reported in other structures[52,53]. However, above 300 K, the ideality factor increases with temperature, and the two mesa diameters diverge. The sharp increase in ideality factor above 300 K likely results from the activation of surface effects, as indicated by the more significant increase of the 200-μm-diameter device compared to the 150-μm-diameter device.

The fitted J_S from (25) is plotted versus inverse temperature in Figure 3.8. Using the fitted J_S, the activation energy was extracted using a similar method as in Figure 3.6. Under a similar temperature range as above, the activation energy is 0.25 eV, similar to the values above. At higher temperatures above 300 K, the extracted activation energy is 0.48 eV. This activation energy is similar to the bandgap of $Al_{0.15}InAsSb$, indicating diffusion current dominates.

In this chapter, I have presented several characteristics of $Al_{0.15}InAsSb$-based PIN photodiodes that will be useful for future designs of APDs operating in the MWIR; specifically, the one discussed in the subsequent chapter, $Al_{0.05}In_{0.95}As_{0.93}Sb_{0.07}$-based SACM APDs. The extracted absorption coefficients are useful for estimating the EQE in a proposed design using (8). The dark current density versus temperature plot helps estimate the bulk dark current at a given temperature. Finally, the tunneling field extracted from the I-V in Figure 3.4(a) will be useful for optimizing the charge region thickness in an SACM design to allow for a high electric field to build up in the multiplier before tunneling occurs in the absorber.

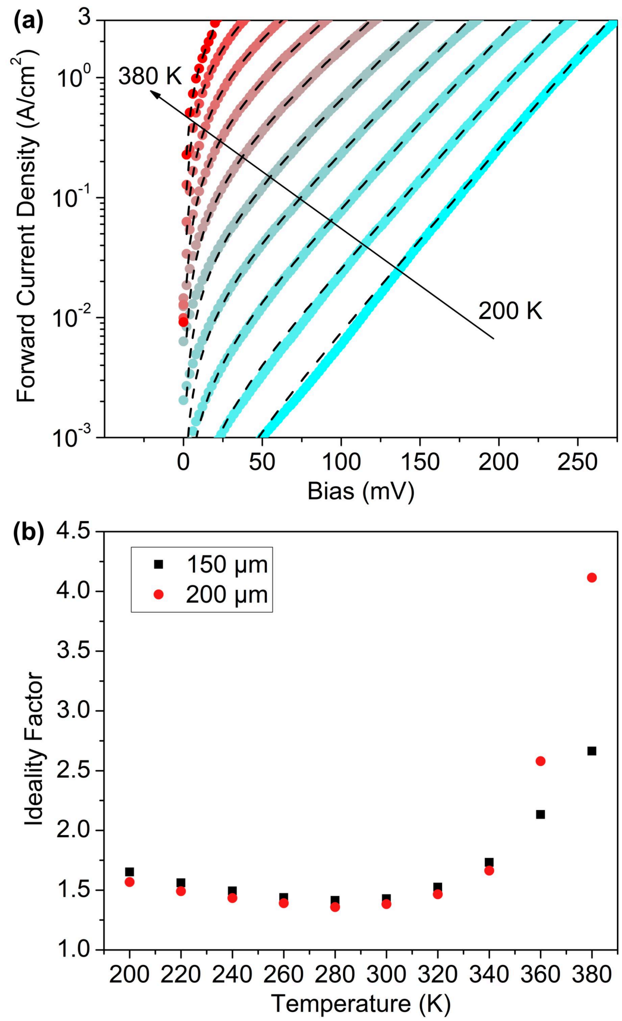

Figure 3.7: (a) Forward current density versus bias for the $Al_{0.15}InAsSb$ PIN from 200 K to 380 K in 20-K increments with (25) fits (dashed). (b) The extracted ideality factor versus temperature for a 150-µm diameter and a 200-µm diameter device.

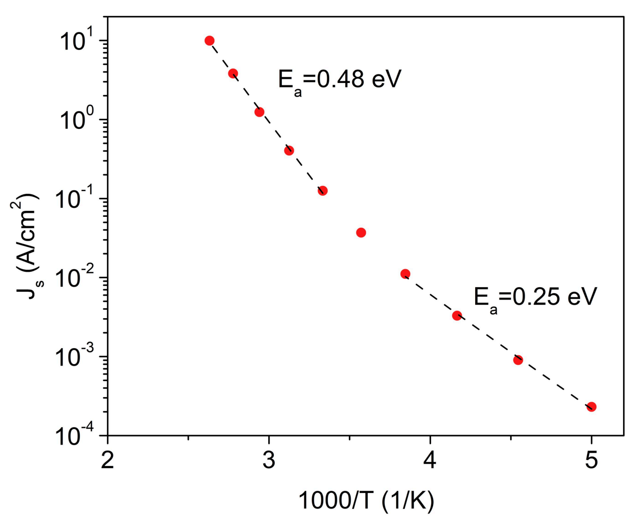

Figure 3.8: Reverse saturation current density, J_S, versus inverse temperature for the $Al_{0.15}InAsSb$ PIN with the corresponding activation energy fitted using (24).

4 $Al_{0.05}In_{0.95}As_{0.93}Sb_{0.07}$-based SACM APDs

In this chapter, I will demonstrate an SACM APD with a $Al_{0.05}$InAsSb absorber, using some of the results gained in the $Al_{0.15}In_{0.85}As_{0.77}Sb_{0.23}$-based PIN Photodiodes chapter above. As mentioned in the Background section, an SACM structure is popular for MWIR detection as it alleviates band-to-band tunneling issues that plague narrow bandgap materials required to absorb MWIR light while simultaneously providing amplification in a wide bandgap region. The device presented in this chapter is the first AlInAsSb-based SACM APD capable of efficiently absorbing light at 3 µm. A previous design's operating window cuts off at ~3-µm[54]. The device I designed has a unity-gain EQE of 24% at 3 µm and cuts off at ~3.5 µm. Other SACM APDs previously designed in our group had cutoff wavelengths of 1.7-µm[33], 2.1-µm[34], and 2.9-µm[54].

4.1 Design

Epitaxial layers for this device, displayed in Figure 4.1(a), were grown by our collaborators at the University of Texas at Austin as a digital alloy via molecular beam epitaxy on an n-type GaSb substrate. Figure 4.1(b) shows the zero bias energy band diagram for the device with different regions of the device numbered. Region 1 is the n-contact. Region 2 is the wide bandgap $Al_{0.7}$InAsSb multiplication layer. Region 3 contains an $Al_{0.7}$InAsSb p-type charge layer and an $Al_{0.7\text{-}0.15}$InAsSb bandgap grading region. These layers establish the electric field profile and provide a smooth transition between the multiplier and absorber. Region 4 is an $Al_{0.15}$InAsSb layer that helps prevent high electric field buildup in the narrow bandgap regions of the grading layer (region 3), reducing dark current contributions from band-to-band tunneling. Region 5 is the $Al_{0.05}$InAsSb narrow bandgap absorber that has been lightly p-type doped, which helps prevent energy band sagging. Finally, region 6 acts as the p-contact and a diffusion barrier for electrons generated in the absorber. The electric field profile for the device was simulated using Lumerical CHARGE based on the finite element drift-diffusion method. Figure 4.2 displays the electric field profile under -46 V and -52 V of bias, along with lines indicating the breakdown field for both the multiplier and the absorber.

Figure 4.3 shows an X-ray diffraction pattern for the grown epitaxy shown in Figure 4.1(a) with the GaSb substrate and AlInAsSb superlattice fringe peaks labeled.

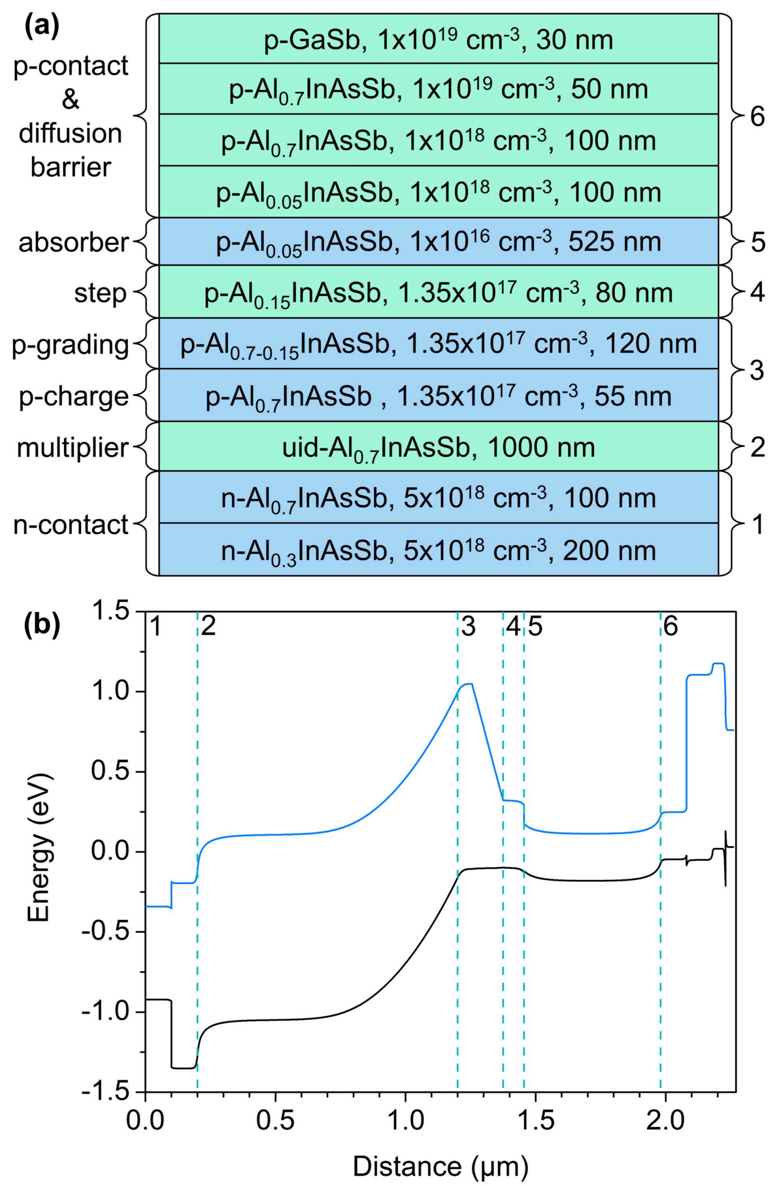

Figure 4.1: (a) The epitaxial layer structure of the 3.5-µm cutoff SACM APD, and (b) the simulated zero bias energy band diagram with corresponding regions numbered.

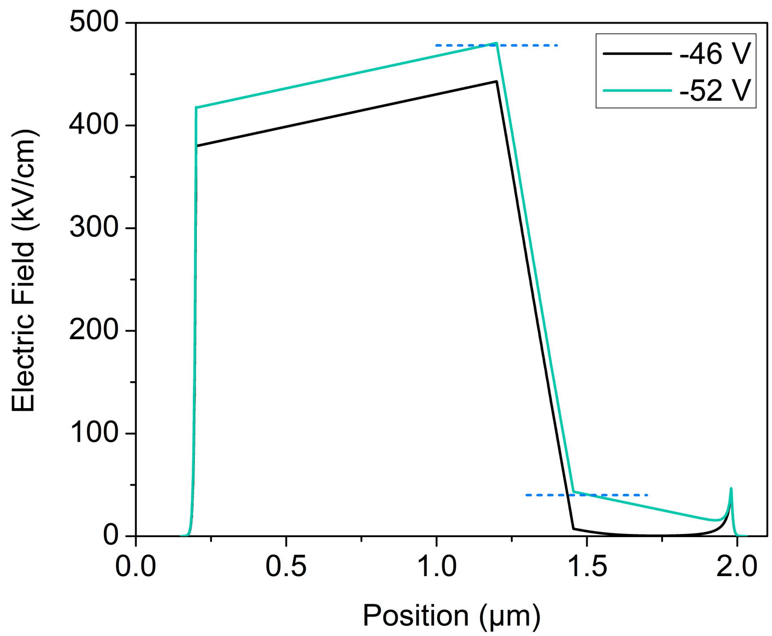

Figure 4.2: The simulated electric field profile for the device at -46 V and -52 V with the breakdown field of the multiplier and absorber indicated with horizontal lines.

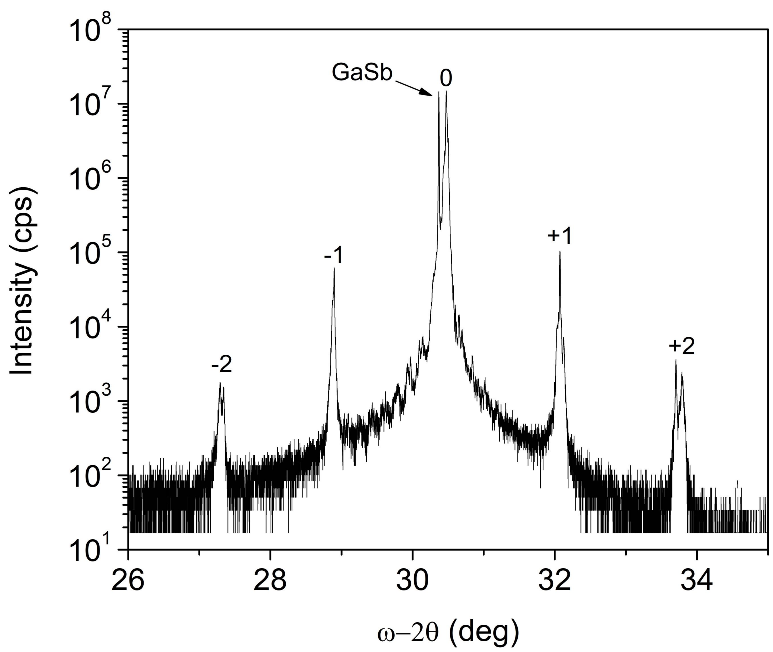

Figure 4.3: X-ray diffraction pattern for the grown epitaxial layer structure shown in Figure 4.1(a).

4.2 Characterization

Devices were fabricated using the process detailed in Appendix 1: Device Fabrication. The dry/wet etch process was used as this device contains a large region of low Al concentration AlInAsSb. A C-V curve is shown for a 150-μm diameter device in Figure 4.4(a). Measurements were performed with an HP 3275A LCR meter at 1 MHz under dark conditions in a cryogenic chamber cooled with liquid nitrogen to

100 K. In Figure 4.4(a), punch-through for the device is visible around 42 V of reverse bias as indicated by the drop in capacitance. At around 46 V, the capacitance has leveled off, indicating that the device is fully depleted. Also included in Figure 4.4(a) is a simulated C-V curve, done using Ansys Lumerical CHARGE, that can be used to verify the doping concentration in the different regions of the device. With the simulated C-V curve, the doping concentration in the multiplier (region 2) and in the absorber (region 5) regions is ~2×10^{15} cm^{-3} and is ~1.28×10^{17} cm^{-3} in the charge/grading region (regions 3 and 4). Figure 4.4(b) shows the calculated doping concentration profile versus depletion width for the C-V measured in Figure 4.4(a). The depletion width was calculated assuming a parallel plate capacitor, where the overall relative permittivity used, 13.4, is a weighted average, based on the thickness, of the relative permittivity of $Al_{0.7}InAsSb$ and $Al_{0.05}InAsSb$. The doping concentration calculation is detailed in the Capacitance-voltage Characteristics section above. The charge region doping is visible between ∼0.9 and ∼1.1 μm and has an average value of ~1.40×10^{17} cm^{-3}. The background concentration of the absorber is visible between ∼1.1 and ∼1.7 μm and has a minimum value of ~2×10^{15} cm^{-3}. The doping values extracted from the simulation and calculated from the measured C-V are within 5% of the as-designed value. This difference is very reasonable, considering the variation with growth parameters and measurement uncertainties.

I-V curves were measured using an HP 4145 Semiconductor Parameter Analyzer in a cryogenic chamber cooled with liquid nitrogen. Figure 4.5 shows the dark current and photocurrent, under ∼11 nW and ∼11 μW of 2-μm illumination, for a 150-μm diameter device measured at 100 K. A temperature-stabilized fiber-coupled laser diode was used with a fiber lens to focus the 2-μm light to a spot size smaller than the mesa diameter to ensure no sidewall illumination. Under the lowest illumination, there are two distinct steps in the photocurrent curve. The first step, around −34 V, is likely caused when the device has depleted into the $Al_{0.15}InAsSb$ barrier, region 4 in Figure 4.1(b). Since the cutoff wavelength of $Al_{0.15}InAsSb$ at 100 K is 2.94 μm[55], the 2-μm light was likely absorbed in this region, accounting for the increase in current. The second step, around −42 V, occurs because the electric field has "punched through" into the absorber, allowing for the injection of carriers from the absorber into the multiplier.

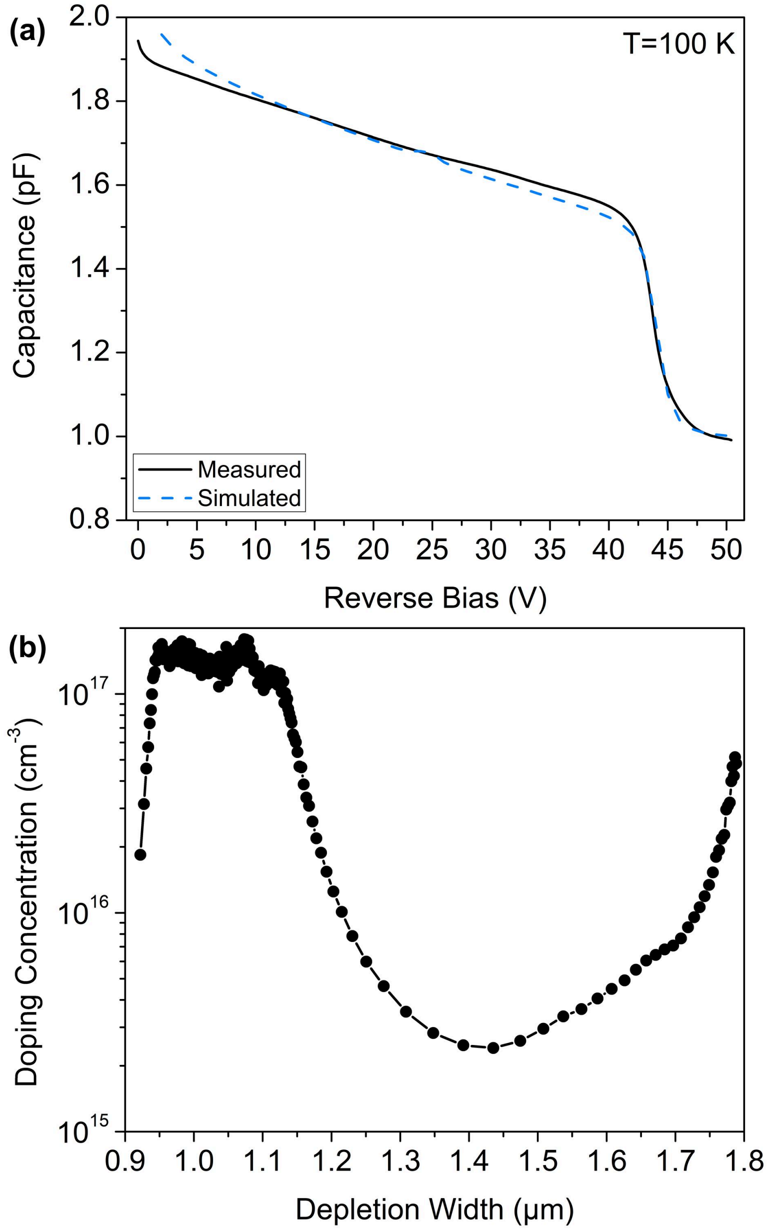

Figure 4.4: (a) The measured capacitance-voltage characteristic, performed at 1 MHz, for a 150-μm diameter device measured at 100 K and the Ansys Lumerical CHARGE simulated C-V curve. (b) The calculated doping concentration versus depletion width for the measured

The gain for this device is valid after the electric field has punched through into the absorber. As mentioned in the Background section above, an excess noise factor measurement was used to determine the gain of the device at a point after punch-through. The gain for the two illumination intensities is plotted in the inset of Figure 4.5. The difference in gain is caused by APD gain saturation, a well-known phenomenon in which the higher photocurrents in an APD cause a voltage drop across the series resistance of the device, lowering the bias across the APD and, in return, limiting the gain. At a light intensity of ~11 nW, this device achieves a gain of ~850 while still maintaining a photocurrent above the dark current. This maximum gain is more than double that of previously reported state-of-the-art InAs detectors[24,56] designed for MWIR detection. The improvement in gain for this structure is likely due to higher achievable electric fields in the multiplication region. This structure achieves gain in a wider bandgap region (~1.1 eV at 300 K), so high electric fields are achievable without band-to-band tunneling. For InAs structures, gain occurs in a narrow bandgap region (~0.35 eV at 300 K), so the electric field must be kept low to prevent band-to-band tunneling.

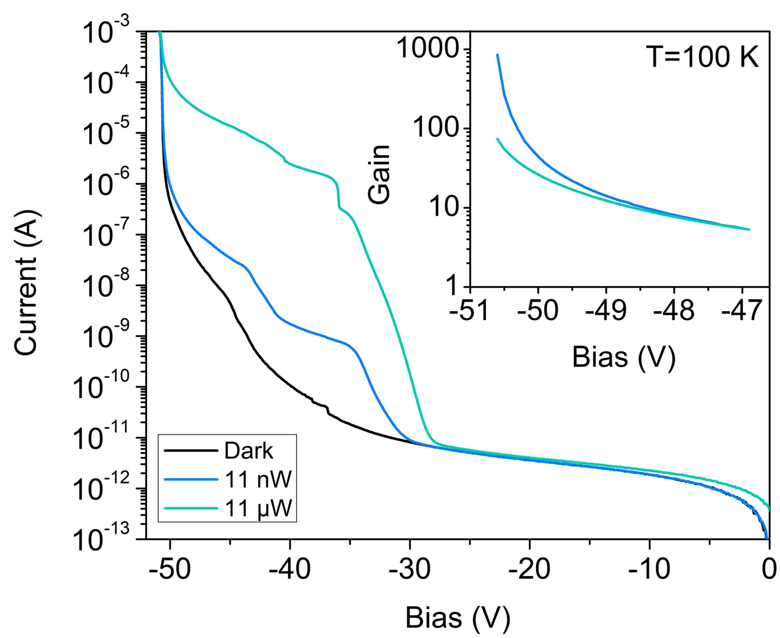

Figure 4.5: Current-voltage characteristics at 100 K under blackout conditions and ~11 nW and ~11 μW of 2-μm illumination. The inset contains the corresponding gains for the two illuminations.

Excess noise measurements were performed with an Agilent 8973 noise figure analyzer in a cryogenic chamber. A 150-μm diameter device was measured at 100 K under 517-nm illumination from a temperature-stabilized fiber-coupled laser diode. This wavelength was chosen to ensure complete absorption before the multiplier to avoid mixed injection, which would alter the measurement. Like the I-V measurements, the light was focused with a fiber lens to a spot size smaller than the mesa diameter. Results of this measurement are displayed in Figure 4.6, along with the theoretical scaling of k=0 through k=0.06 using the local-field model[19]. The excess noise with this device scales with a low k of ~0.04, similar to the previously published results for $Al_{0.7}InAsSb$ multipliers[29,34] and the known low k of ~0.01 for Si[57,58].

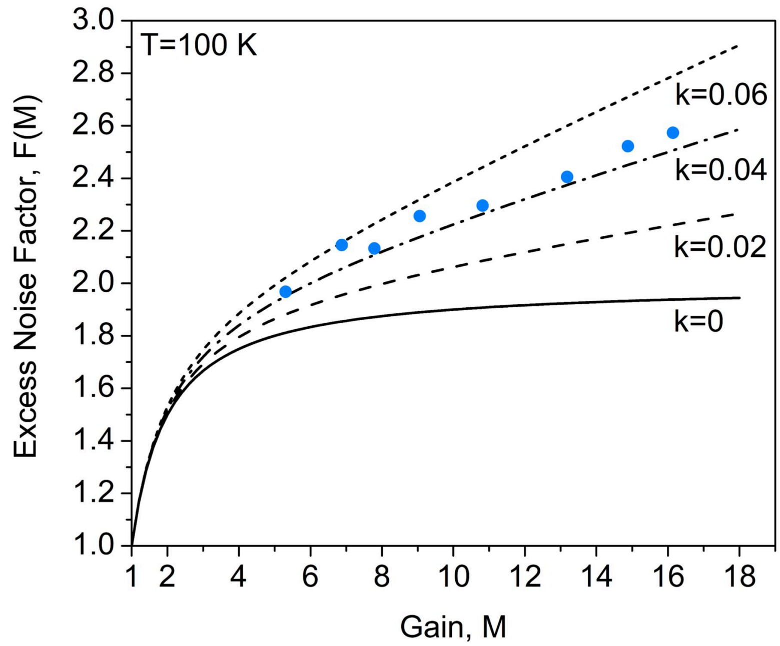

Figure 4.6: The measured excess noise factor versus gain for a 150-μm diameter device under 517-nm illumination at 100 K.

Using the known gain of 5.3 at -46.9 V, determined from the excess noise measurement, the unity-gain external quantum efficiency for this device at 2-μm is 49% (0.79 A/W) at -46.9 V. Improvement to this external quantum efficiency can be explored using (8). The top surface of this device is GaSb, which has a reflectivity of ~35% at 2 μm[59]. With a 1%-reflectivity AR coating, the unity-gain external quantum efficiency can be increased to ~74% (1.2 A/W). Alternatively, if the absorber thickness is increased from 525 nm to 1 μm, the external quantum efficiency can be increased to ~64% (1.04 A/W). Compared to our group's previously reported $Al_{0.15}InAsSb$-based SACM, this device has a unity-gain EQE of ~49% at 2 μm with a 525-nm thick absorber. In contrast, the previous structure has a unity-gain EQE of ~47% for a 1-μm thick absorber. A slightly higher unity-gain EQE is achieved in the new structure with an absorber half as thick. This improvement is likely due to the smaller bandgap of $Al_{0.05}InAsSb$ compared to $Al_{0.15}InAsSb$.

The relative spectral response near cutoff was assessed using double-modulated Fourier-transform IR (FTIR) spectroscopy at 100 K. Using the known unity-gain EQE of 49% (0.79 A/W) at 2 μm, the relative spectral response was converted to EQE, and the result is plotted in Figure 4.7. The peak unity-gain EQE of this detector is ~54% (1.02 A/W) at ~2.35 μm and ~24% (0.58 A/W) at 3-μm. Using a 1%-reflectivity AR coating could improve the unity-gain EQE of this detector to 82% (1.56 A/W) at 2.35 μm and 37% (0.9

A/W) at 3 μm. The cutoff wavelength of InAs at 77 K is ~3 μm, and for $Al_{0.15}InAsSb$ at 240 K, the cutoff is ~2.9 μm. This device has a cutoff at 100 K of ~3.5 μm, which is particularly useful as it allows for the detection of 3-μm light.

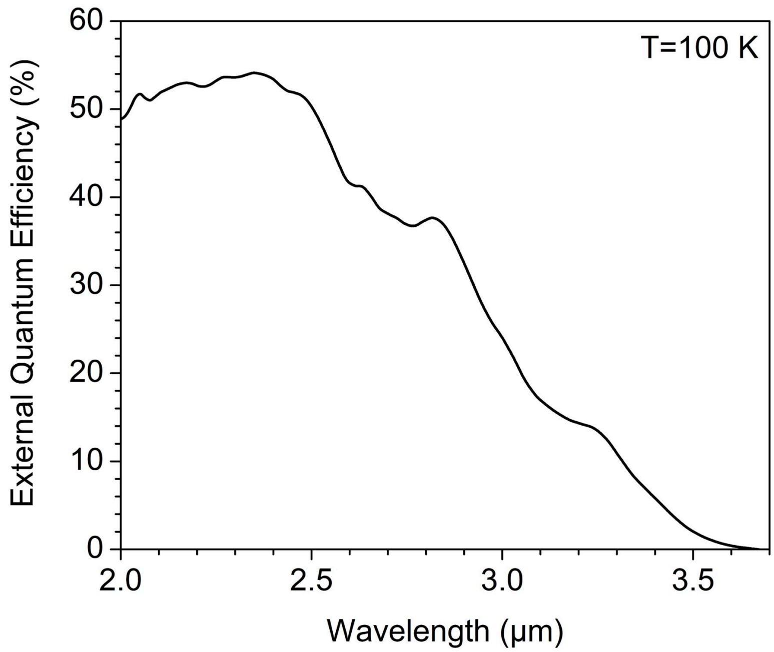

Figure 4.7: The measured unity-gain external quantum efficiency of a 250-μm diameter device at 100 K.

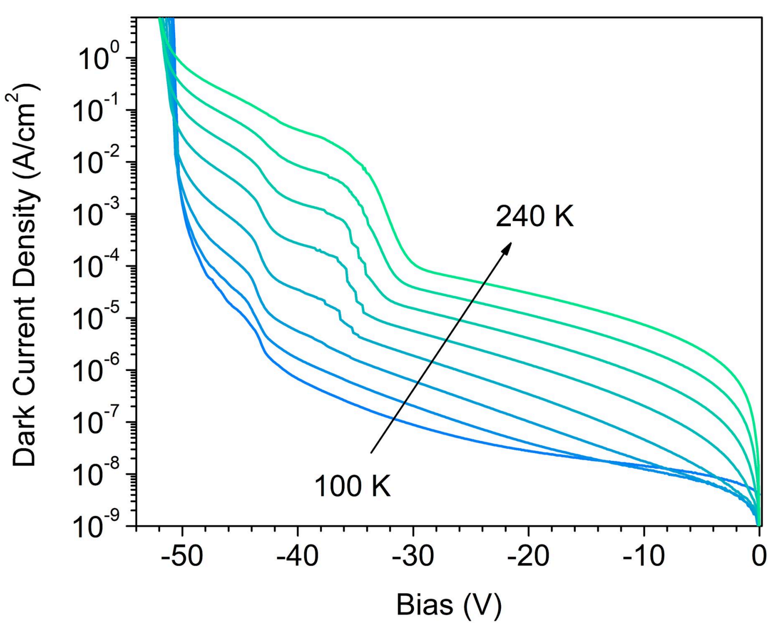

Figure 4.8: The dark current density versus voltage for a 150-μm diameter device from 100 K to 240 K in 20-K increments.

The dark current density (DCD) versus voltage for this device was measured from 100 K to 240 K in 20-K increments using an HP 4145 semiconductor parameter analyzer in a cryogenic chamber. The results of this measurement are displayed in Figure 4.8. Using the gain from the inset of Figure 4.5, the gain-normalized DCD for this device, at 100 K, at a gain of 10 is ~0.03 mA/cm^2, and at a gain of 850 is ~0.05 mA/cm^2. Compared to our previous $Al_{0.15}InAsSb$-based SACM, this device has a gain-normalized DCD of more than two orders of magnitude lower, 0.05 mA/cm^2 compared to 6 mA/cm^2. Table 4.1 below summarizes the results of this device with comparisons to the $Al_{0.15}InAsSb$-based SACM[54], two state-of-the-art InAs APDs[24,56], and a state-of-the-art HgCdTe-based APD[60].

In this chapter, I have presented the design for a $Al_{0.05}InAsSb$-based SACM APD and demonstrated its performance for operation in the MWIR. This device is the first AlInAsSb-based SACM APD capable of efficiently absorbing 3-µm light; the unity-gain EQE is 24%. Compared to InAs, my device achieves a higher gain and a longer cutoff wavelength. Compared to our group's $Al_{0.15}InAsSb$-based SACM, my device has a gain normalized DCD over two orders of magnitude lower. Additionally, at 2 µm, my device has a unity-gain EQE of ~49% with a 525-nm thick absorber compared to ~47% for the $Al_{0.15}InAsSb$-based SACM with a 1-µm thick absorber. It achieves a slightly increased unity-gain EQE for an absorber nearly half as thick.

Table 4.1: The $Al_{0.05}InAsSb$-based SACM APD compared to other MWIR APDs.

Ref.	Material	Operating Temperature (K)	Maximum Gain	Gain-normalized DCD (mA/cm^2)	Cut-off Wavelength (µm)
This device	**$Al_{0.05}InAsSb$**	**100**	**850**	**0.05**	**~3.5**
24	InAs	77	27	0.005	~3
56	InAs	200	330	0.4	~3.2
54	$Al_{0.15}InAsSb$	100	380	6.0	~2.9
60	HgCdTe	77	5300	0.001	~5

5 Excess Noise of Staircase APDs

In this chapter, I will demonstrate experimental measurements of the excess noise factor of so-called staircase avalanche photodiodes performed at an operating frequency of 70 kHz. This low operating frequency ensured the excess noise measurements were performed under the 3-dB bandwidth of the staircase APD devices. These measurements were enabled by the low-frequency setup that I developed and described in the APD Noise Considerations chapter. The staircase avalanche photodiode was first proposed by Federico Capasso in the 1980s, intended as a low-noise solid-state replacement for a photomultiplier tube (PMT)[61]. Figure 5.1 shows a qualitative energy band diagram for such a device under zero bias (a) and reverse bias (b). The namesake of the staircase APD is visible in Figure 5.1(b), as the conduction band looks like a staircase.

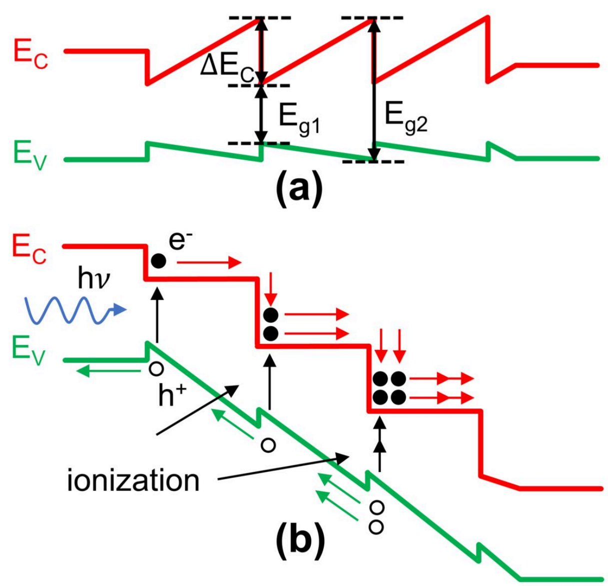

Figure 5.1: (a) Energy band diagram of unbiased staircase APD and (b) illustration of localized impact ionization under reverse bias.

The large steps in the conduction band are designed to deterministically induce an impact ionization event for electrons, while the holes remain largely unaffected by the relatively flat valence band. In this sense, a staircase APD acts like a PMT, as only electrons contribute to the gain. Additionally, the conduction band steps create spatially deterministic impact ionization like the dynodes in a PMT. In such a device where the probability of impact ionization differs for each step, the gain can be represented by

$$M = \prod_{i=1}^{N} (1 + p_i) \tag{26}$$

where p_i is the probability of impact ionization at the i^{th} step, and N is the number of steps. With the assumption of equal impact ionization probability at each step (26) can be simplified to

$$M = (1 + p)^N \tag{27}$$

With a unity probability of impact ionization at each step, the equation reduces to $M = 2^N$. Since the gain for this device is more deterministic than a conventional APD, the excess noise factor of the device should be lower as the noise in a conventional APD arises from the spatial variance of impact ionization. Several theories have been proposed for the theoretical excess noise of staircase APDs[20,21,62–64]. The most general form for the excess noise of a staircase APD with different probabilities of impact ionization at each step is[21],

$$F(N,p) = 1 + \frac{\mathrm{var}(1 + p_1)}{(1 + p_1)^2} + \sum_{i=2}^{N} \left(\frac{\mathrm{var}(1 + p_i)}{(1 + p_i)^2 \prod_{k=1}^{i-1} (1 + p_k)} \right) \tag{28}$$

where $\mathrm{var}(1 + p_i)$ is the variance in multiplication at the i^{th} step. Assuming the same probability of impact ionization at each step yields a simplified form of (28),

$$F(N,p) = 1 + \frac{\mathrm{var}(1 + p)}{p(1 + p)} \left(1 - \frac{1}{(1 + p)^N} \right). \tag{29}$$

Finally, as shown by Teich et al.[21], $\mathrm{var}(1 + p) = p(1 - p)$, which substituted into (29), gives the final expression for the excess noise factor of a staircase APD,

$$F(N,p) = 1 + \left(\frac{1 - p}{1 + p} \right) \left(1 - \frac{1}{(1 + p)^N} \right). \tag{30}$$

In the case of unity probability at each step, the excess noise factor reduces to one. Compared to a best-case k=0 traditional APD, in which the excess noise asymptotically approaches two, staircase APDs should have an excess noise factor two times lower.

5.1 Initial Excess Noise Factor Characterization

Initially, Capasso et al. used $Al_xGa_{1-x}As/GaAs$ to fabricate the staircase band structures[61,65]. Unfortunately, the $Al_xGa_{1-x}As/GaAs$ conduction band discontinuity is insufficient to allow carriers to impact ionize in GaAs, particularly for high-energy electrons scattered to satellite valleys[66]. Recently, Ren et al. and March et al. have realized 1-[67], 2-, and 3-step[68] staircase APDs with gains of ~2, ~4, and ~7, respectively, using the AlInAsSb materials system. Figure 5.2(a) shows the measured gain for these devices. Figure 5.2(b) shows the measured noise power spectral density (NPSD) for the staircase devices compared to models and measurements for the best-case PMTs and a best-case k=0 APD. The NPSD was measured under 543-nm laser illumination with a noise figure analyzer in a setup depicted in Figure 2.4(a). The NPSD for the staircase devices is significantly lower than both k=0 APDs and PMTs and appears to scale linearly with gain. In fact, this noise is much lower than predicted in (1) with an excess noise like that in (30). Even with an excess noise factor of 1, the best-case scenario for a staircase APD, the NPSD should still scale quadratically with gain, not linearly.

Regarding this discrepancy, a third party suggested that the bandwidth of the devices may be too low for the 50 MHz measurement frequency used. In response, I performed several measurements to evaluate this concern. First, I measured 2- and 3-step devices at a lower frequency, 15 MHz, and the measured noise was the same as at 50 MHz. Second, I sent a 3-step device to John David's group at the University of Sheffield, a well-known APD research group, to perform measurements at 10 MHz. The resulting noise measurement was very similar to the previous two measurement frequencies. Third, I measured the NPSD versus photocurrent for a PIN photodiode, which should have lower noise than an

APD, to ensure the measurement setup has high enough sensitivity. The NPSD for the shot noise of a PIN photodiode is the following:

$$\mathrm{NPSD} = 2q\left(I_{\mathrm{photo}} + I_{\mathrm{dark}}\right)R \tag{31}$$

where R is the system impedance (50 Ω). For increasing light intensity, the NPSD of the PIN scaled linearly, as expected, confirming that the NFA-based setup had high enough sensitivity for measuring the shot noise of PIN photodiodes and APDs. This measurement is displayed in Figure 5.3 below. Also plotted (dashed line) is the calculated NPSD using the measured photocurrent and a system impedance of 50 Ω.

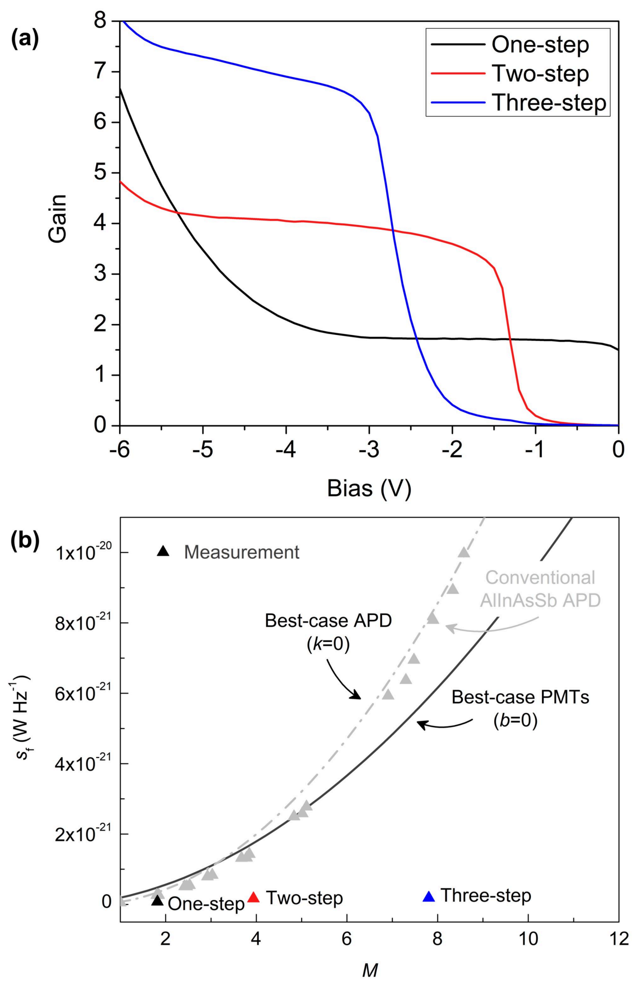

Figure 5.2: (a) The measured gain versus bias for 1-, 2-, and 3-step staircase avalanche photodiodes, and (b) the measured noise power spectral density for 1-, 2-, and 3-step staircase avalanche photodiodes[68] [Nat. Photonics **15**, 468-474 (2021)].

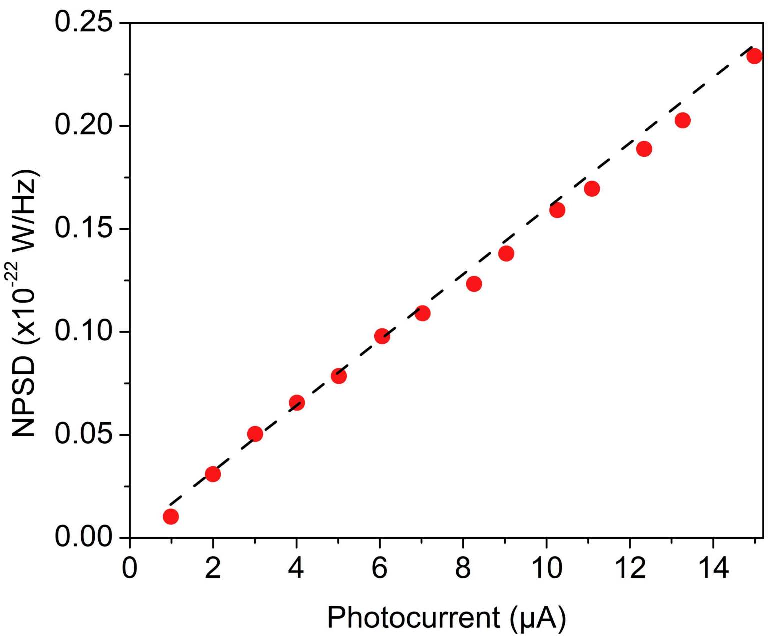

Figure 5.3: The Noise Power Spectral Density versus photocurrent for a $Al_{0.7}InAsSb$-based PIN photodiode. The dashed line is the calculated NPSD, using (31), based on the measured photocurrent and an impedance of 50 Ω.

From these three tests, it seemed that 1) the bandwidth of the staircase devices was high enough for the chosen measurement frequency, and 2) the noise figure analyzer had high enough sensitivity to measure the noise of the devices correctly.

To get a conclusive answer, I needed to measure the bandwidth of the staircase devices directly. Finding a suitable modulation scheme for this measurement was non-trivial as the traditional lithium niobate modulators are 1) designed to operate at much higher frequencies than 10s of MHz and 2) designed for near-infrared operation, not visible. Lithium niobate modulators were not an option, so I directly modulated a laser diode at 635 nm with a signal generator. The resulting bandwidth measurements for a 2- and 3-step staircase detector are shown in Figure 5.4. The measured 3-dB bandwidths for the 2- and 3-step devices were ~5 MHz and ~0.8 MHz, respectively, much lower than the measurement frequencies used for NPSD measurements. As the minimum frequency of our noise figure analyzer is 15 MHz, a new noise setup, operating in the kHz range, was needed to measure the noise of the staircase devices correctly. This setup was described above in the APD Noise Considerations chapter.

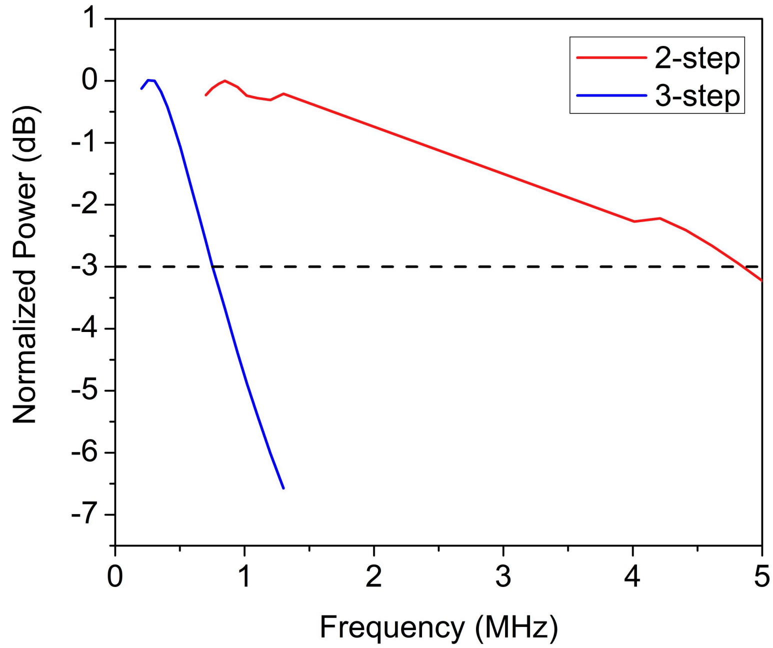

Figure 5.4: The normalized power versus frequency for 2- and 3-step staircase avalanche photodiodes.

The noise for 2- and 3-step staircase APD devices was measured at a low frequency of around 70 kHz to ensure the devices were not bandwidth-limited. The TIA was set to the low-noise performance range with a trans-impedance of 10^5 V/A. The SA center frequency was 69.4 kHz with a resolution bandwidth of 47 Hz. This measurement frequency was selected because the system noise floor was low enough to detect the noise of the DUT. For reference, the system noise floor was about -116.1 dBm, and the lowest measured noise for either of the control structures was -114.9 dBm.

5.2 Low-frequency Excess Noise Factor Characterization

For all measurements, a bias of -2.5 V was used for the 2-step and its control, and a bias of -4 V was used for the 3-step and its control. These biases yield the maximum gain in each of the staircase structures. By using the same bias for both the control and its staircase, we ensure the control has the same depletion characteristics as the staircase, directly comparing only the signal and noise performance. All devices were illuminated with 543-nm light from a He-Ne continuous-wave laser, and all measurements were performed at room temperature.

The shot noise powers for an APD and a PIN are shown in (32) and (33), respectively. The equations are like (1), except the system impedance, R = 50 Ω, has been introduced and the multiplied photocurrent is used as explained above in the APD Noise Considerations chapter.

$$N_{\text{APD}} = 2q\left(I_{\text{photo}} + I_{\text{dark}}\right)R\Delta f MF(M) \tag{32}$$

$$N_{\text{PIN}} = 2q\left(I_{\text{photo}} + I_{\text{dark}}\right)R\Delta f \tag{33}$$

To measure the excess noise of the 2- and 3-step staircase APDs, the noise versus photocurrent was first measured for the corresponding control structure. The control structure is simply a PIN photodiode producing a unity gain and unity excess noise. By varying the incident light power and thus the photocurrent, the noise power of the control structures was measured corresponding to $2q\left(I_{\text{photo}} + I_{\text{dark}}\right)R\Delta f + N_{\text{system}}$. When plotting the measured noise versus photocurrent, there is a y-intercept at zero photocurrent corresponding to the dark noise contributions and any system noise. By subtracting the intercept, we are left with a line that scales linearly with photocurrent and represents $2qI_{\text{photo}}R\Delta f$. These are the “Control photo” lines in Figure 5.5(a,b).

A similar measurement was performed for the staircase APD. With the staircase APD biased to achieve maximum output photocurrent, the device was illuminated with the same intensities exposed to the control. The staircase APD gain is its measured output photocurrent divided by the photocurrent of its control under the same illumination. The noise power was also measured at each intensity and corresponded to $2q\left(I_{\text{photo}} + I_{\text{dark}}\right)R\Delta f MF(M) + N_{\text{system}}$, the “n-step total” line in Figure 5.5(a,b). The intercept of the "n-step total" line corresponds to the dark noise of the staircase APD and any system noise contributions. By subtracting the intercept, we get the "N-step photo” lines in Figure 5.5(a,b), which are the photo noise power of the staircase devices corresponding to $2qI_{\text{photo}}R\Delta f MF(M)$.

At the same input light powers, the measured control noise corresponds to $2qI_{\text{photo}}R\Delta f$. The measured staircase APD noise corresponds to $2qI_{\text{photo}}R\Delta f MF(M)$. Therefore, the excess noise factor of the staircase APD can be calculated by dividing the measured noise of staircase APD by the measured noise of the control and the gain of the staircase APD, $F(M) = N_{\text{staircase}}/N_{\text{control}}M$. This method for determining $F(M)$ accounts for any uncertainties with system gain and bandwidth and any noise contributions from the laser source[44]. Since the staircase APD noise is divided by the control noise, these uncertainties will be canceled, and only the excess noise intrinsic to the staircase device will remain. This method is preferred for determining $F(M)$ compared to direct calculation with (32).

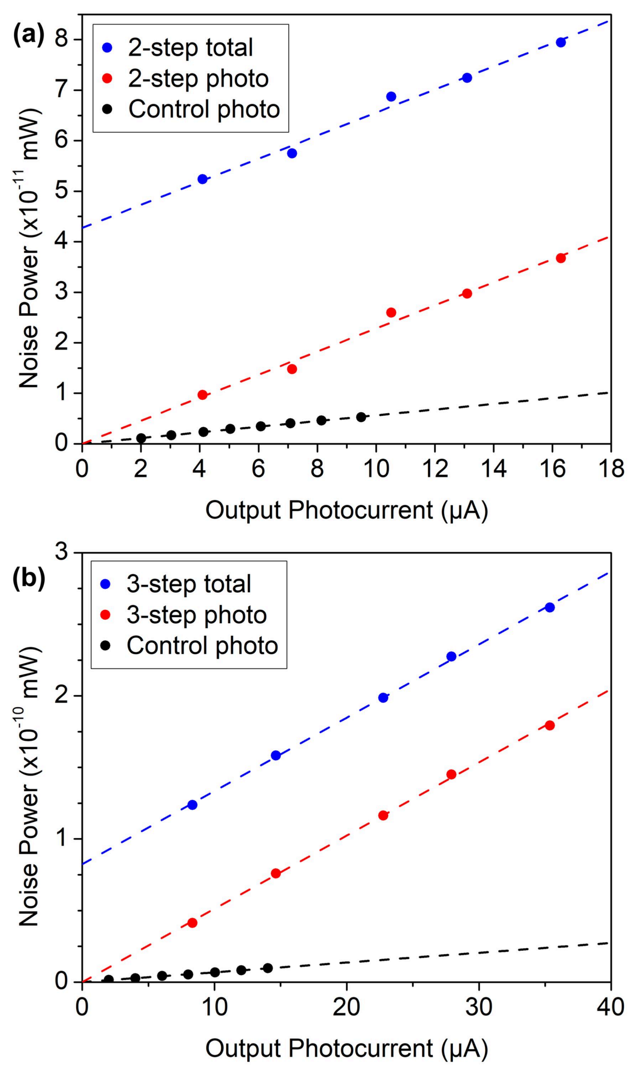

Figure 5.5: (a) The measured noise power for a 2-step staircase APD and its control, and (b) the measured noise power for a 3-step staircase APD and its control.

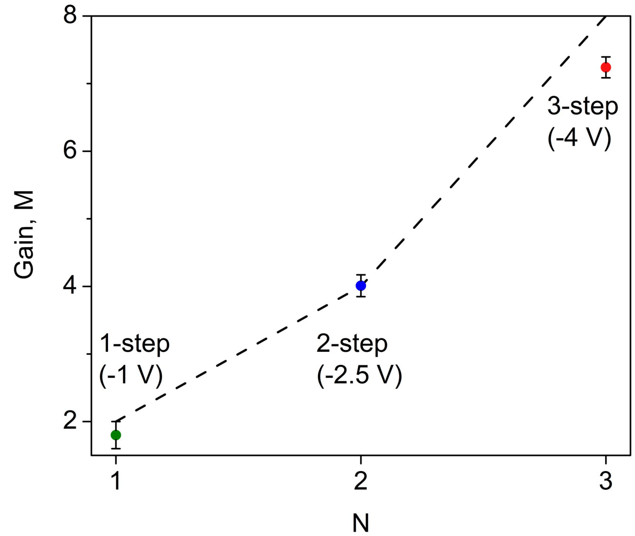

Figure 5.6: The theoretical, 2^N, gain, and measured gain for a 1-[67], 2-, and 3-step staircase APD. The bias needed to reach the plotted gain is in parentheses.

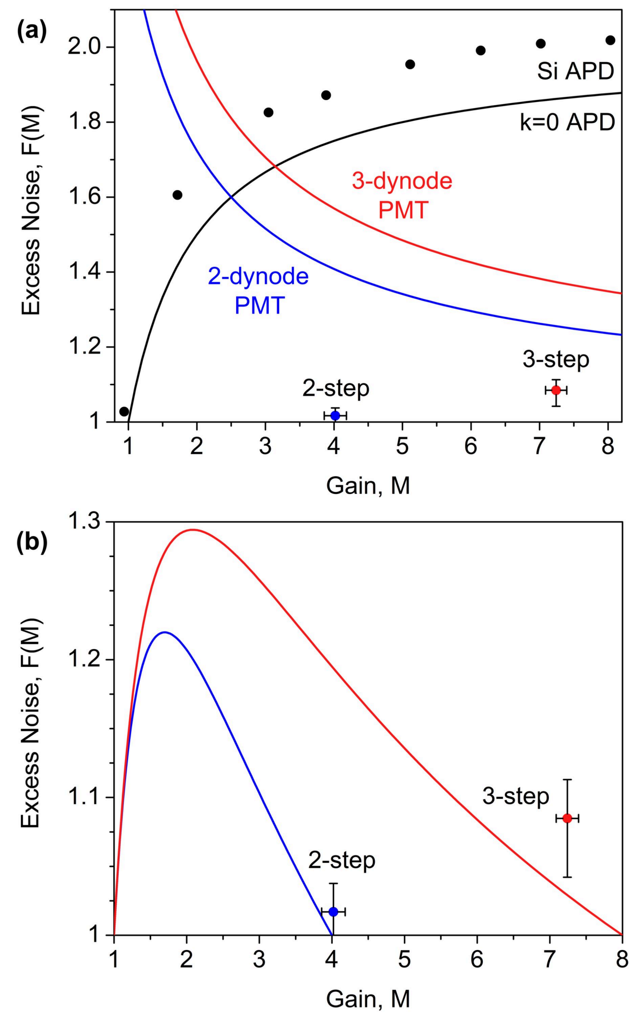

Figure 5.7: (a) The measured excess noise factor for a 2- and 3-step staircase APD compared to the excess noise, based on (3), of a k=0 conventional APD, a Si APD[29], and the theoretical excess noise of two best-case PMTs ($A = 10$, $D = \infty$)[21]. (b) The measured excess noise compared to the theoretical excess noise for a 2- and 3-step staircase APD.

Four devices were measured for both the 2- and 3-step staircase structure, and their excess noise was averaged. The measured average excess noise factors for the 2- and 3-step staircase APDs are 1.02 and 1.08, respectively. The corresponding average gains for the 2- and 3-step staircases are 4.01 and 7.24. The gain for a previously reported 1-step[67], as well as the gains for the 2- and 3-step staircase APDs, are plotted with the theoretical, 2^N, gain in Figure 5.6.

Figure 5.7(a) shows the measured excess noise compared to the theoretical scaling of the best-case k=0 conventional APD based on the local field model[19], (3). Also plotted is the excess noise of a Si APD[29] and two best-case high-gain first-dynode PMTs with 2- and 3-dynodes. For both PMTs, the gain of the first dynode, A, equals 10, and the "degrees-of-freedom," D, is ∞ (the least noisy)[21]. This "degrees-of-freedom" describes the variability of secondary-emission efficiency across the surface of the dynode[21]. The measured excess noise of both staircase APDs is much lower than that of the best-case k=0 conventional APD and both best-case PMTs. Figure 5.7(b) shows the measured excess noise compared to the theoretical excess noise of staircase APDs expressed in (30). Instead of plotting directly versus the probability, p, the average gain was first calculated from the expression $M = (1 + p)^N$ and used. There is excellent agreement between the theoretical and measured noise for the 2- and 3-step staircase APDs.

In this chapter, I have demonstrated experimental measurements of staircase APDs at 70 kHz. For a 2- and 3-step device with an average gain of 4.01 and 7.24, the measured excess noise factors were 1.02 and 1.08, respectively. These measurements agree well with the theoretically predicted noise of staircase APDs predicted by Capasso et al.[20] and Teich et al.[21] This measurement was made possible due to my development of a new excess noise setup capable of measuring noise at operating frequencies in the 10s to 100s of kHz. Future iterations of this structure offer exciting implications for receiver sensitivities. First, due to the exponential gain scaling in staircase APDs, each additional staircase step added to the structure has the potential to double the gain. With the same near-unity excess noise factor, a future staircase APD design with four or five steps would provide double or quadruple the gain of a three-step device while maintaining a receiver system that is still circuit noise limited.

6 SACM Staircase APDs

With the multistep staircase APDs, I have demonstrated devices with an excess noise factor ~2 times lower than a traditional best-case k=0 APD. This lower excess noise factor reduces device shot noise, as seen in (1), leading to an overall increase in the APD signal-to-noise ratio. However, since this device uses $Al_{0.7}InAsSb$ as the absorber material (~1 μm cutoff), the absorber is limited to visible and NIR detection. With the MWIR SACM APDs, I have demonstrated a device capable of detecting MWIR light out to 3.5 μm with gains up to 850 with a k-factor of ~0.04. This device achieves gains more than double state-of-the-art InAs detectors and gain-normalized dark current densities over two orders of magnitude lower than our previously reported MWIR Al0.15InAsSb-based detector. While this device has a low k-factor near 0, it still has an excess noise factor ~2 times higher than achievable with a staircase multiplier. The natural conclusion is to make a hybrid device, combining the low excess noise multiplication of the staircase multiplier with the MWIR absorption capabilities of the MWIR SACM APD.

6.1 Design

Working with our collaborators at the University of Texas at Austin, a proposed design for such a device was created incorporating $Al_{0.15}InAsSb$ as the absorber and a 2-step staircase structure as the multiplier. This device should be able to detect MWIR light up to ~3 μm and give a gain of ~4 with a near unity excess noise factor. We call this device a SACMcase as it can detect and amplify IR light like a SACM APD and is composed of a staircase multiplier. The design for the SACMcase and a control structure are displayed in Figure 6.1. The control structure is nearly identical to the SACMcase, except the staircase region has been replaced with $Al_{0.7}InAsSb$. Like staircase APDs, this control structure is used to calculate the gain of the SACMcase by dividing the photocurrent of the SACMcase by the photocurrent of the control at each bias point. Figure 6.2 shows the energy band diagram of the structure under -3.5 V of bias. Regions corresponding to the absorber, charge grading, and staircase multiplier have been labeled.

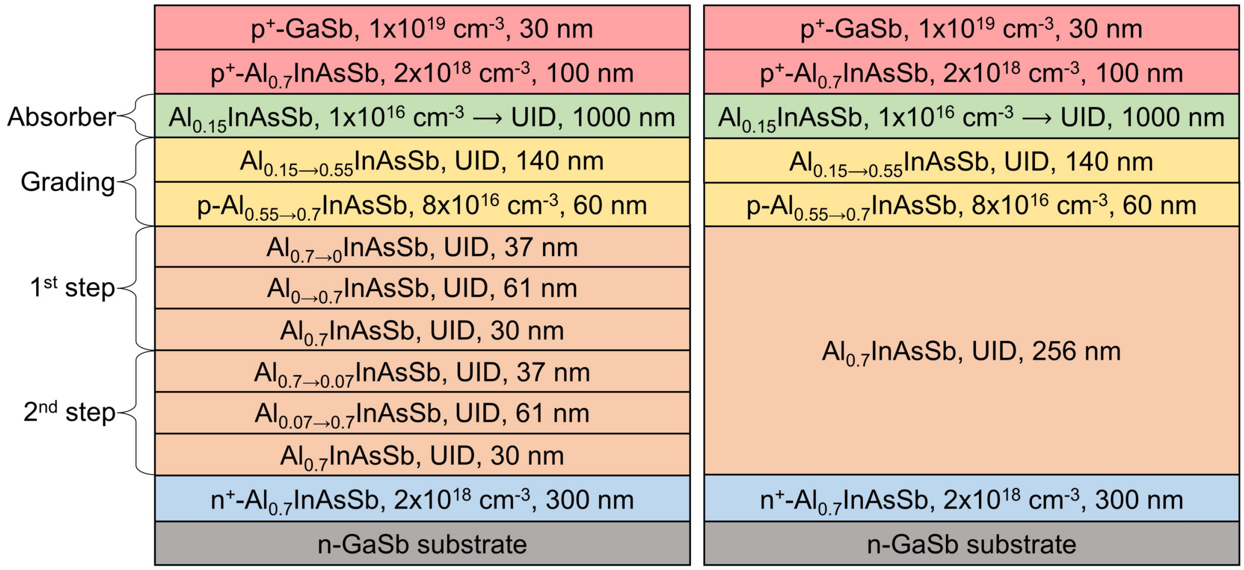

Figure 6.1: Schematic cross-sections of the SACMcase epitaxial layer structure (left) and control structure (right) with labeled absorber, grading, and staircase step regions.

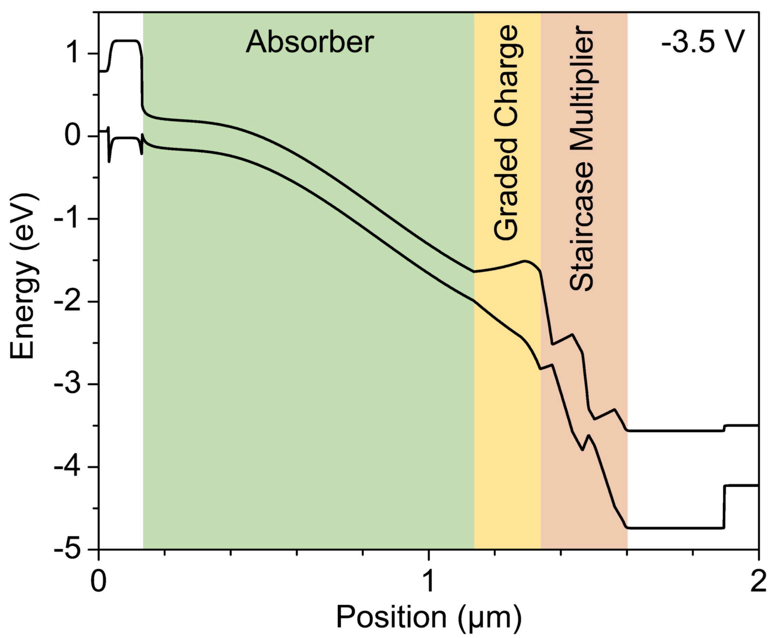

Figure 6.2: Simulated energy band diagram of the SACMcase under 3.5 V reverse bias with labeled absorber, grading, and staircase multiplier regions.

6.2 Characterization

Devices were fabricated using the process detailed in Appendix 1: Device Fabrication. As previously reported for staircase devices, the gain of the SACMcase device was determined by comparing its photocurrent with that of a control device having no steps in the multiplier region[69,70]. This gain, along with current-voltage curves of the control and SACMcase structures, are shown in Figure 6.3. The control must be under sufficient bias for the photogenerated electrons to overcome the graded charge layer, demonstrated by the abrupt rise in current near -2 V. The gain of the SACMcase is determined beyond -2.8 V, the bias point where the steps have sufficiently flattened to initiate impact ionization. At a gain of 4, the SACMcase can produce approximately 200% multiplied external quantum efficiency (EQE) at 1550 nm without additional AR enhancement. GaSb presents a reflectance of about 0.34 at this wavelength[71], indicating that with a 1% AR coating, the SACMcase could provide a multiplied EQE of nearly 300% at a gain of 4. The EQE could be further improved by increasing the thickness of the absorber region.

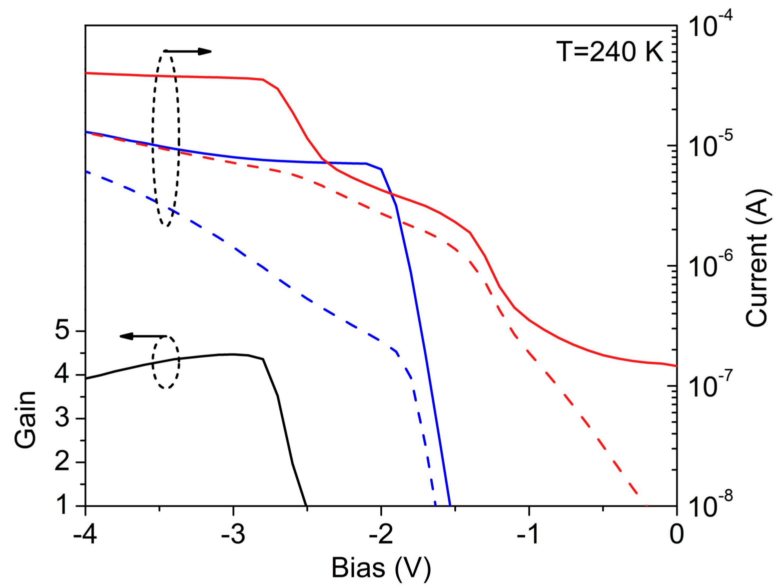

Figure 6.3: Current-voltage curves of the control (blue) and SACMcase (red) devices. Dark current curves are dashed, and 1550-nm illuminated curves are solid. The resulting gain is shown in black. Measurements are of 150-µm-diameter devices at 240 K.

Figure 6.4 shows the dark current of a 150-µm diameter device as a function of temperature, indicating a three-order-of-magnitude decrease in dark current from 300 K to 100 K at -3 V. This reduction suggests that band-to-band tunneling is not the predominant dark current mechanism in the operating range. Variable area diode analysis was performed at 240 K to extract the bulk and surface-leakage current contributions to the dark current of the SACMcase devices.

Figure 6.5(a) shows the current-voltage characteristic at 240 K for five different-size devices. From -3 V to -5 V in -0.5-V increments, J_{bulk} and J_{surface} were fit using (11) for different diameter devices. For all fits, $R^2 > 0.9998$. The fitted J_{bulk} and J_{surface} are plotted as an inset of Figure 6.5(a). At -3 V, where the gain of the SACMcase plateaus, the values for J_{bulk} and J_{surface} are 3.38x10^{-2} A/cm^2 and 5.27x10^{-5} A/cm, respectively. Using these values, the bulk current, I_{bulk}, and surface-leakage current, I_{surface}, are plotted versus device diameter in Figure 6.5(b). For diameters less than ~62 µm, surface-leakage current dominates, and bulk current dominates for diameters greater than ~62 µm.

To properly characterize the excess noise factor of this device, I first measured its 3-dB bandwidth to see if it was high enough (over 15 MHz) to use the NFA-based setup depicted in Figure 2.4(a) or if I would need to use the low-frequency setup shown in Figure 2.4(b). The bandwidth of the device was measured with a 1550-nm laser diode directly modulated with a signal generator. The resulting 3-dB bandwidth is displayed in Figure 6.6. The 3-dB bandwidth of the SACMcase is ~8 MHz, meaning that I would need to use the low-frequency setup to measure the excess noise of this device correctly.

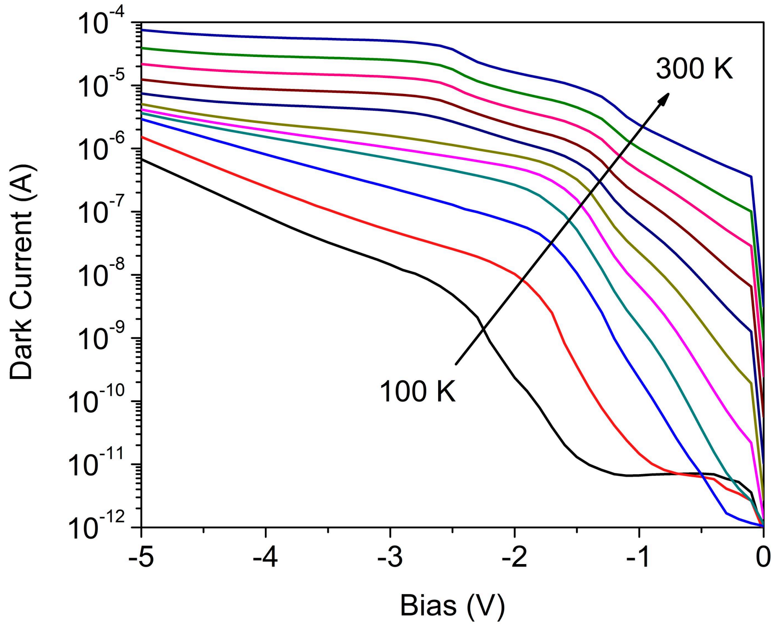

Figure 6.4: Dark current-voltage curves of the SACMcase versus temperature for a 150-µm diameter device from 100 K to 300 K in 20-K increments.

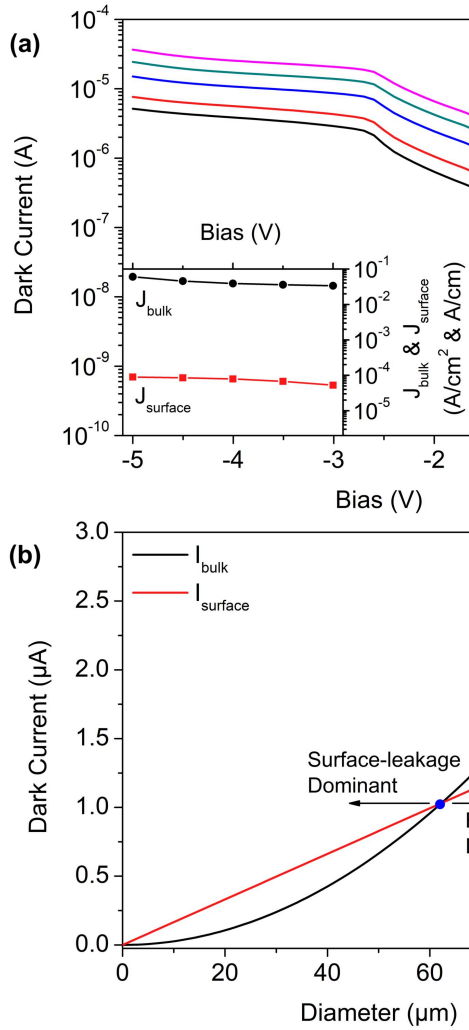

Figure 6.5: (a) Measured dark current, at 240 K, for five different-sized devices (inset) with extracted bulk and surface-leakage current density coefficients. (b) The bulk and surface-leakage current contributions versus device diameter at -3 V with the crossover point between the two contributions indicated at a diameter of 62 µm.

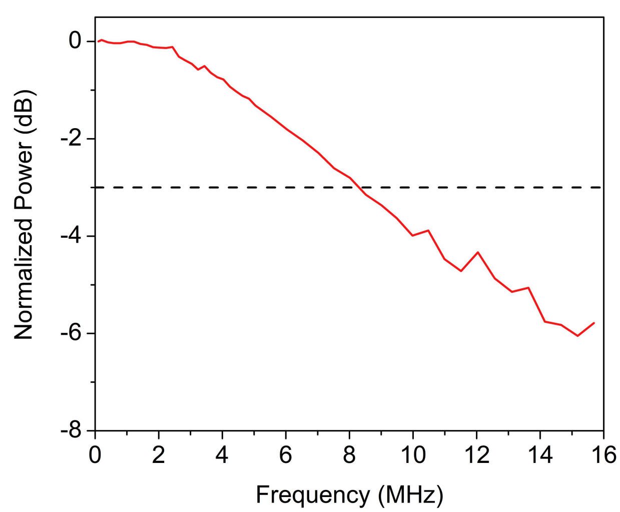

Figure 6.6: The normalized power versus frequency for the 2-step SACMcase device with a 3-dB bandwidth of 8 MHz.

The excess noise factor of the SACMcase was measured in a cryo chamber at 240 K to reduce the dark current. Under 543-nm He-Ne laser illumination, all light was absorbed before the staircase multiplier region. The measurement was performed well below the device bandwidth at an operating frequency of ~70 kHz using the low-frequency noise setup described in the APD Noise Considerations chapter. The SACMcase was biased to -3 V, where the gain curve plateaus. Four devices were measured, and their gain and the excess noise factors were averaged. This measurement was performed the same way as the staircase devices in the Excess Noise of Staircase APDs chapter above, where the noise of a control device was used to calculate the excess noise factor in the SACMcase. Figure 6.7 shows a sample noise measurement plot. The average gain for the four devices was 4.12 with an average excess noise factor of 0.97, falling in line with the 2- and 3-step staircase APD devices I measured in the above staircase noise section. The measured excess noise factor for the SACMcase also agrees with previously predicted theoretical excess noise[21,72]. The excess noise results for the SACMcase are plotted in Figure 6.8 alongside the previously measured 2- and 3-step staircase APDs and the theoretical excess noise for a 2- and 3-step staircase APD[21,72]. Error bars are included, representing the ranges of measured gain and excess noise for the measured devices. Reference curves are also included for excess noise that scales as $k = 0$, $k = 0.1$, and $k = 0.2$.

In this chapter, I have demonstrated a hybrid SACM staircase (SACMcase) APD incorporating two staircase steps with an average gain of 4.12 and an average measured excess noise factor of 0.97. The results achieved in this chapter relied on results from several of the previous chapters. Design considerations for the $Al_{0.05}InAsSb$-based SACM APD chapter helped optimize the charge region thickness and doping concentration in the final SACMcase design. Absorption coefficients obtained in the $Al_{0.15}InAsSb$ PIN chapter helped model the absorber in the SACMcase design. The methodology for measuring the excess noise factor of staircase-step-containing devices was developed in the Staircase Noise chapter. Designs for the low-frequency noise measurement setup used to measure the excess noise factor of the SACMcase were introduced in the APD Noise Considerations chapter.

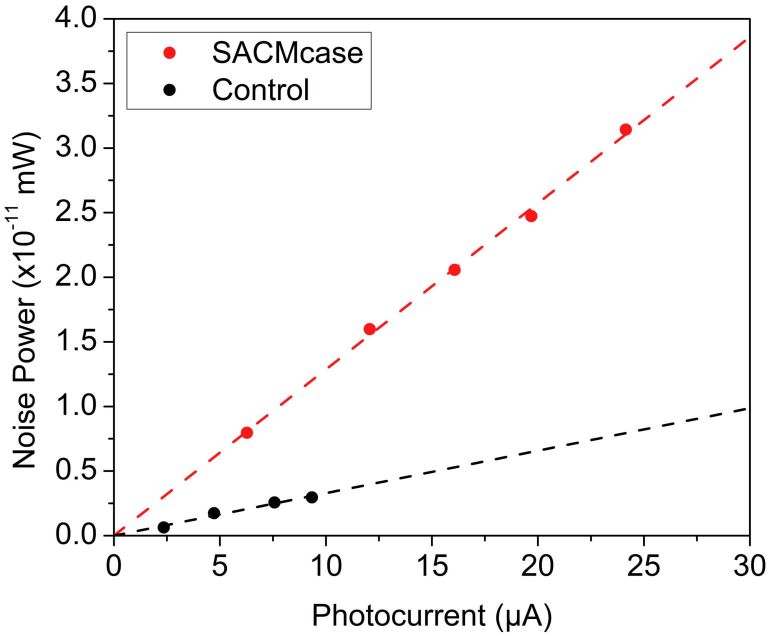

Figure 6.7: The measured noise power of a SACMcase device and control device under the same bias (-3 V) and illumination conditions.

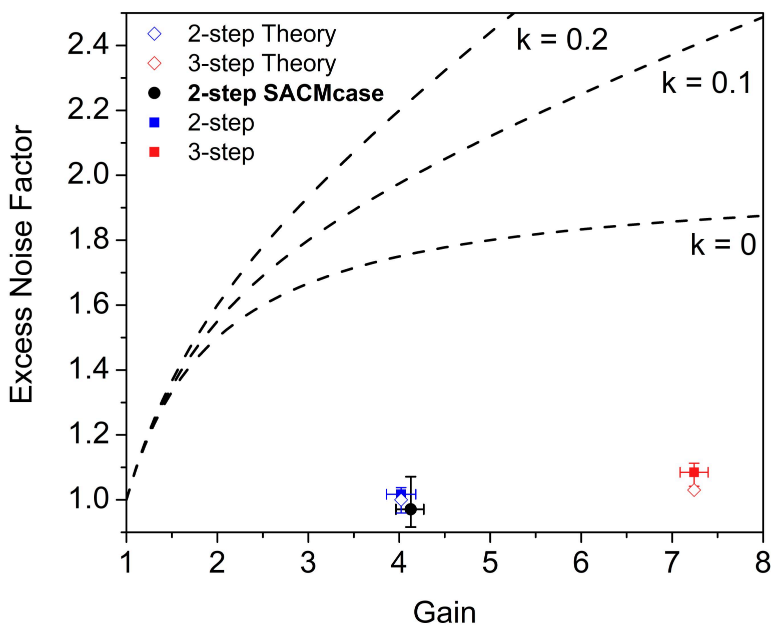

Figure 6.8: The average excess noise factor of four SACMcase devices under 543-nm illumination at 240 K alongside the measured excess noise factor for 2- and 3-step staircase APDs without narrow bandgap absorbers and the theoretical noise for a 2- and 3-step staircase APD. Also included are reference curves for excess noise that scale as $k = 0$, $k = 0.1$, and $k = 0.2$.

7 Cascaded Multiplier APDs

From the Excess Noise of Staircase APDs chapter, I have demonstrated that the excess noise factor of 2- and 3-step staircase APD structures is near unity as theoretically predicted. A maximum gain of ~7.3 was achieved with a 3-step structure. To increase the gain in a staircase structure, additional steps need to be added, each drastically increasing the dark current in the structure due to the narrow bandgap regions needed to form the staircase step. Another approach to increase the gain is to form a "cascaded" structure where a staircase step or steps are placed before a conventional high-electric-field multiplication region. In such a structure, the electrons would first impact ionize one or several times in the staircase steps before entering a high-electric-field conventional region to impact ionize further. In this scheme, the staircase region is akin to a low-noise pre-amplifier before a cascade of other amplifiers used to reduce the overall output noise. It follows that the excess noise factor in this structure would behave similarly to that of the noise factor in cascaded amplifiers based on Friis' equation[73]

$$F_{\text{Total}} = F_1 + \frac{F_2 - 1}{M_1} + \cdots + \frac{F_N - 1}{M_1 M_2 \ldots M_{N-1}} \tag{34}$$

where M_N and F_N are the gain and noise factor of the N^{th} stage in a series of cascaded amplifiers.

7.1 Design

For such a structure to be realized, a sufficient field must first be established in the conventional multiplication region before the staircase steps unfold. As shown in Figure 5.2(a) from the staircase noise section, once the staircase steps have unfolded, the gain flattens out, no longer increasing with bias as in a conventional multiplier. However, increasing bias contributes to increased dark currents from the onset of tunneling in the narrow bandgap region at the bottom of the staircase step. Therefore, a sufficient field should be established, followed by the unfolding of the staircase steps to maximize the potential for gain and minimize excess dark currents from the staircase region. For this cascaded multiplier structure to work, an intermediate positive charge region should be placed between the staircase region and conventional multiplication region to allow for a high electric field to be established in the conventional multiplier before depleting the charge region and subsequent unfolding of the staircase steps. Such a structure was designed by my colleagues at the University of Texas at Austin and is depicted in Figure 7.1(a). This design incorporates one staircase step before the conventional multiplication region. Similar to other structures containing staircase steps, a step-free control structure (Figure 7.1(b)) was also grown, where the staircase step region was replaced with an equally thick $Al_{0.7}InAsSb$ region. This control structure is used to characterize the gain in the cascaded multiplier APD by dividing the photocurrent present in the cascaded multiplier APD by the photocurrent present in the control structure under the same incident light power.

Figure 7.2 shows the simulated energy band diagram of the cascaded multiplier APD at a bias of -25 V. The simulation was performed with Ansys Lumerical CHARGE. The different regions are colored corresponding to the epitaxy layers in Figure 7.1(a). In the figure, the unfolded staircase step is visible, as well as the high-electric-field conventional multiplier.

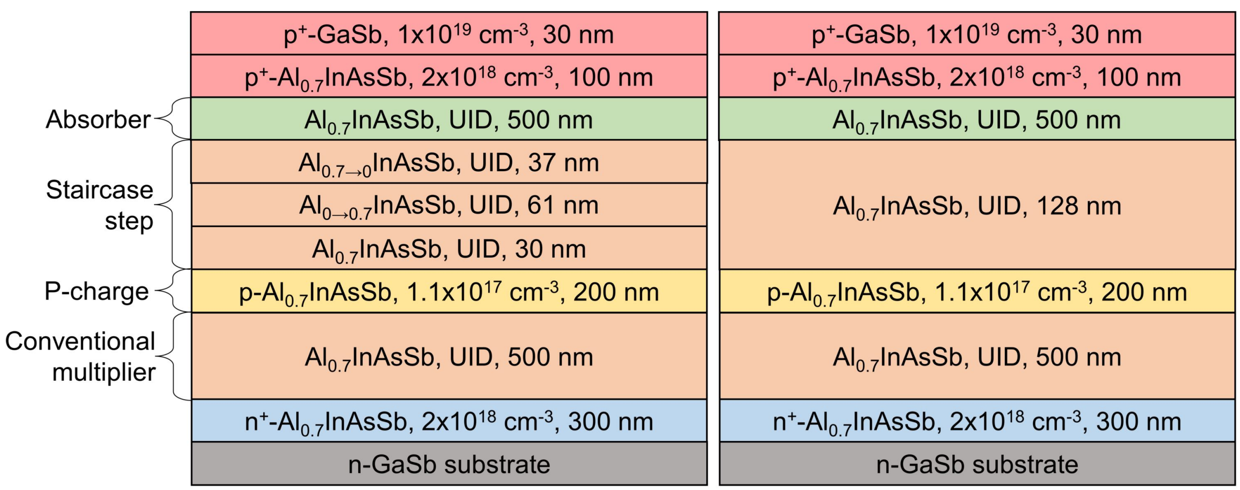

Figure 7.1: The schematic cross-section of the cascaded multiplier APD (left) and its corresponding control structure (right).

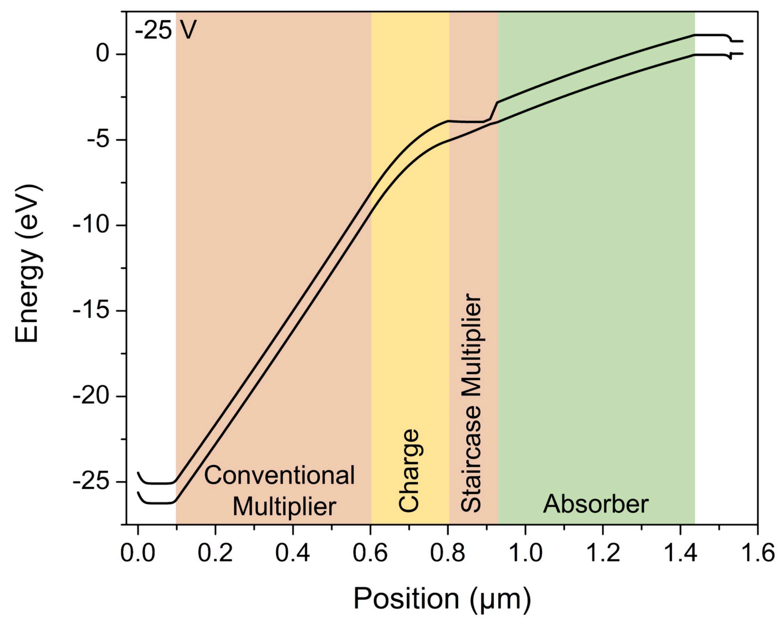

Figure 7.2: The simulated energy band diagram of the cascaded multiplier APD at a bias of -25 V with corresponding epitaxial regions colored and labeled.

7.2 Characterization

Devices were fabricated using the process described in Appendix 1: Device Fabrication using the dry/wet etch technique. To characterize the device performance, I-V characteristics were first measured with a Keithley 2400 SourceMeter at room temperature. Measurements were made under blackout conditions and 543-nm illumination from a He-Ne laser. The cascaded multiplier APD and its control were illuminated with the same incident power, allowing for a direct comparison of the two structures. The measured I-Vs are displayed in Figure 7.3(a). The hump in the control curves around -20 V indicates the device has "punched through" and is depleting into the absorber. The cascaded multiplier curves show a double hump. The first hump around -23 V most likely indicates when the device has depleted through the p-charge region. The second hump around -30 V indicates where the staircase step has fully unfolded, and the device has depleted into the absorber. Figure 7.3(b) shows the photocurrent ratio between the cascaded multiplier APD and its control. For a standard staircase device (one with no charge region or conventional multiplier), this photocurrent ratio would represent the gain. However, these devices operate under a high enough bias that there is likely a sufficient electric field for impact ionization to occur after -25 V, where the devices have initially "punched through" the p-charge region. This high electric field means the control structure likely has a non-unity gain. To get the overall gain of the cascaded multiplier APD, the gain in the control structure must first be determined.

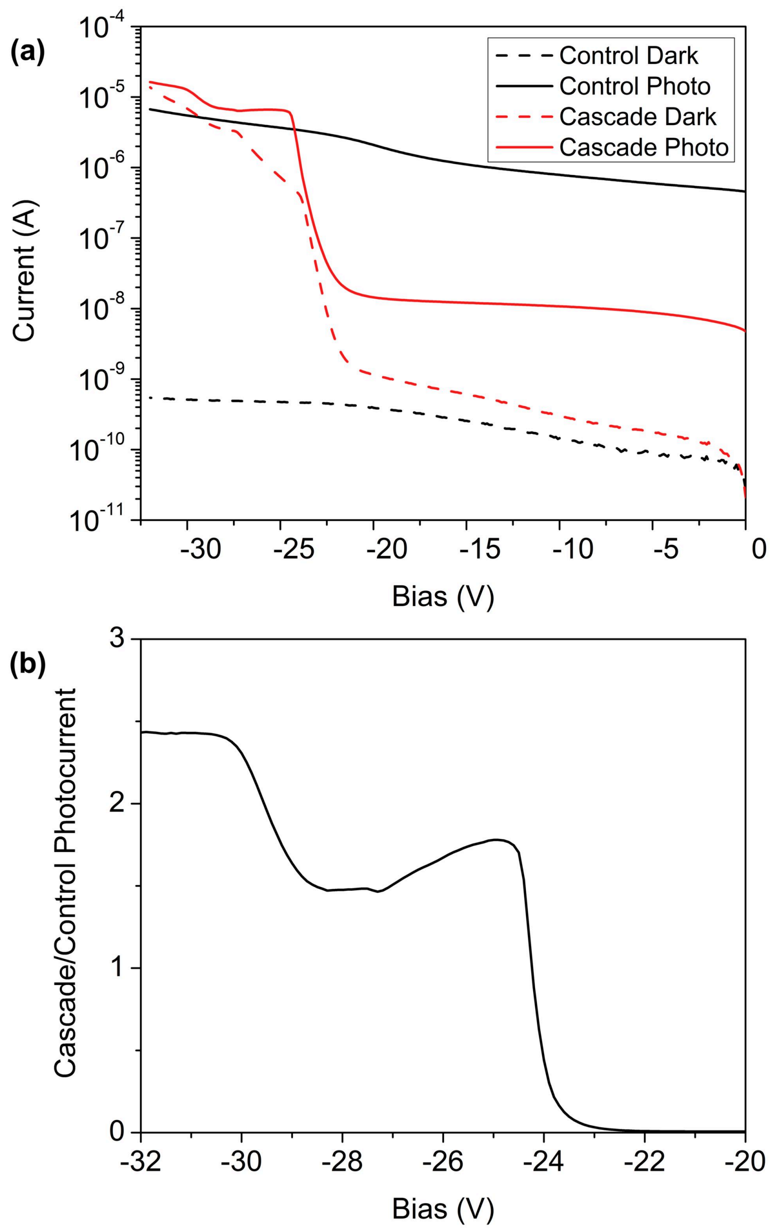

Figure 7.3: (a) The measured current-voltage characteristic for the cascaded multiplier APD and its control. Both devices have a 150-μm diameter and are illuminated with ~31 μW of 543-nm laser light. (b) The photocurrent ratio of the cascaded multiplier APD and its control.

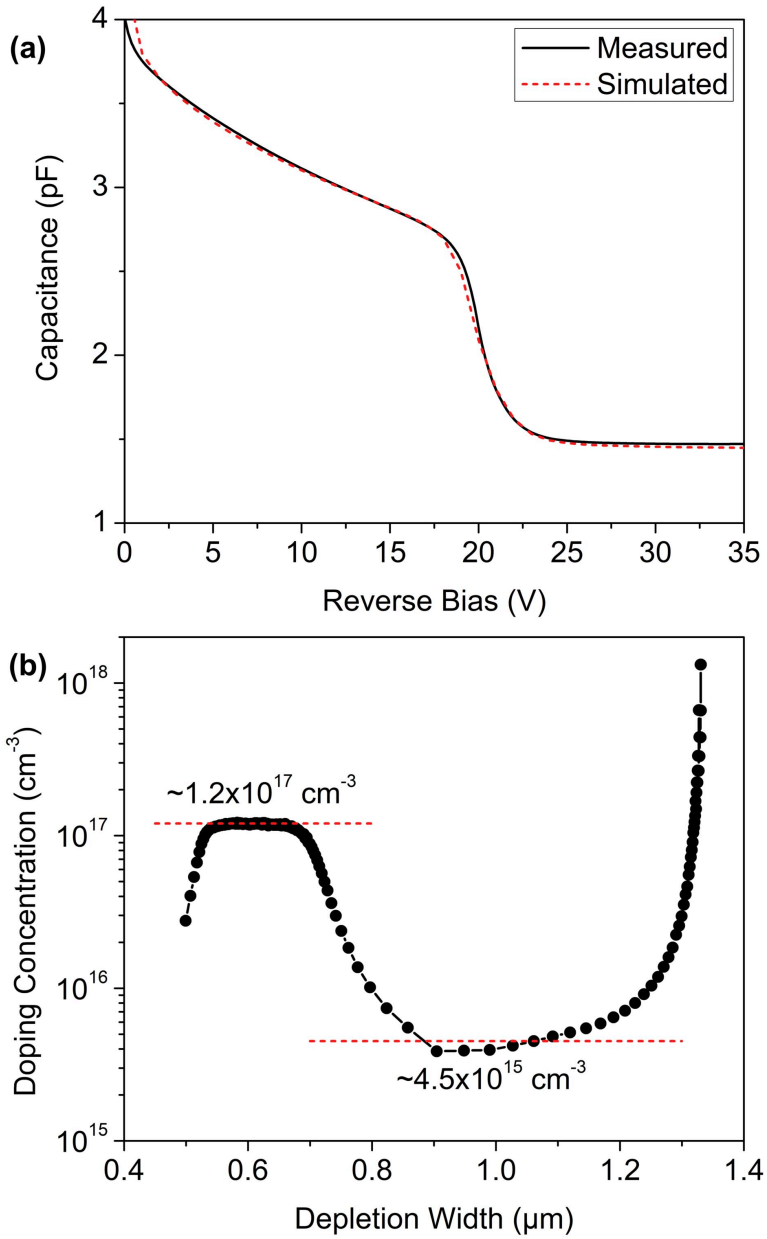

Figure 7.4: (a) The measured capacitance-voltage characteristic for a 150-µm diameter control device. Punch-through is visible around 20 V of reverse bias. The simulated capacitance-voltage characteristic is also included, and there is excellent agreement with the measurement. (b) The extracted doping concentration versus depletion width for the control structure with the p-charge region and absorber region doping values labeled.

One method to determine the gain is to use the following expression[74]

$$M = \frac{\left(\alpha(E) - \beta(E)\right)\exp\left[-W\left(\alpha(E) - \beta(E)\right)\right]}{\alpha(E) - \beta(E)\exp\left[W\left(\alpha(E) - \beta(E)\right)\right]} \tag{35}$$

where W is the thickness of the multiplier region and $\alpha(E)$ and $\beta(E)$ are the electric-field-dependent impact ionization coefficients for electrons and holes, respectively. Expressions for $\alpha(E)$ and $\beta(E)$ for $Al_{0.7}InAsSb$ have been previously published[46] and are as follows

$$\alpha(E) = 4.5 \times 10^6 \exp(-2.5 \times 10^6/E) \tag{36}$$

$$\beta(E) = 3.5 \times 10^6 \exp(-3.2 \times 10^6/E) \tag{37}$$

The control structure was simulated using Ansys Lumerical CHARGE to extract the electric field strength in the multiplication region. To confirm the accuracy of the simulation, the capacitance of the control structure was simulated and compared to the measurements. The capacitance for a 150-µm diameter device was measured with an HP 3275A LCR meter at 1 MHz under dark conditions. Figure 7.4(a) shows the measured and simulated capacitance-voltage characteristics for the control structure. There is excellent agreement between the measured and simulated C-V. Figure 7.4(b) shows the extracted doping concentration versus depletion width for the measured C-V in Figure 7.4(a). The measured p-charge and absorber doping concentrations are ~1.2×10^{17} cm^{-3} and ~4.5×10^{15} cm^{-3}, respectively. For the simulation, the absorber region was doped 5×10^{15} cm^{-3} p-type, the multiplier was doped 5×10^{15} cm^{-3} n-type, and the p-charge was doped 1.35×10^{17} cm^{-3} p-type. The slight difference between measured and simulated p-charge is likely due to a slight measurement uncertainty.

Now, with a sufficiently accurate simulation structure, the electric field in the structure can be obtained. From the simulation at a bias of -25 V, just after punch-through, the average electric field strength in the multiplication region is ~380 kV/cm^2. Substituting this electric field into (35), a gain of ~1.38 at -25 V is calculated in the control structure. Using this value, the gain of the control and cascaded multiplier APD can be calculated and is displayed in Figure 7.5. At a bias of -32 V, the cascaded multiplier APD has a gain of ~6.1, indicating a combined gain contribution from both the staircase step and conventional multiplier.

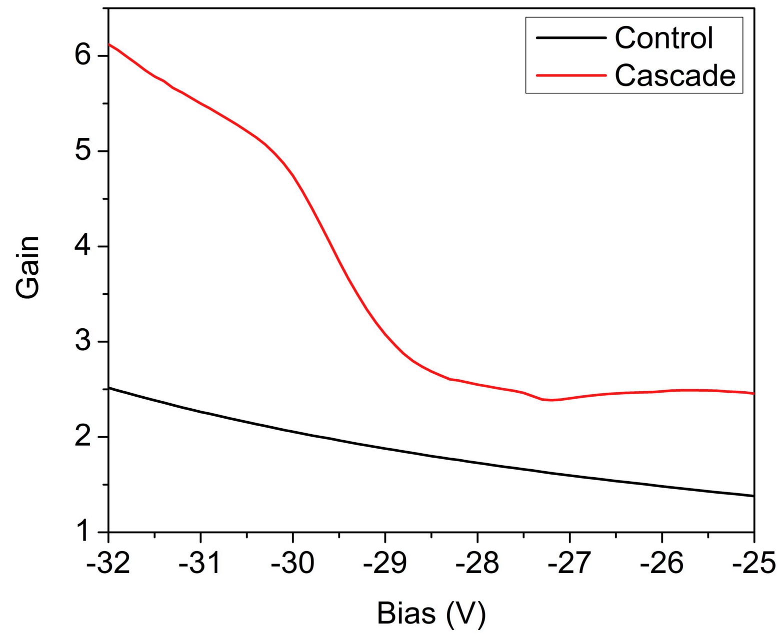

Figure 7.5: The calculated total gain of the cascaded multiplier APD and its control using the calculated gain of 1.38 at -25 V in the control.

Calculating the excess noise factor in the cascaded multiplier APD can be achieved in a similar way as other staircase-step-containing devices. The noise of the control structure can first be measured to calculate the unity-gain shot noise for calculating the excess noise of the cascaded multiplier APD. However, for the cascaded multiplier APD, the calculation is more complicated as the control structure no longer has unity gain and unity excess noise. The photocurrent contribution of the shot noise of both structures is as follows,

$$N_{\text{cascade}} = 2qI_{\text{photo}}R\Delta f M_{\text{cascade}}F(M)_{\text{cascade}} \tag{38}$$

$$N_{\text{control}} = 2qI_{\text{photo}}R\Delta f M_{\text{control}}F(M)_{\text{control}} \tag{39}$$

where both structures have their own M and $F(M)$ terms. Note that I_{photo} is the multiplied photocurrent, not the unity-gain photocurrent. Solving for $F(M)_{\text{cascade}}$ in (38) yields

$$F(M)_{\text{cascade}} = \frac{N_{\text{cascade}}}{2qI_{\text{photo}}R\Delta f M_{\text{cascade}}} \tag{40}$$

At -32 V (the bias where the cascaded multiplier APD is maximized), M_{cascade} is already known from Figure 7.5 above. The shot noise in the control structure represented in (39) can be used to calculate a value for $2qI_{\mathrm{photo}}R\Delta f$. The gain for the control structure at -32 V was determined above, so M_{control} is known. $F(M)_{\mathrm{control}}$ can be calculated from the local field model, (3). From previously published work, the k-factor of $Al_{0.7}InAsSb$ is ~0.01-0.05[28,29]. Measurements above in the APD Noise Considerations chapter also corroborate a k-factor of ~0.05. Using a k-factor of 0.05 and M_{control} = 2.54, the term $F(M)_{\mathrm{control}}$ is calculated to be 1.65.

With values for M_{control} and $F(M)_{\mathrm{control}}$, a measurement to obtain N_{control} is the final variable needed to calculate a value for $2qI_{\mathrm{photo}}R\Delta f$. With a bias of -32 V, the noise power of the control was measured as a function of photocurrent achieved by varying the output power of the laser. This measurement is the "Control Noise" line in Figure 7.6(a). A value for $2qI_{\mathrm{photo}}R\Delta f$ or "N_{unity}" can be obtained by dividing the control noise, (39), by the control gain, $M_{\mathrm{control}} = 2.54$, and the excess noise factor, $F(M)_{\mathrm{control}} = 1.65$, $N_{\mathrm{unity}} = N_{\mathrm{control}}/(M_{\mathrm{control}}F(M)_{\mathrm{control}})$. This new line is called "Unity Noise" in Figure 7.6(a). By using a measurement to obtain $2qI_{\mathrm{photo}}R\Delta f$, we can account for any uncertainties with system gain and bandwidth and any additional noise contributions from the laser source[44].

Now, with a line representing $2qI_{\mathrm{photo}}R\Delta f$, the excess noise factor of the cascaded multiplier APD can be calculated. Similar to the control, the cascaded multiplier APD was biased to -32 V, and the noise power was measured as a function of photocurrent by varying the output power of the laser. This line, "Cascade Noise," in Figure 7.6(a), is represented by (38). Finally, the excess noise factor of the cascade can be obtained with (40). The average excess noise factor of seven cascade devices at a unity photocurrent of ~1.5 µA is plotted in Figure 7.6(b). The average gain is 6.05, and the average excess noise factor is 1.28. This value is plotted alongside the excess noise factor scaling of a best-case k=0 conventional APD and a Si APD.

In order to account for measurement errors, because we assumed a k-factor of 0.05 for the control device, error bars have been added to the measurement. The error bars for gain are the minimum and maximum gain measured for the seven devices. The error bars for excess noise were generated by assuming a control k-factor of 0 for the minimum and a k-factor of 0.1 for the maximum.

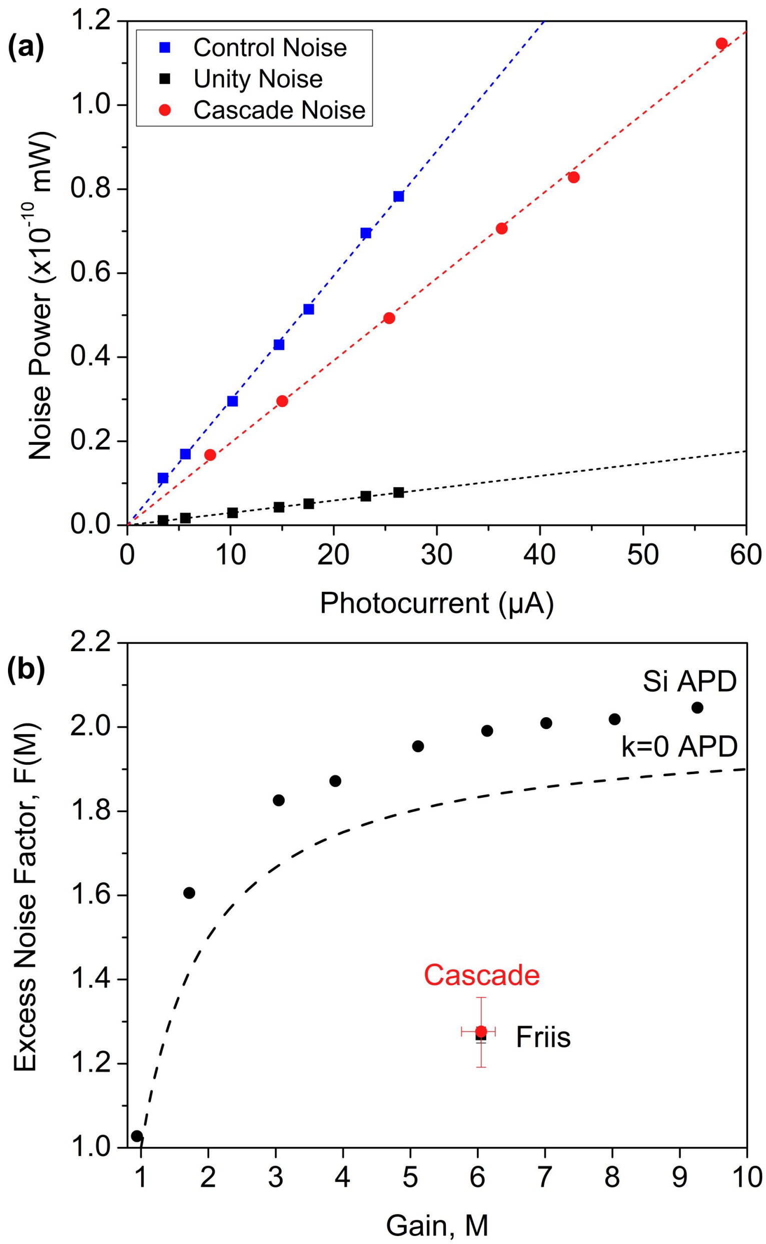

Figure 7.6: (a) The measured noise power versus photocurrent for the control and the cascaded multiplier APD, as well as the calculated unity gain noise. All measurements were made at -32 V under 543-nm He-Ne laser illumination. (b) The calculated excess noise factor of the cascaded multiplier APD. The point is an average of seven devices with error bars representing the span of measured gain and calculated excess noise. Also plotted is the theoretical excess noise factor calculated from Friis' equation, (41), and the excess noise factor scaling for a best-case k = 0 APD and a Si APD.

Using Friis' equation, the theoretical excess noise factor of the cascaded multiplier APD can be calculated. For the cascaded multiplier APD, Friis' noise equation is

$$F_{\text{cascade}} = F_1 + \frac{F_2 - 1}{M_1} = F_{1\text{ step}} + \frac{F_{\text{conventional}} - 1}{M_{1\text{ step}}} \tag{41}$$

where $F_{1\text{ step}}$ is the excess noise factor of a 1-step staircase APD, $F_{\text{conventional}}$ is the excess noise factor of the k = 0.05 conventional multiplier at a gain of 2.54, and $M_{1\text{ step}}$ is the gain of the 1-step staircase APD. For the cascaded multiplier APD, $F_{1\text{ step}}$ = 1, $F_{\text{conventional}}$ = 1.65, and $M_{1\text{ step}}$ = 2.42. Substituting these values into (41) yields a calculated excess noise factor of 1.27. An uncertainty can be placed on this value by varying the assumed k-value for the conventional multiplier from k = 0 to k = 0.1. With these two extremes, the calculated excess noise factor from Friis' equation is 1.27 ± 0.02. This value is also plotted in Figure 7.6(b).

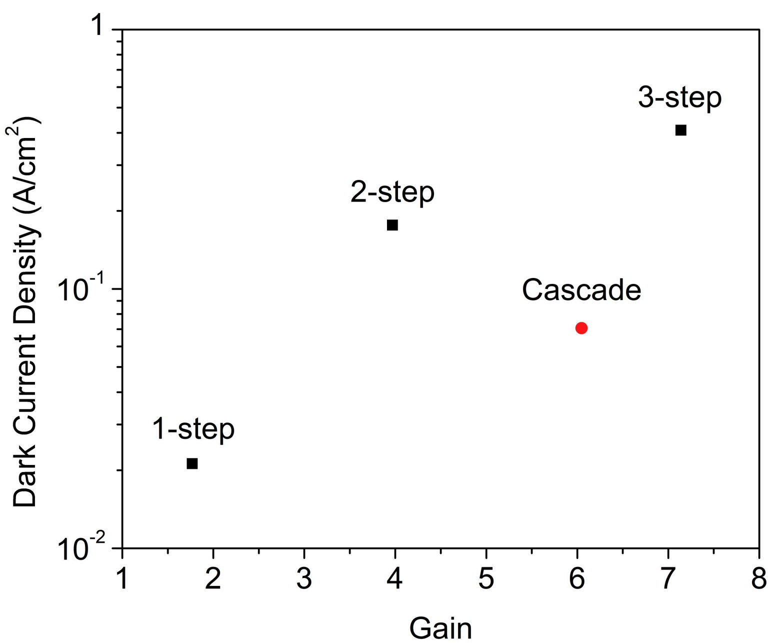

Figure 7.7: The Dark Current Density versus Gain for a 1-, 2-, and 3-step staircase APD plotted alongside the cascaded multiplier APD. Gain for all devices was determined with 543-nm He-Ne laser illumination.

For a final comparison, Figure 7.7 shows Dark Current Density versus Gain for the cascaded multiplier APD alongside those of 1-, 2-, and 3-step staircase APDs. From the plot, it is clear that the goals of the cascaded multiplier APD were achieved. The cascaded multiplier APD can achieve a gain greater than that of a 1-step staircase APD, 6.05 versus ~2. It can also achieve this gain with a dark current density of ~70 mA/cm^2 versus a dark current density of ~170 mA/cm^2 and ~400 mA/cm^2 for a 2-step and 3-step staircase APD, respectively. The trade-off for the cascaded multiplier APD is the slightly sacrificed excess noise factor of ~1.3 compared to the near unity excess noise factor in both the 2- and 3-step staircase APD structures.

In this chapter, I have demonstrated measurements of a cascaded multiplier APD structure incorporating a single staircase step followed by a conventional bulk $Al_{0.7}InAsSb$ multiplication region. The device reached a gain of ~6 with an excess noise factor of ~1.3. Compared to its pure staircase gain counterparts with similar gains (2- and 3-step staircase APDs), the cascaded multiplier APD achieved its gain with a dark current of ~70 mA/cm^2 compared to ~170 mA/cm^2 and ~400 mA/cm^2 for 2-step and 3-step staircase APDs, respectively. While this device only had a gain of ~6, there are two ways to increase the gain. Additional staircase steps can be added, each one doubling the gain. Also, optimizations in the design of the bulk multiplication region could be performed to increase its gain beyond the ~2.5 present in this design. Increasing the charge layer doping would allow a stronger electric field to build up in the $Al_{0.7}InAsSb$ multiplier, increasing its gain before the staircase step region depletes.

8 Final Comparison of $F(M)$

As a final comparison, Figure 8.1 shows the measured gain and excess noise factor for all devices presented in this dissertation, offering a convenient reference for the design space for AlInAsSb/GaSb. Traditional SACM APDs have the highest noise with k ~ 0.05 scaling; however, they offer the highest achievable gains much greater than 100. Staircase APDs with wide and narrow bandgap absorbers offer near-unity $F(M)$ with a gain approaching 8. The SACMcase brings the near-unity $F(M)$ of a staircase APD out to operating wavelengths in the MWIR. The cascaded multiplier offers a middle ground with respect to $F(M)$. With only a single staircase step, the cascade offers three times the gain of a 1-step staircase and only a 28% increase in $F(M)$. Additionally, the cascade has a dark current density ~4 times lower than regular 2- and 3-step staircase APDs with similar gains. Overall, the AlInAsSb/GaSb materials system offers a robust design space that can be tuned for specific needs. Conventional SACM APD structures are possible with high gain and low k-factor excess noise scaling for applications that demand high gain. Additionally, APDs incorporating staircase multiplication regions are possible for applications demanding the lowest possible excess noise.

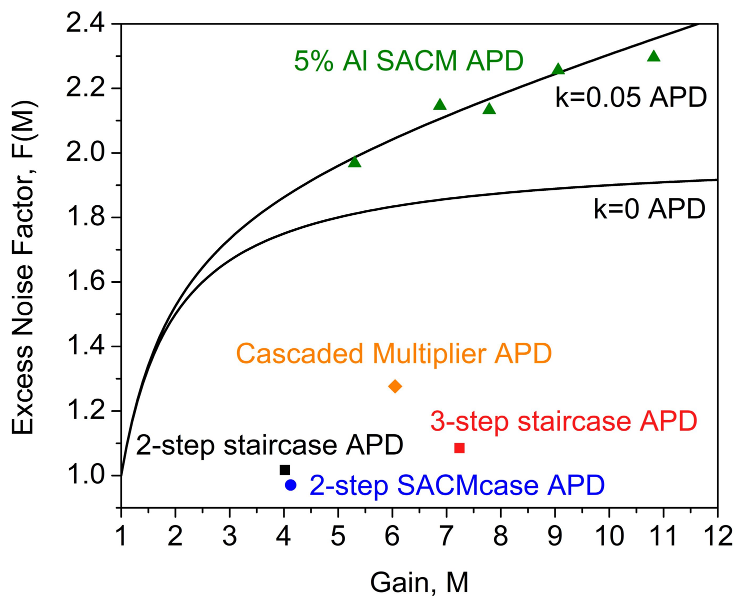

Figure 8.1: The excess noise factor versus gain for the $Al_{0.05}InAsSb$-based SACM APD, 2- and 3-step staircase APDs, 2-step SACMcase APD, and cascaded multiplier APD. Reference lines for k=0 and k=0.05 APDs are also included. It should be noted that even the highest excess noise reported here is on the order of the lowest excess noise for Si, known to have one of the lowest k-factors.

9 Future Work

9.1 Higher step-count Staircase APDs

A natural continuation for staircase APDs is to increase the number of steps. As the gain increases exponentially with the number of steps, the excess noise factor improvement over conventional APDs is also expected to increase exponentially. Figure 9.1 shows the projected excess noise factor versus gain for higher step count staircase APDs plotted alongside existing InGaAs/InP[42] and InGaAs/InAlAs[75] SACM APDs. Excess noise measurements for existing 2- and 3-step staircase APDs are included, as well as vertical lines at gains of 16 and 32 for a theoretical 4- and 5-step staircase, respectively. A 4-step staircase APD with a gain of 16 would have ~5x and ~9x lower excess noise than InGaAs/InP and InGaAs/InAlAs SACM APDs. A 5-step staircase APD with a gain of 32 would have ~8x and ~17x lower excess noise than InGaAs/InP and InGaAs/InAlAs SACM APDs. The higher step-count devices would also need to be realized as SACMcase structures to allow for infrared absorption like the existing SACM structures.

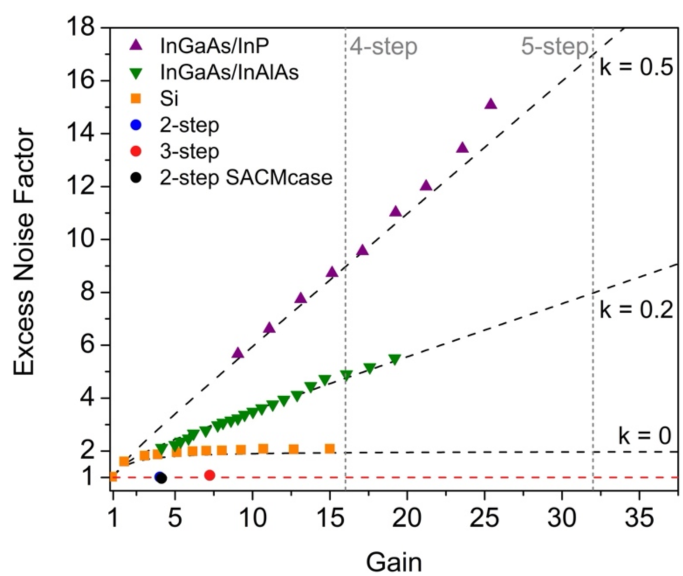

Figure 9.1: The projected excess noise factor versus gain for a staircase APD (red dashed) compared to InGaAs/InP SACM APDs[42], InGaAs/InAlAs SACM APDs[75]. Excess noise measurements for existing 2- and 3-step staircase APDs are included, as well as vertical lines at gains of 16 and 32 for a theoretical 4- and 5-step staircase, respectively.

The main limitation in realizing higher step count staircase APDs is ensuring that all the staircase steps unfold simultaneously. With each additional staircase step added, it becomes more challenging to balance the electrostatics of the device in a way to ensure all steps unfold together. If only some of the steps are unfolded, there could be significant charge trapping in the unfolded steps as they essentially act as an energy well. Additionally, suppose one step has completely unfolded and begins to flatten before the others. In that case, carriers may begin tunneling in the narrow bandgap region at the bottom of the step, resulting in increased dark currents. Adding intermediate charge layers between steps may become necessary for higher step counts to ensure the proper step unfolding.

9.2 $Al_{0.7}$InAsSb/InP SACM APDs

While my research has focused entirely on AlInAsSb lattice matched to GaSb, it is also possible to grow AlInAsSb lattice matched to InP. Two papers have been recently published about $Al_{0.70}In_{0.30}As_{0.82}Sb_{0.18}$ PIN APDs lattice matched to InP[39,40]. Similar to its GaSb counterpart, AlInAsSb on InP was also found to have a low k-factor of ~0.02. Growth of AlInAsSb on InP presents fewer difficulties than growth on GaSb as it can be grown as a random alloy. Theoretically, the direct band gap tunability for AlInAsSb/InP should range from 1.81 eV ($Al_{0.84}In_{0.16}As_{0.70}Sb_{0.30}$) to 1.45 eV ($Al_{0.48}In_{0.52}As$)[76]. However, for $Al_{0.70}In_{0.30}As_{0.82}Sb_{0.18}$, Hirst et al. have experimentally measured the bandgap to be closer to 1.45 eV when grown at 325°C instead of the theoretically predicted 1.57 eV[76]. For $Al_{0.79}In_{0.21}As_{0.74}Sb_{0.26}$, Kodati et al. have reported a bandgap of ~1.55 eV when grown at 450°C instead of the theoretically predicted 1.77 eV[39].

In addition to the growth of AlInAsSb as a random alloy, there are several other significant benefits of being latticed to InP. First, crystal growth on InP is a more mature process compared to growth on GaSb, leading to easier and cheaper growth at foundries. Second, a lattice match to InP unlocks the potential to use $In_{0.53}$GaAs as an absorbing material for SACM designs. As $In_{0.53}$GaAs/InP is a staple for telecommunications at 1550 nm, its material properties are well known, making it easier to design devices with predictable characteristics. Finally, the availability of semi-insulating InP substrates allows for higher bandwidth devices compared to ones grown on highly-doped GaSb substrates[35].

With these considerations in mind, I have designed an SACM APD incorporating a $Al_{0.7}$InAsSb multiplier and $In_{0.53}$GaAs absorber designed for operation at 1550 nm. The schematic cross-section of the device is shown in Figure 9.2. A 1000-nm thick multiplier was chosen to match the thickness in previously reported $Al_{0.7}InAsSb$ PIN APDs[40]. A 1500-nm thick absorber should give an EQE of ~40 % without incorporating an AR coating. Implementing a 1%-reflectively AR coating would increase the EQE up to ~57 %. The EQE for the device was estimated using the following,

$$\eta_{\mathrm{ext}} = (1 - R_{\mathrm{InGaAs}}) \exp\left(-\alpha_{\mathrm{InGaAs}} W_{\mathrm{InGaAs,contact}}\right)\left(1 - \exp(-\alpha_{\mathrm{InGaAs}} W_{\mathrm{InGaAs}})\right) \quad (42)$$

where R_{InGaAs} = 0.31 is the surface reflection for $In_{0.53}GaAs$[77] at 1550 nm, α_{InGaAs} = 6200 cm^{-1} is the absorption coefficient for $In_{0.53}GaAs$[77] at 1550 nm, $W_{\mathrm{InGaAs,contact}}$ = 100 nm is the thickness of $In_{0.53}GaAs$ in the contact region, and W_{InGaAs} = 1500 nm is the thickness of the absorber. In (42), $(1 - R_{\mathrm{InGaAs}})$ represents light lost due to surface reflections, $\exp\left(-\alpha_{\mathrm{InGaAs}} W_{\mathrm{InGaAs,contact}}\right)$ represents light lost due to absorption in the contact region, and $1 - \exp(-\alpha_{\mathrm{InGaAs}} W_{\mathrm{InGaAs}})$ represents light absorbed and collected in the absorber. Finally, $In_{0.53}GaAs$ was used for both p- and n-contacts as low resistance ohmic contacts can be formed[78].

Simulations for this device using ANSYS Lumerical CHARGE indicate an operating range of ~38 V with breakdown in the multiplier[40] (600 kV/cm) occurring at -85 V. At the time of writing, we are currently discussing the growth of this structure with a commercial foundry.

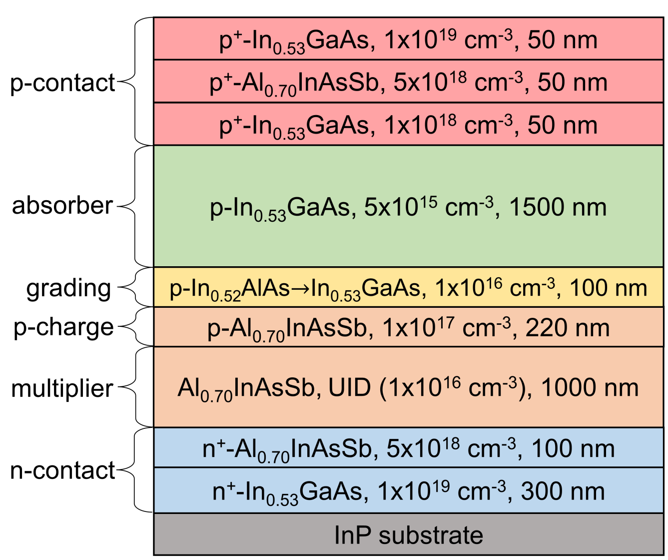

Figure 9.2: The schematic cross-section of a $Al_{0.7}InAsSb$-based SACM APD lattice matched to InP.

Publications

Journals

Herrera, D. J., **Dadey, A. A.**, March S. D., Bank, S. R., Campbell, J. C., AlInAsSb Geiger-mode SWIR and eSWIR SPADs with High Avalanche Probability. *OE*, submitted.

Dadey, A. A., Jones, A. H., March, S. D., Bank, S. R., Campbell, J. C., Separate absorption, charge, and multiplication staircase avalanche photodiodes. *Applied Physics Letters*, submitted.

Wei, D., **Dadey, A. A.**, McArthur, J. A., Bank S. R., Campbell, J. C., Enhancing Extended SWIR $Al_{0.3}InAsSb$ PIN Photodetectors with All-Dielectric Amorphous Germanium Photon-Capturing Gratings. *ACS Photonics*, in review.

Dadey, A. A., Jones, A. H., March, S. D., Bank, S. R., Campbell, J. C., Near-unity excess noise factor of staircase avalanche photodiodes. *Optica, OPTICA* **10** 1353–1357 (2023).

McArthur, J. A., **Dadey, A. A.**, March, S. D., Jones, A. H., Xue, X., Salas, R., Campbell, J. C., Bank, S. R., Demonstration of the AlInAsSb cascaded multiplier avalanche photodiode. *Applied Physics Letters* **123**, 041106 (2023).

Dadey, A. A., McArthur, J. A., Jones, A. H., Bank, S. R., Campbell, J. C., Considerations for excess noise measurements in low-k-factor Sb-based avalanche photodiodes. *J. Opt. Soc. Am. A, JOSAA* **40**, 1225-1230 (2023).

Chen, D., March, S. D., Jones, A. H., Shen, Y., **Dadey, A. A.**, Sun K., McArthur, J. A., Skipper, A. M., Xue, X., Guo, B., Bai, J., Bank, S. R., Campbell, J. C., Photon-trapping-enhanced avalanche photodiodes for mid-infrared applications. *Nat. Photon.* **17**, 594-600 (2023).

Dadey, A. A., McArthur, J. A., Kamboj, A., Bank, S. R., Wasserman, D., Campbell, J. C., High-gain low-excess-noise MWIR detection with a 3.5-µm cutoff AlInAsSb-based separate absorption, charge, and multiplication avalanche photodiode. *APL Photonics* **8**, 036101 (2023).

Dadey, A. A., Jones, A. H., McArthur, J. A., Wang, E. Y., Muhowski, A. J., Bank, S. R., Campbell, J. C., Narrow bandgap $Al_{0.15}In_{0.85}As_{0.77}Sb_{0.23}$ for mid-infrared photodetectors. *Opt. Express, OE* **30**, 27285–27292 (2022).

Chen, D., Sun, K., Shen, Y., Jones, A. H., **Dadey, A. A.**, Guo, B., McArthur, J. A., Bank, S. R., Campbell, J. C., Frequency behavior of AlInAsSb nBn photodetectors and the development of an equivalent circuit model. *Opt. Express, OE* **30**, 25262–25276 (2022).

Jones, A. H., March, S. D., **Dadey, A. A.**, Muhowski A. J., Bank, S. R., Campbell, J. C., AlInAsSb Separate Absorption, Charge, and Multiplication Avalanche Photodiodes for Mid-Infrared Detection. *IEEE Journal of Quantum Electronics* **58**, 1-6 (2022).

Chen, D. McArthur, J. A., March, S. D., Xue, X., Jones, A. H., **Dadey, A. A.**, Bank, S. R., Campbell, J. C., Comparison and analysis of Al0.7InAsSb avalanche photodiodes with different background doping polarities. *Appl. Phys. Lett.* **119**, 032101 (2021).

Conferences

Dadey, A. A., Jones, A. H., March, S. D., Bank, S. R., Campbell, J. C., Staircase Avalanche Photodiode with a Mid-wave Infrared Absorber. in *2023 IEEE Photonics Conference (IPC)* 1-2 (2023).

Dadey, A. A., McArthur, J. A., Bank, S. R., Campbell, J. C., Separate Absorption, Charge, and Multiplication Avalanche Photodiode with a Digital Alloy $Al_{0.05}In_{0.95}As_{0.93}Sb_{0.07}$ Absorber for Mid-IR Detection. in *2022 IEEE Photonics Conference (IPC)* 1-2 (2022).

Dadey, A. A., March, S. D., Xue, X., Bank, S. R. & Campbell, J. C., Cryogenic Noise of Staircase Avalanche Photodiodes. in *2021 IEEE Photonics Conference (IPC)* 1–2 (2021).

El-Jaroudi, R. H., **Dadey, A. A.**, Xue, X., Jones, A. H., Guo, B., Campbell, J. C., Bank, S. R., Reducing III-V avalanche photodiode noise through the introduction of boron. *Device Research Conference* (2021).

References

1. Campbell, J. C. Recent Advances in Avalanche Photodiodes. *J. Lightwave Technol., JLT* **34**, 278–285 (2016).
2. Eastman, J. Brief history of barcode scanning. in *OSA Century of Optics* 128–133 (Optical Society, 2015).
3. Forrest, S. R. Chapter 4 Sensitivity of Avalanche Photodetector Receivers for High-Bit-Rate Long-Wavelength Optical Communication Systems. in *Semiconductors and Semimetals* (ed. Tsang, W. T.) vol. 22 329–387 (Elsevier, 1985).
4. Campbell, J. C. Recent Advances in Telecommunications Avalanche Photodiodes. *Journal of Lightwave Technology* **25**, 109–121 (2007).
5. Sun, X., Abshire, J. B. & Beck, J. D. HgCdTe e-APD detector arrays with single photon sensitivity for space lidar applications. in *Advanced Photon Counting Techniques VIII* vol. 9114 80–89 (SPIE, 2014).
6. Li, N. *et al.* A Progress Review on Solid-State LiDAR and Nanophotonics-Based LiDAR Sensors. *Laser & Photonics Reviews* **16**, 2100511 (2022).
7. Wier, W. G., Balke, C. W., Michael, J. A. & Mauban, J. R. H. A custom confocal and two-photon digital laser scanning microscope. *American Journal of Physiology-Heart and Circulatory Physiology* **278**, H2150–H2156 (2000).
8. Donati, S. & Tambosso, T. Single-Photon Detectors: From Traditional PMT to Solid-State SPAD-Based Technology. *IEEE Journal of Selected Topics in Quantum Electronics* **20**, 204–211 (2014).
9. Ghioni, M., Gulinatti, A., Rech, I., Zappa, F. & Cova, S. Progress in Silicon Single-Photon Avalanche Diodes. *IEEE Journal of Selected Topics in Quantum Electronics* **13**, 852–862 (2007).
10. Hadfield, R. H. Single-photon detectors for optical quantum information applications. *Nature Photon* **3**, 696–705 (2009).
11. Signorelli, F. *et al.* Low-Noise InGaAs/InP Single-Photon Avalanche Diodes for Fiber-Based and Free-Space Applications. *IEEE Journal of Selected Topics in Quantum Electronics* **28**, 1–10 (2022).
12. Liu, C., Ye, H.-F. & Shi, Y.-L. Advances in near-infrared avalanche diode single-photon detectors. *Chip* **1**, 100005 (2022).
13. Canon developing world-first ultra-high-sensitivity ILC equipped with SPAD sensor, supporting precise monitoring through clear color image capture of subjects several km away, even in darkness. *Canon Global* https://global.canon/en/news/2023/20230403.html.
14. Kyba, C. C. M., Mohar, A. & Posch, T. How bright is moonlight? *Astronomy & Geophysics* **58**, 1.31-1.32 (2017).
15. Bagnasco, G. *et al.* Overview of the near-infrared spectrograph (NIRSpec) instrument on-board the James Webb Space Telescope (JWST). in *Cryogenic Optical Systems and Instruments XII* vol. 6692 174–187 (SPIE, 2007).
16. Rieke, G. H. *et al.* The Mid-Infrared Instrument for the$\less$i$\greater$James Webb Space Telescope$\less$/i$\greater$, VII: The MIRI Detectors. *PASP* **127**, 665–674 (2015).
17. Popa, D. & Udrea, F. Towards Integrated Mid-Infrared Gas Sensors. *Sensors* **19**, 2076 (2019).
18. Razeghi, M. & Nguyen, B.-M. Advances in mid-infrared detection and imaging: a key issues review. *Rep. Prog. Phys.* **77**, 082401 (2014).
19. McIntyre, R. J. Multiplication noise in uniform avalanche diodes. *IEEE Transactions on Electron Devices* **ED-13**, 164–168 (1966).
20. Capasso, F., Tsang, W.-T. & Williams, G. F. Staircase solid-state photomultipliers and avalanche photodiodes with enhanced ionization rates ratio. *IEEE Transactions on Electron Devices* **30**, 381–390 (1983).
21. Teich, M., Matsuo, K. & Saleh, B. Excess noise factors for conventional and superlattice avalanche photodiodes and photomultiplier tubes. *IEEE Journal of Quantum Electronics* **22**, 1184–1193 (1986).
22. Frisk, C. *et al.* On the Extraction of Doping Concentration From Capacitance–Voltage: A Cu2ZnSnS4 and ZnS Sandwich Structure. *IEEE Journal of Photovoltaics* **7**, 1421–1425 (2017).

23. Zheng, X. G. *et al.* Long-wavelength In/sub 0.53/Ga/sub 0.47/As-In/sub 0.52/Al/sub 0.48/As large-area avalanche photodiodes and arrays. *IEEE Journal of Quantum Electronics* **40**, 1068–1073 (2004).
24. Ker, P. J., Marshall, A. R. J., Krysa, A. B., David, J. P. R. & Tan, C. H. Temperature Dependence of Leakage Current in InAs Avalanche Photodiodes. *IEEE Journal of Quantum Electronics* **47**, 1123–1128 (2011).
25. Liu, H.-D. *et al.* Avalanche photodiode punch-through gain determination through excess noise analysis. *Journal of Applied Physics* **106**, 064507 (2009).
26. Onabe, K. Unstable Regions in III–V Quaternary Solid Solutions Composition Plane Calculated with Strictly Regular Solution Approximation. *Jpn. J. Appl. Phys.* **21**, L323 (1982).
27. Maddox, S. J., March, S. D. & Bank, S. R. Broadly Tunable AlInAsSb Digital Alloys Grown on GaSb. *Crystal Growth & Design* **16**, 3582–3586 (2016).
28. Bank, S. R. *et al.* Avalanche Photodiodes Based on the AlInAsSb Materials System. *IEEE Journal of Selected Topics in Quantum Electronics* **24**, 1–7 (2018).
29. Woodson, M. E. *et al.* Low-noise AlInAsSb avalanche photodiode. *Appl. Phys. Lett.* **108**, 081102 (2016).
30. Ren, M. *et al.* Characteristics of $Al_xIn_{1-x}As_ySb_{1-y}$ (x:0.3−0.7) Avalanche Photodiodes. *Journal of Lightwave Technology* **35**, 2380–2384 (2017).
31. Jones, A. H. *et al.* High Gain, Low Dark Current Al0.8In0.2As0.23Sb0.77 Avalanche Photodiodes. *IEEE Photonics Technology Letters* **31**, 1948–1951 (2019).
32. Campbell, J. C., David, J. P. R. & Bank, S. R. Sb-Based Low-Noise Avalanche Photodiodes. *Photonics* **10**, 715 (2023).
33. Ren, M. *et al.* AlInAsSb separate absorption, charge, and multiplication avalanche photodiodes. *Appl. Phys. Lett.* **108**, 191108 (2016).
34. Jones, A. H., March, S. D., Bank, S. R. & Campbell, J. C. Low-noise high-temperature AlInAsSb/GaSb avalanche photodiodes for 2-μm applications. *Nat. Photonics* **14**, 559–563 (2020).
35. Chen, D. *et al.* Photon-trapping-enhanced avalanche photodiodes for mid-infrared applications. *Nat. Photon.* **17**, 594–600 (2023).
36. Zheng, J. *et al.* Characterization of band offsets in AlxIn1-xAsySb1-y alloys with varying Al composition. *Appl. Phys. Lett.* **115**, 122105 (2019).
37. Vegard, L. Die Konstitution der Mischkristalle und die Raumfüllung der Atome. *Z. Physik* **5**, 17–26 (1921).
38. Guden, M. & Piprek, J. Material parameters of quaternary III - V semiconductors for multilayer mirrors at wavelength. *Modelling Simul. Mater. Sci. Eng.* **4**, 349 (1996).
39. Kodati, S. H. *et al.* AlInAsSb avalanche photodiodes on InP substrates. *Appl. Phys. Lett.* **118**, 091101 (2021).
40. Ronningen, T. J. *et al.* Ionization coefficients and excess noise characteristics of AlInAsSb on an InP substrate. *Applied Physics Letters* **123**, 131110 (2023).
41. Jin, X. *et al.* Excess noise measurements in Al0.85Ga0.15As0.56Sb0.44 avalanche photodiodes. in *Optical Sensing and Detection VII* vol. 12139 59–66 (SPIE, 2022).
42. Lee, S. *et al.* High gain, low noise 1550 nm GaAsSb/AlGaAsSb avalanche photodiodes. *Optica, OPTICA* **10**, 147–154 (2023).
43. David, J. P. R. *et al.* Avalanche multiplication and excess noise characteristics in antimony-based avalanche photodiodes. in *Emerging Imaging and Sensing Technologies for Security and Defence VII* vol. 12274 54–65 (SPIE, 2022).
44. Bulman, G. E., Robbins, V. M. & Stillman, G. E. The determination of impact ionization coefficients in (100) gallium arsenide using avalanche noise and photocurrent multiplication measurements. *IEEE Transactions on Electron Devices* **32**, 2454–2466 (1985).
45. Green, J. E., David, J. P. R. & Tozer, R. C. A transimpedance amplifier for excess noise measurements of high junction capacitance avalanche photodiodes. *Meas. Sci. Technol.* **23**, 125901 (2012).
46. Yuan, Y. *et al.* AlInAsSb Impact Ionization Coefficients. *IEEE Photonics Technology Letters* **31**, 315–318 (2019).

47. Aspnes, D. E. & Studna, A. A. Dielectric functions and optical parameters of Si, Ge, GaP, GaAs, GaSb, InP, InAs, and InSb from 1.5 to 6.0 eV. *Phys. Rev. B* **27**, 985–1009 (1983).
48. Campbell, J. C. Evolution of Low-Noise Avalanche Photodetectors. *IEEE Journal of Selected Topics in Quantum Electronics* **28**, 1–11 (2022).
49. Taylor-Mew, J., Shulyak, V., White, B., Tan, C. H. & Ng, J. S. Low Excess Noise of Al0.85Ga0.15As0.56Sb0.44 Avalanche Photodiode From Pure Electron Injection. *IEEE Photonics Technology Letters* **33**, 1155–1158 (2021).
50. Woods, M. H., Johnson, W. C. & Lampert, M. A. Use of a Schottky barrier to measure impact ionization coefficients in semiconductors. *Solid-State Electronics* **16**, 381–394 (1973).
51. Huang, J. *et al.* High-performance mid-wavelength InAs avalanche photodiode using $AlAs_{0.13}Sb_{0.87}$ as the multiplication layer. *Photon. Res., PRJ* **8**, 755–759 (2020).
52. Verschraegen, J., Burgelman, M. & Penndorf, J. Temperature dependence of the diode ideality factor in CuInS2-on-Cu-tape solar cells. *Thin Solid Films* **480–481**, 307–311 (2005).
53. Hudait, M. K. & Krupanidhi, S. B. Doping dependence of the barrier height and ideality factor of Au/n-GaAs Schottky diodes at low temperatures. *Physica B: Condensed Matter* **307**, 125–137 (2001).
54. Jones, A. H. *et al.* AlInAsSb Separate Absorption, Charge, and Multiplication Avalanche Photodiodes for Mid-Infrared Detection. *IEEE Journal of Quantum Electronics* **58**, 1–6 (2022).
55. Dadey, A. A. *et al.* Narrow bandgap $Al_{0.15}In_{0.85}As_{0.77}Sb_{0.23}$ for mid-infrared photodetectors. *Opt. Express, OE* **30**, 27285–27292 (2022).
56. White, B. S. *et al.* High-Gain InAs Planar Avalanche Photodiodes. *J. Lightwave Technol.* **34**, 2639–2644 (2016).
57. Kaneda, T., Matsumoto, H., Sakurai, T. & Yamaoka, T. Excess noise in silicon avalanche photodiodes. *Journal of Applied Physics* **47**, 1605–1607 (1976).
58. Kanbe, H., Kimura, T., Mizushima, Y. & Kajiyama, K. Silicon avalanche photodiodes with low multiplication noise and high-speed response. *IEEE Transactions on Electron Devices* **23**, 1337–1343 (1976).
59. Ferrini, R., Patrini, M. & Franchi, S. Optical functions from 0.02 to 6 eV of AlxGa1−xSb/GaSb epitaxial layers. *Journal of Applied Physics* **84**, 4517–4524 (1998).
60. Rothman, J. *et al.* High performance characteristics in pin MW HgCdTe e-APDs. in *Infrared Technology and Applications XXXIII* vol. 6542 475–484 (SPIE, 2007).
61. Williams, G. F., Capasso, F. & Tsang, W. T. The graded bandgap multilayer avalanche photodiode: A new low-noise detector. *IEEE Electron Device Letters* **3**, 71–73 (1982).
62. Matsuo, K., Teich, M. & Saleh, B. Noise properties and time response of the staircase avalanche photodiode. *Journal of Lightwave Technology* **3**, 1223–1231 (1985).
63. Pilotto, A. *et al.* A New Expression for the Gain-Noise Relation of Single-Carrier Avalanche Photodiodes With Arbitrary Staircase Multiplication Regions. *IEEE Transactions on Electron Devices* **66**, 1810–1814 (2019).
64. Van Vliet, K. M. & Rucker, L. M. Noise associated with reduction, multiplication and branching processes. *Physica A: Statistical Mechanics and its Applications* **95**, 117–140 (1979).
65. Ripamonti, G. *et al.* Realization of a staircase photodiode: Towards a solid-state photomultiplier. *Nuclear Instruments and Methods in Physics Research Section A: Accelerators, Spectrometers, Detectors and Associated Equipment* **288**, 99–103 (1990).
66. Czajkowski, I. K., Allam, J. & Adams, A. R. Role of satellite valleys in ionisation rate enhancement in multiple quantum well avalanche photodiodes. *Electronics Letters* **16**, 1311–1313 (1990).
67. Ren, M. *et al.* AlInAsSb/GaSb staircase avalanche photodiode. *Appl. Phys. Lett.* **108**, 081101 (2016).
68. March, S. D., Jones, A. H., Campbell, J. C. & Bank, S. R. Multistep staircase avalanche photodiodes with extremely low noise and deterministic amplification. *Nature Photonics* 1–7 (2021) doi:10.1038/s41566-021-00814-x.
69. Ren, M. *et al.* AlInAsSb/GaSb staircase avalanche photodiode. *Appl. Phys. Lett.* **108**, 081101 (2016).
70. March, S. D., Jones, A. H., Campbell, J. C. & Bank, S. R. Multistep staircase avalanche photodiodes with extremely low noise and deterministic amplification. *Nat. Photonics* **15**, 468–474 (2021).

71. Cardona, M. Optical investigation of the band structure of GaSb. *Z. Physik* **161**, 99–102 (1961).
72. Williams, G. F., Capasso, F. & Tsang, W. T. The graded bandgap multilayer avalanche photodiode: A new low-noise detector. *IEEE Electron Device Lett.* **3**, 71–73 (1982).
73. Friis, H. T. Noise Figures of Radio Receivers. *Proceedings of the IRE* **32**, 419–422 (1944).
74. Capasso, F. Chapter 1 Physics of Avalanche Photodiodes. in *Semiconductors and Semimetals* (ed. Tsang, W. T.) vol. 22 1–172 (Elsevier, 1985).
75. Xie, S., Zhang, S. & Tan, C. H. InGaAs/InAlAs Avalanche Photodiode With Low Dark Current for High-Speed Operation. *IEEE Photonics Technology Letters* **27**, 1745–1748 (2015).
76. Hirst, L. C. *et al.* Spatially indirect radiative recombination in InAlAsSb grown lattice-matched to InP by molecular beam epitaxy. *Journal of Applied Physics* **117**, 215704 (2015).
77. Adachi, S. Optical dispersion relations for GaP, GaAs, GaSb, InP, InAs, InSb, AlxGa1−xAs, and In1−xGaxAsyP1−y. *Journal of Applied Physics* **66**, 6030–6040 (1989).
78. Crook, A. M. *et al.* Low resistance, nonalloyed Ohmic contacts to InGaAs. *Applied Physics Letters* **91**, 192114 (2007).

Appendix 1: Device Fabrication

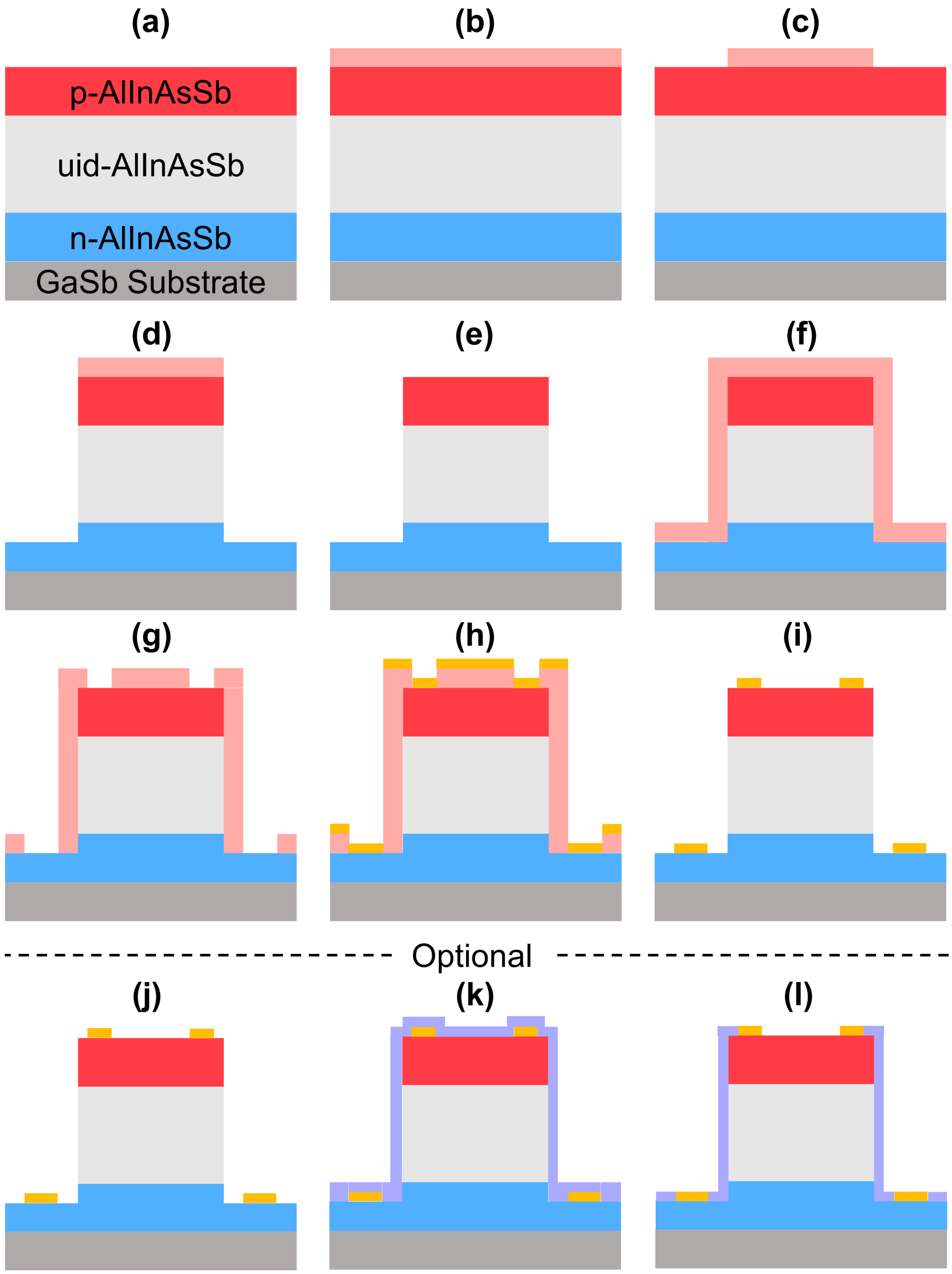

Figure A1.1: Fabrication process for a PIN avalanche photodiode.

A1.1 Fabrication Steps

1. The basic structure of an AlInAsSb-based PIN APD is shown in Figure A1.1(a).
2. On a spinner, rinse the surface of the sample with Acetone and Isopropanol (~10 s each) to remove any residue from the surface. Dry the surface with nitrogen.
3. Using a photoresist spinner, coat the surface in a layer of positive resist. After spinning the resist, bake on a hot plate. After this step, the sample will look as depicted in Figure A1.1(b). In our group, we typically use AZ 5214 with the following parameters.
   3.1. Spin speed: 4000 rpm
   3.2. Acceleration: 1000 rpm/s
   3.3. Spin time: 40 s
   3.4. Bake temperature: 100 C
   3.5. Bake time: 60 s
4. Using a Mask Aligner, align the pattern for the mesa structure (typically circles of various sizes). When the pattern is aligned, expose the sample. After exposure, develop the sample. When finished, the sample will look like Figure A1.1(c). For exposure, we used 365-nm light, and for development, we use AZ 300 MIF with the following parameters.
   4.1. Exposure dose: 175 mJ/cm^2
   4.2. Develop time: ~45 s (or until the mesa pattern is clearly visible)
5. To form the mesas, wet etch the sample in a solution of $C_6H_8O_7$:H_3PO_4:H_2O_2:H_2O (10 g: 6 mL: 3 mL: 60 mL). Etch until the n-contact (blue) layer is reached, as shown in Figure A1.1(d). Remove the remaining photoresist with an Acetone/Isopropanol rinse (10 s each) and dry with nitrogen. (Figure A1.1(e)) Etching can also be performed in a dry/wet process, as detailed below.
6. Like step 3, spin another layer of positive photoresist (Figure A1.1(f)).
7. Use a Mask Aligner to align and expose the pattern for the metal contact layer (Figure A1.1(g)). We use the same metals for both the p- and n-contacts.
8. Use an E-beam Evaporator to deposit the contact metals. Typically, we use a layer of Ti/Au (10 nm/100 nm) (Figure A1.1(h)).
9. Use Acetone and an ultrasonic bath to remove the unwanted contact metal by dissolving the underlying photoresist and lifting off the metal (Figure A1.1(i)). At this point, the devices have been fully formed and can be tested.

A1.2 Optional Passivation

10. A layer of SU-8 photoresist can be spun onto the sample to protect the device sidewalls from oxidation that would adversely affect the performance of the photodiodes by increasing their surface leakage current. To do so, take the finished sample (Figure A1.1(j)) and spin on a layer of SU-8 photoresist (Figure A1.1(k)). Our group typically uses SU-8 2000.5 with the following parameters.
    10.1. Spin speed: 5000 rpm
    10.2. Acceleration: 500 rpm/s
    10.3. Spin time: 40 s
    10.4. Bake temperature: 90 C
    10.5. Bake time: 70 s
11. Use a Mask Aligner to align the passivation pattern and expose the sample. Bake the sample a second time and develop. The finished sample will look as depicted in Figure A1.1(l). For exposure, we used 365-nm light, and for development, we use SU-8 Developer with the following parameters.
    11.1. Exposure dose: 500 mJ/cm^2
    11.2. Post-exposure bake temperature: 90 C

11.3. Post-exposure bake time: 70 s
11.4. Develop time: 30 s

A1.3 Dry/wet Etch Option

For the wet etchant described in step 5, the etch rate greatly decreases as the concentration of Al in AlInAsSb decreases. For the low Al%-containing compositions needed for MWIR detection, a pure wet etch leads to a large enough bevel such that the metal contact lithography no longer fits on the top mesa. This problem can be circumvented by performing a dry etch to partially form the mesas, followed by a wet etch to remove sidewall damage caused by the dry etch. Due to its physical nature, a dry etch will vertically etch a mesa with minimal beveling. Typically, the dry etch is used to etch through the low Al-containing AlInAsSb layers. A wet etch, using the solution in step 5, is used to finish the etch in the high Al-containing AlInAsSb layers. Below are the parameters for dry etching using a reactive ion etch with inductively coupled plasma (RIE-ICP). A thicker photoresist must also be used as the dry etch we use is not selective to photoresist. We typically use AZ4330 with parameters also listed below.

RIE-ICP Parameters:

- Process gases: Cl_2/N_2 (8 sccm/ 20 sccm)
- Process pressure: 4 mTorr.
- Process temperature: 50 C
- RF Power: 115 W
- ICP Power: 300 W

AZ4330 Parameters:

- Spin: 2500 rpm, 1000 rpm/s, 30 s
- Bake: 110 C for 120 s
- Exposure Dose: 500 mJ/cm^2
- Develop: AZ400K:H_2O (1:3) for 60 s (or until the pattern is clear)
- Post-develop Bake: 110 C for 600 s

Appendix 2: Methods to Reduce Dark Current in $Al_{0.7}$InAsSb PIN APDs

A2.1 NH_4OH Dip

$Al_{0.7}$InAsSb is the most common material our group uses for APD designs. As such, it would be beneficial for our $Al_{0.7}$InAsSb PIN APDs to have the lowest possible dark current. As the material contains Al, there is likely some surface oxidation on the sidewall that would contribute to an increased surface leakage current. If this oxide layer could be removed, the surface leakage component of the dark current could be reduced. I figured a finished sample could be dipped in a solution to remove the surface oxide. I started by dipping the sample in a 10% Buffered Oxide Etch (BOE) solution for various times. However, the BOE only increased the dark current by several orders of magnitude.

From my time as an undergraduate researcher at the University of Delaware, I remembered we had some success with reducing dark current in InGaAs/InP photodiodes by dipping the samples in a 5% Tetramethyl Ammonium Hydroxide (TMAH) solution in water. This solution acts as a dilute basic etch. I was discussing this problem with a colleague from another research group here at UVA[b] and he suggested I try using a 29% NH_4OH solution in water. To evaluate the performance, I took a 29% NH_4OH solution and further diluted it in a 1:40 ratio by volume with water. I then dipped some $Al_{0.7}$InAsSb PIN samples in the further diluted solution for 30 seconds. I then compared the dark current of the several devices before and after the NH_4OH dip. The results are displayed in Figure A2.1(a). The dip has clearly improved the dark current of the devices. For the pre-dip curve, there is a slope change in the curve around -22 V, where the dark current starts increasing at a quicker rate. However, in the post-dip curve, the slope appears to remain constant out to around -42 V. Another observation deals with how the two curves appear around device breakdown. The pre-dip curve has a more abrupt breakdown, only starting to curve upward around -45 V. This behavior is characteristic of an abrupt surface breakdown. However, the breakdown for the post-dip curve is smoother, with a gradual breakdown that looks similar to the photocurrent curve. This

[b] I want to acknowledge Chris Moore for suggesting the use of NH_4OH.

smooth breakdown is characteristic of a bulk region breakdown. Figure A2.1(b) plots the dark current versus gain (left axis) for the pre- and post-dip samples. The pre-/post-dip current ratio is also plotted in Figure A2.1(b) (right axis).

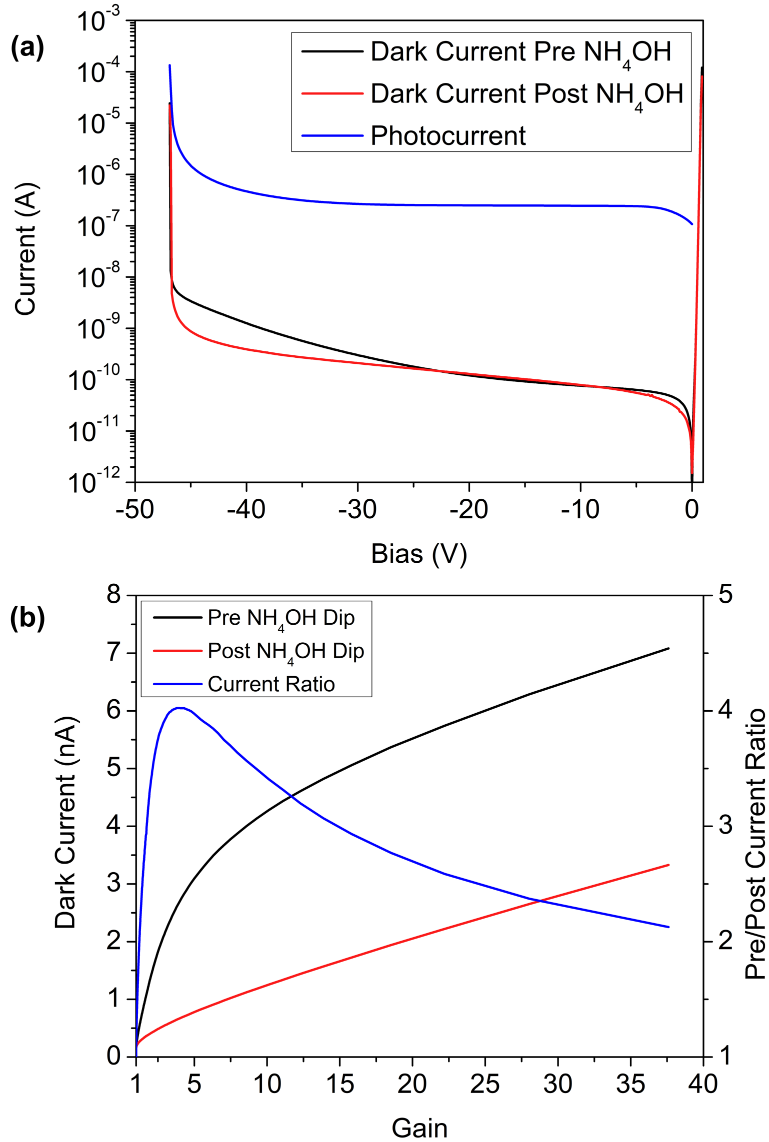

Figure A2.1: (a) The dark current of an $Al_{0.7}InAsSb$ PIN APD before and after a 30-second dip in an NH_4OH solution. Also plotted is the photocurrent under lamp illumination. (b) The dark current versus gain for the $Al_{0.7}InAsSb$ PIN APD before and after the NH_4OH dip (left axis) and the Pre/Post-dip current ratio (right axis).

A2.2 Double Mesa Fabrication

Another method for reducing the dark current in an APD is by implementing a double mesa structure. This method is beneficial for reducing the surface leakage current contribution to the device dark current as the double mesa structure acts to confine the high electric field away from the sidewalls of the structure. Figure A2.2(a) shows a schematic of how a double mesa PIN APD device looks, illustrating the effect of electric field confinement. Figure A2.2(b) shows a 2D electric field profile (simulated with Ansys Lumerical CHARGE) of the device depicted in Figure A2.2(a). The simulation illustrates the confinement of the electric field from the top to the bottom of the depletion region. This structure is achieved by performing two mesa etches. The first etch, with a smaller mesa diameter, is used to etch through the top p-contact, just into the uid region. The second mesa etch, with a larger diameter, is used to etch into the n-contact. By reducing the diameter of the p-contact region, the electric field is confined to the smaller top diameter, greatly reducing the electric field strength near the sidewall of the detector.

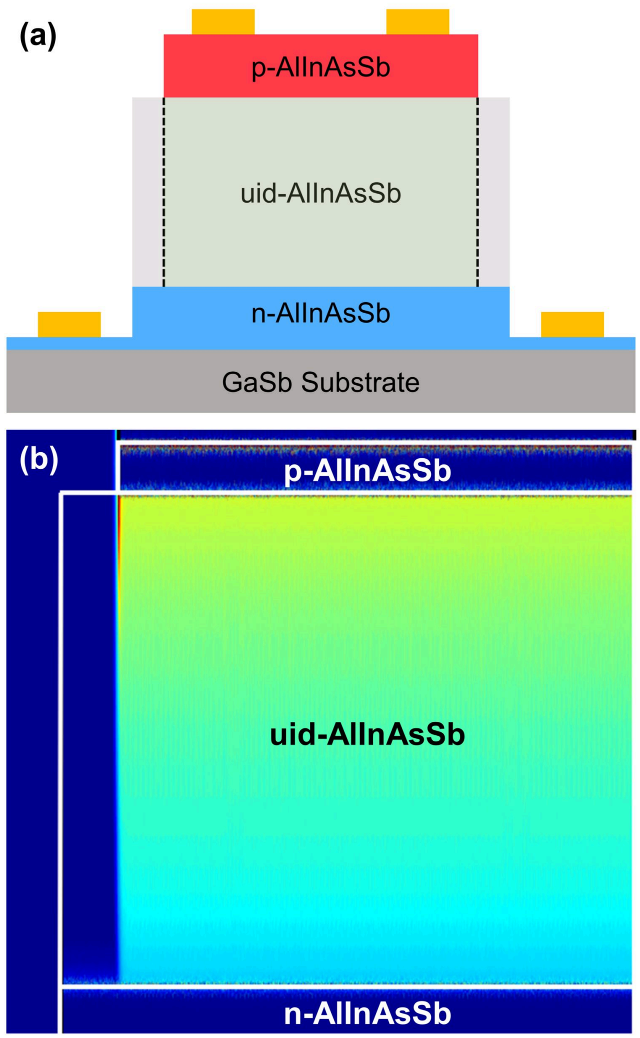

Figure A2.2: (a) Schematic cross-section of a double-mesa PIN APD. (b) The 2D electric field profile, simulated with Ansys Lumerical CHARGE, for the structure depicted in (a).

To illustrate the performance benefit, I took one of our standard 1-µm thick $Al_{0.7}InAsSb$ PIN APD epitaxies and fabricated it as a double mesa. The photomask I used had various bottom mesa diameters (80 µm, 100 µm, 150 µm, 200 µm). For each bottom mesa size, there were several smaller top mesa diameters that reduced in size in 10-µm increments. Figure A2.3 is an I-V for a series of five 150-µm bottom diameter devices. As the top mesa diameter is reduced, the overall dark current also reduces. It is interesting to note that as the top mesa diameter decreases, the slope of the dark current also appears to decrease. To further emphasize this point, Figure A2.4 shows a 100/80-µm and 150/100-µm diameter device plotted together. It is evident that after the device is depleted (~ -3 V), the slope of the 150/100-µm diameter device is much less steep than that of the 100/80-µm diameter device. In fact, at high bias, the 150/100-µm device has a lower dark current than the 100/80-µm diameter device. This implies that the surface current dominates at a higher bias for $Al_{0.7}InAsSb$. The 150/100-µm diameter device has ~60% more bulk area compared to the 100/80-µm diameter device, yet it has a lower dark current.

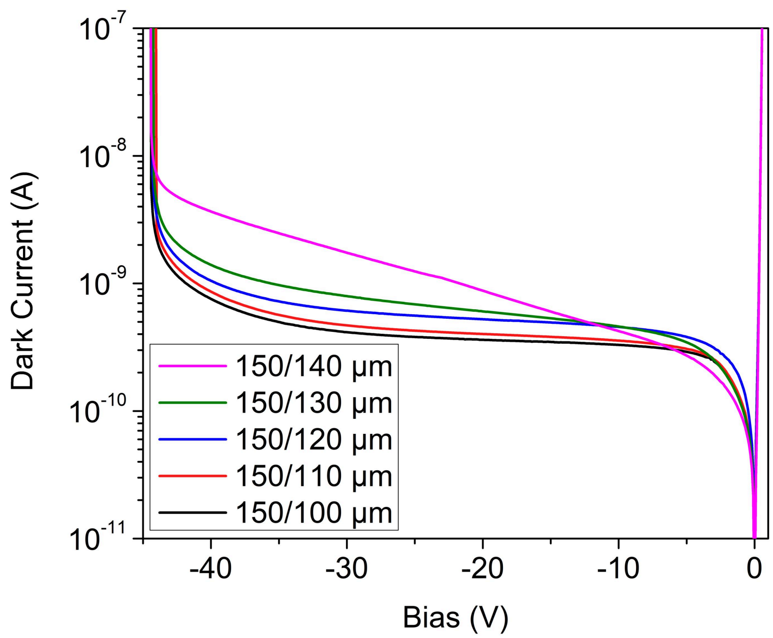

Figure A2.3: The current-voltage characteristic for a series of 150-µm bottom diameter devices.

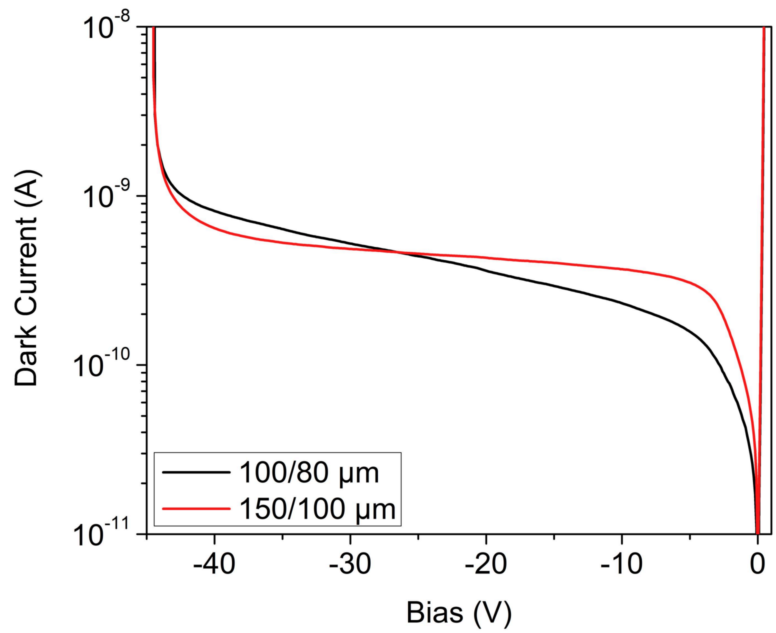

Figure A2.4: The current-voltage characteristic for a 100/80-µm and 150/100-µm diameter device.

As a final comparison, Figure A2.5 shows the dark current versus gain for three devices. The blue curve represents a "standard" fabrication run, a single-mesa structure with SU-8 photoresist to protect the sidewalls. The red curve is a single-mesa device dipped in an NH_4OH solution, as described above. The black curve represents a double-mesa device that was also dipped in NH_4OH. Both NH_4OH-treated devices have lower dark current at a given gain compared to the SU-8 passivated device.

It should be noted that the single-mesa structures used also benefit from a partial electric field confinement away from the sidewalls. During the wet etching, the single-mesa samples are beveled because the top GaSb capping layer, usually present in our devices, etches faster than the AlInAsSb layers. At the top of the device, the electric field spans the entire diameter of the device, but toward the bottom, the electric field becomes gradually confined away from the sidewall. Figure A2.6(a) shows a more accurate schematic cross-section of a $Al_{0.7}InAsSb$ PIN APD device. Figure A2.6(b) shows a 2D electric field profile (simulated with Ansys Lumerical CHARGE) of the device depicted in Figure A2.6(a). The simulation illustrates the gradual confinement of the electric field from the top to the bottom of the depletion region. Devices with more anisotropic etches, forming straight sidewalls, will have a high electric field at the sidewall throughout the entire length of the depletion region, leading to potentially large surface leakage currents. Compared to a beveled device, straight sidewall devices are more likely to benefit from a double-mesa structure due to their electric field confinement away from the sidewall.

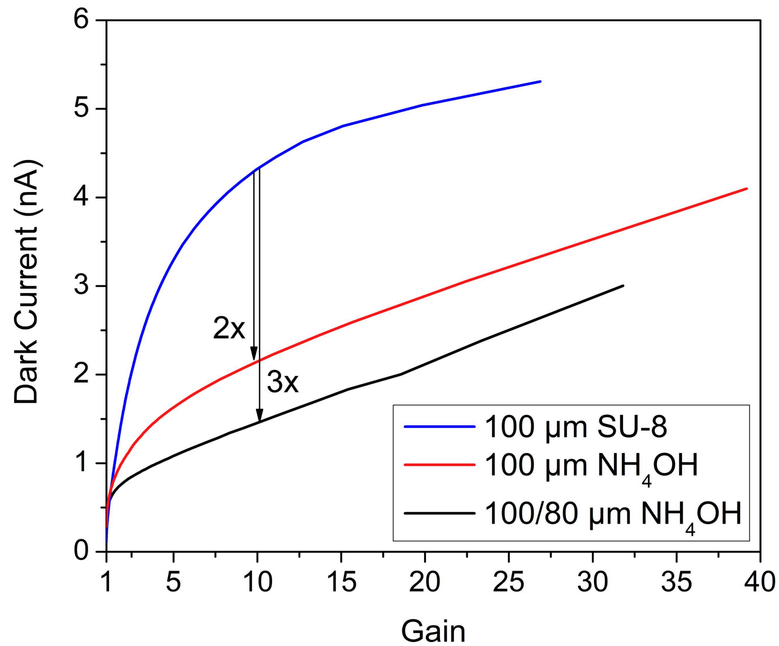

Figure A2.5: The dark current versus gain for three $Al_{0.7}InAsSb$ PIN APD devices. Two single-mesa devices, one with a traditional SU-8 surface passivation (blue) and one dipped in an NH_4OH solution (red), and one double-mesa device also dipped in an NH_4OH solution (black).

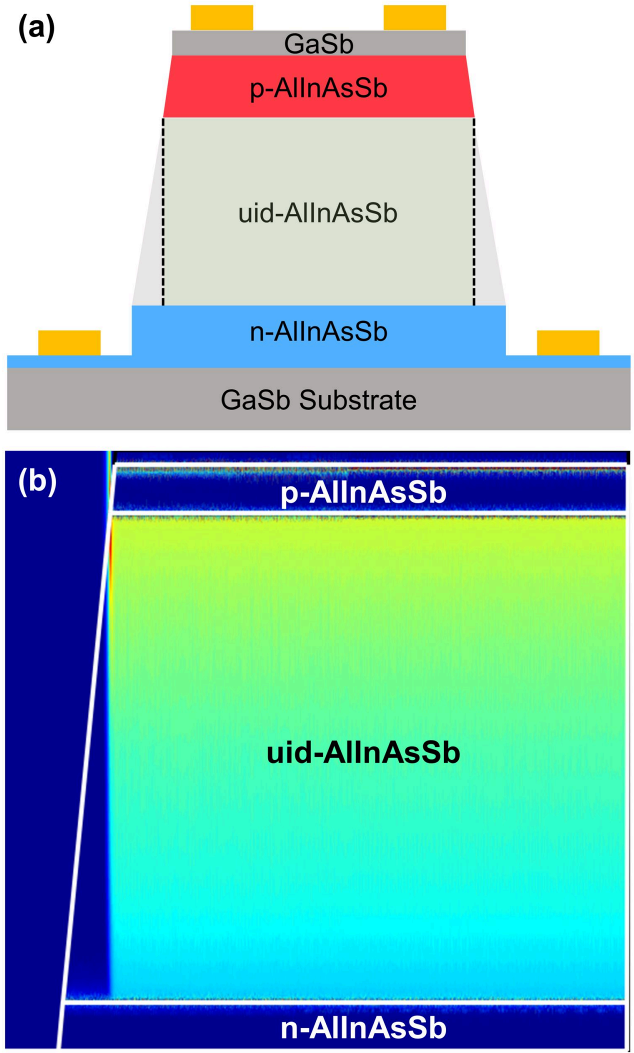

Figure A2.6: (a) The schematic cross-section of a beveled single-mesa PIN APD. (b) The 2D electric field profile, simulated with Ansys Lumerical CHARGE, for the structure depicted in (a).

Appendix 3: Troubleshooting the Low-frequency Noise Setup

A3.1 From Room Temperature to 240 K

Considerable steps were taken to enable the low-frequency noise setup to work in our cryogenic chamber. For the 2- and 3-step staircase devices and the cascaded multiplier device, the low-frequency setup at room temperature was sufficient as their dark current was low enough not to saturate the TIA. However, the 2-step SACMcase would need to be measured at lower temperatures (240 K) to ensure the dark current was low enough not to saturate the TIA.

A3.1.1 Room Temperature Setup

Figure A3.1(a) shows the physical room-temperature low-frequency noise measurement setup depicted in Figure 2.4(b). The TIA is the black box at the bottom of the image, and the SourceMeter is at the top. The SA is not depicted, but it is connected to the output of the TIA, coming out of the bottom of the image. The GS probe used has an SMA connection, so it was connected to a breakout cable to separate the positive and negative signals. It should be noted that the breakout cable was kept short to limit additional noise in the system. Figure A3.1(b) shows a cable grounding the workbench. The inset shows the plug end with only the ground pin. It is crucial for the workbench to be grounded! Without a grounded workbench, RF interference in the lab will dominate the noise floor of the SA, making it impossible to measure the noise of the DUT. It is also essential to ensure the SourceMeter is set to high accuracy mode! Under normal accuracy, the SourceMeter generates enough RF interference to dominate the noise floor of the measurement setup.

Figure A3.2 shows an image of the noise floor of the measurement setup without a device connected. The center frequency is ~69 kHz with a resolution bandwidth of 47 Hz. From many rounds of testing, I found that a noise floor of less than -110 dBm was sufficient to perform the low-frequency excess noise measurements for all devices mentioned in this thesis. Therefore, if I could achieve a noise floor of -110 dBm or lower when measuring in the cryogenic chamber, I would be confident in the sensitivity of the system.

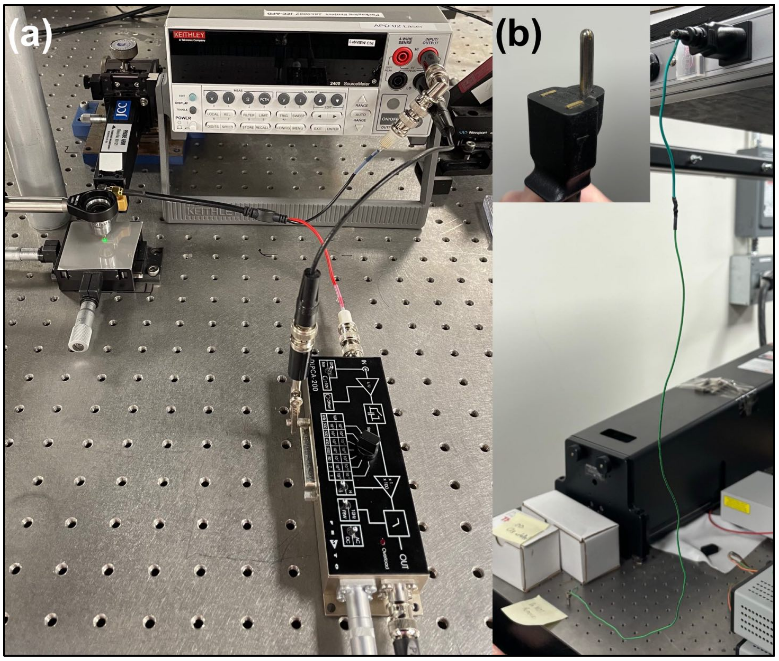

Figure A3.1: (a) The room-temperature low-frequency noise measurement setup. The spectrum analyzer is not depicted. (b) An image of the grounded workbench with an inset showing the plug end connected to the wall.

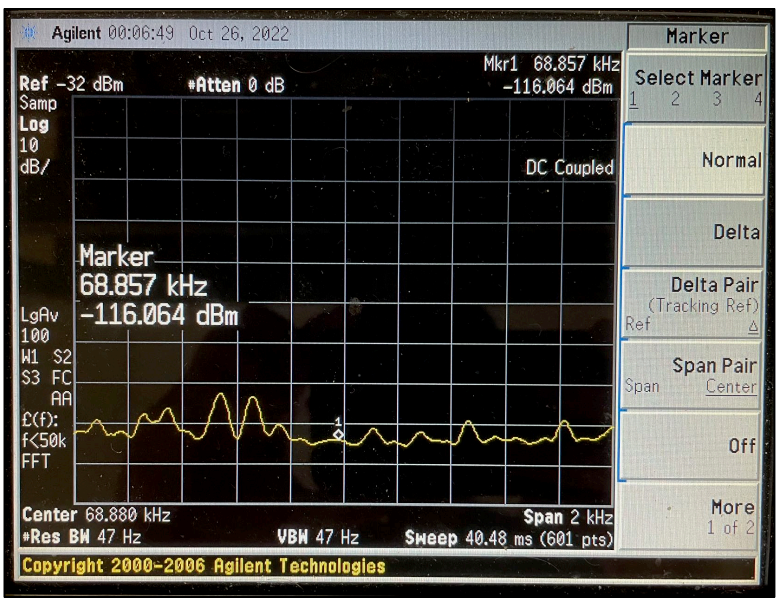

Figure A3.2: An image of the noise floor at a center frequency of ~69 kHz with a resolution bandwidth of 47 Hz.

A3.1.2 Cryogenic Chamber Setup

To start, I simply moved the components of the low-frequency setup to our cryo chamber. I wanted to see the noise floor of the setup without any modifications. Figure A3.3 shows the noise floor. In the initial measurement, there are two big problems. One, the noise floor shows repeated ripples, likely indicating some RF interference. Two, the noise floor is around -98 dBm, too high to measure the excess noise of a device. After much trial and error, I discovered that the physical location of the cryo chamber was the problem. I had the SourceMeter, TIA, and SA into a power strip. Depending on which wall the power strip was plugged into, the noise floor in the setup would drastically change. Also, I found that the chamber needed to be grounded, like the workbench, to reduce RF interference. To solve the problem, I physically moved the cryo chamber from its workbench to the same workbench used for the room-temperature low-frequency noise measurements.

Figure A3.4 shows an image of the cryogenic-temperature low-frequency noise setup. The layout is effectively the same as for the room-temperature version, except that there is an additional grounding line that connects the cryo chamber to the common ground of the outside of the TIA case. The TIA is elevated on a wooden box because the SMA breakout cable was too short to connect the GS probe to the TIA sitting on the workbench. After all modifications, the cryogenic setup, as depicted in Figure A3.4, achieved a noise floor of about -110 dBm, as shown in Figure A3.5. At this point, the setup was ready to test on known working devices to confirm its capabilities.

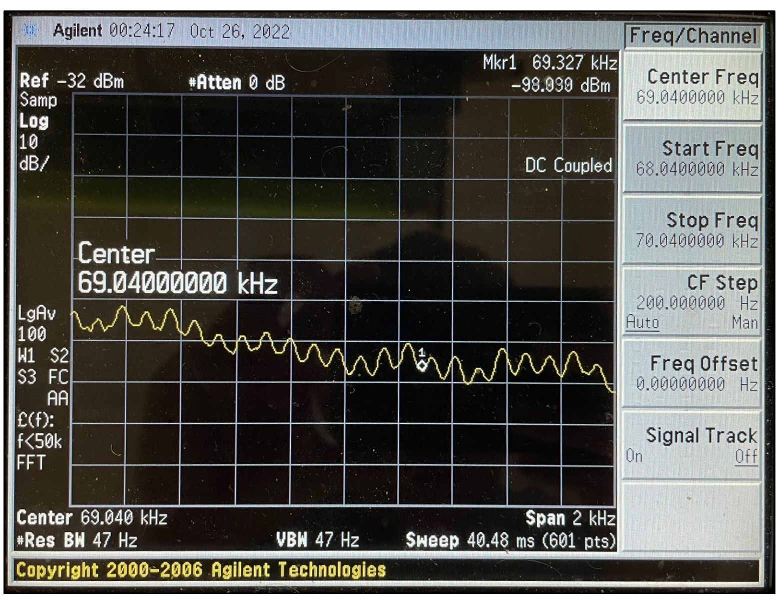

Figure A3.3: The noise floor of the low-frequency setup attached to the cryo chamber without any modifications.

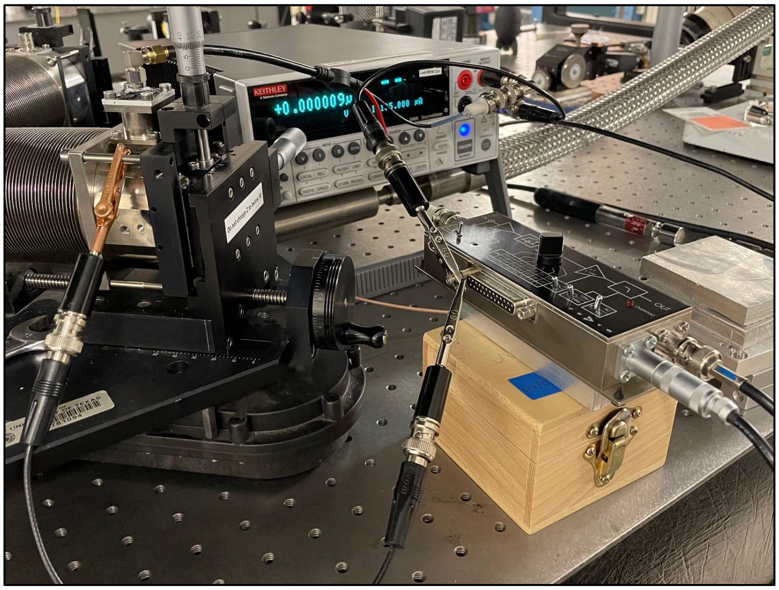

Figure A3.4: The cryogenic-temperature low-frequency noise measurement setup.

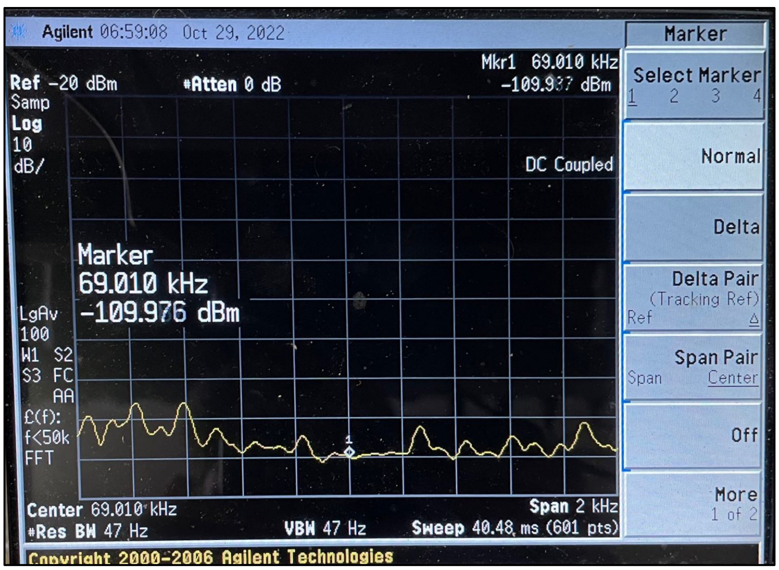

Figure A3.5: The noise floor of the cryogenic-temperature low-frequency noise measurement setup after it was moved to the same workbench as the room-temperature setup.

A3.2 Testing the Setup in the Cryogenic Chamber

To test the viability of the setup, I first decided to measure the noise power of a simple PIN APD at low bias where there is unity gain and unity excess noise. The measurement was performed at atmosphere and room temperature. The noise was measured at an operating frequency of ~70 kHz and a resolution bandwidth of 39 Hz. The results of the measurement are displayed in Figure A3.6. Like the staircase and SACMcase measurements presented above, the noise power containing the dark and photocurrent contributions is plotted in black, and the photocurrent-only contribution is plotted in red. A clear linear relationship is present, meaning the setup in the cryo-chamber is sensitive enough to measure the noise of DUT correctly.

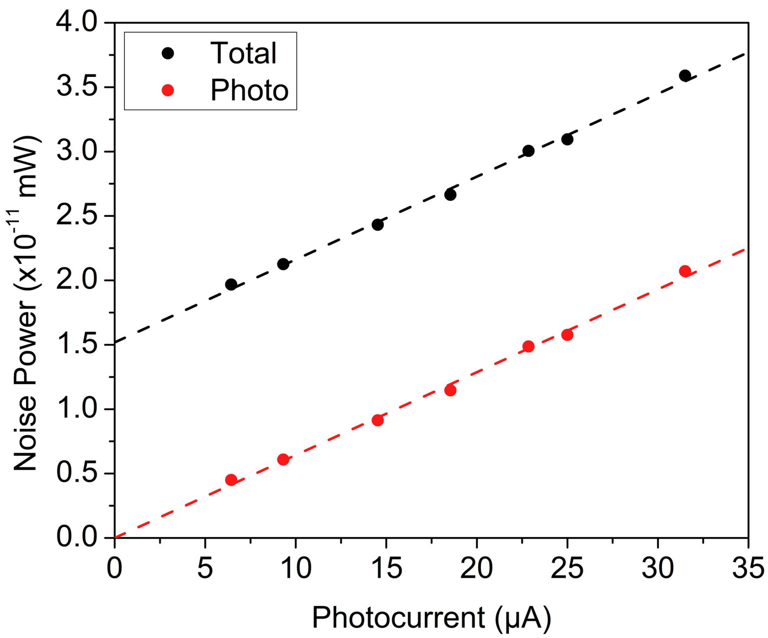

Figure A3.6: The measured noise power versus photocurrent of a PIN APD at low bias with unity gain and unity excess noise using the cryogenic-temperature low-frequency noise measurement setup. The black points represent the photo and dark current contributions, whereas the red points represent only the photocurrent current contribution.

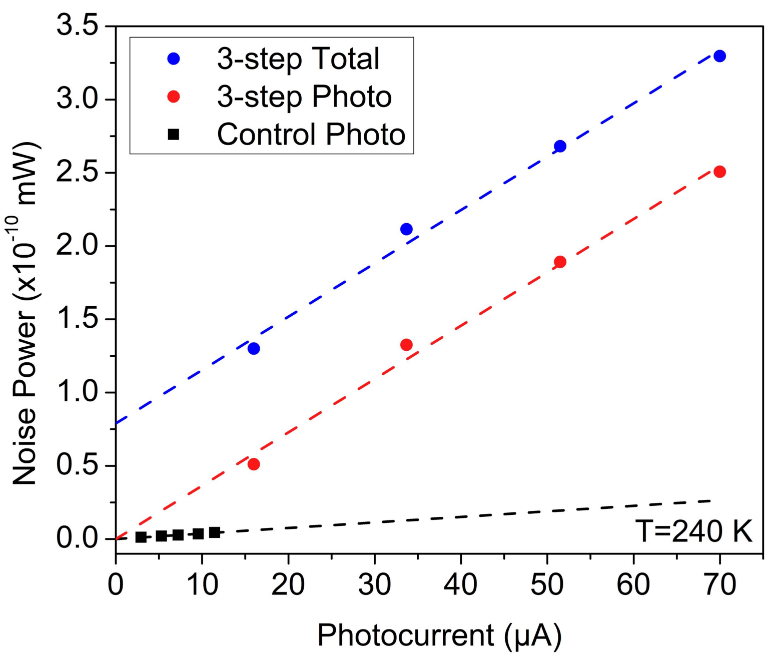

Figure A3.7: The measured noise power versus photocurrent of the 3-step staircase and its control at 240 K measured using the cryogenic-temperature low-frequency noise measurement setup.

The final test was to measure a staircase APD structure. I selected the 3-step staircase APD. The measurement was performed at 240 K under a pressure of less than one mTorr. Like the PIN APD, the 3-step staircase APD was measured at an operating frequency of ~70 kHz with a resolution bandwidth of 39 Hz. The measurement technique was the same as presented in the Excess Noise of Staircase APDs chapter, where the control was measured alongside the 3-step device to serve as a measured value for the unmultiplied shot noise power. The measurement is displayed in Figure A3.7 and looks very similar to the ones performed in the Excess Noise of Staircase APDs chapter at room temperature. Figure A3.8 shows the measured excess noise factor for three 3-step devices. The results are similar to those found at room temperature. The slight increase in noise is likely attributed to the slightly higher than 2^N gain measured in the devices. With successful measurements of a standard PIN APD and a 3-step staircase APD, I was confident the cryogenic-temperature low-frequency noise measurement setup was ready to measure the excess noise of a 2-step SACMcase APD.

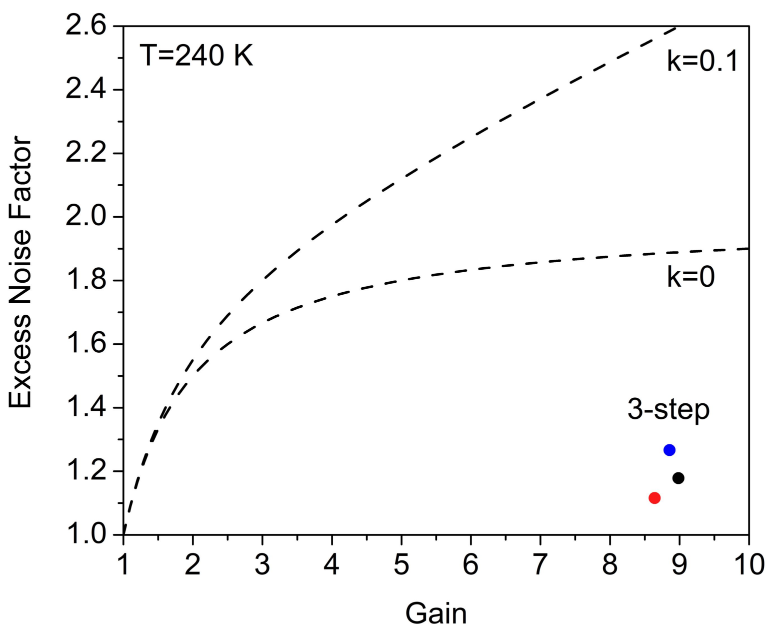

Figure A3.8: The measured excess noise factor of the 3-step staircase APD measured at 240 K in the cryogenic-temperature low-frequency noise measurement setup. Reference lines for k=0 and k=0.1 are included.

Appendix 4: SEM Images

Below are a few scanning electron microscope (SEM) images I took throughout my time at UVA. I have included these images because I think they look cool and display a level of detail unobtainable with light-based microscope imaging. All SEM images were taken using the Zeiss GeminiSEM 560 inside the UVA Innovations in Fabrication (IFAB) facility.

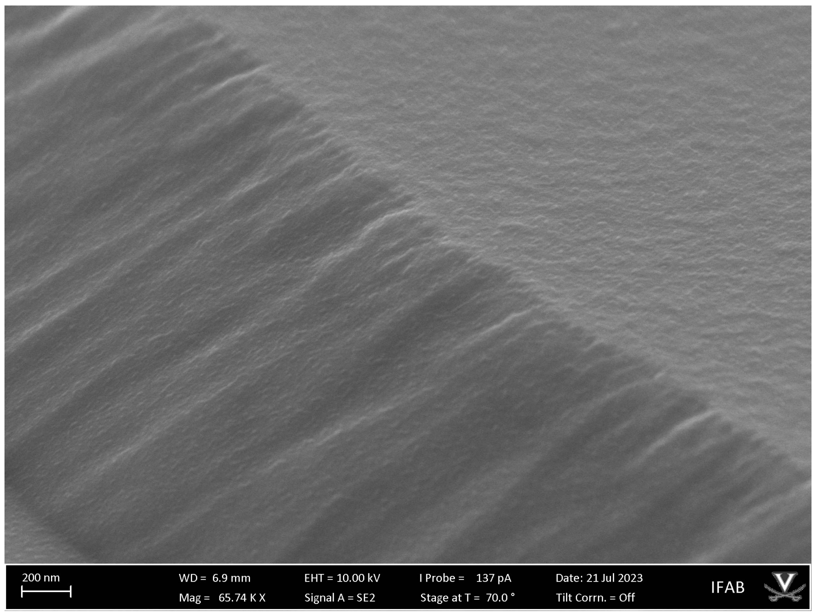

The sidewall of an etched circular mesa after it was dipped in an NH_4OH solution.

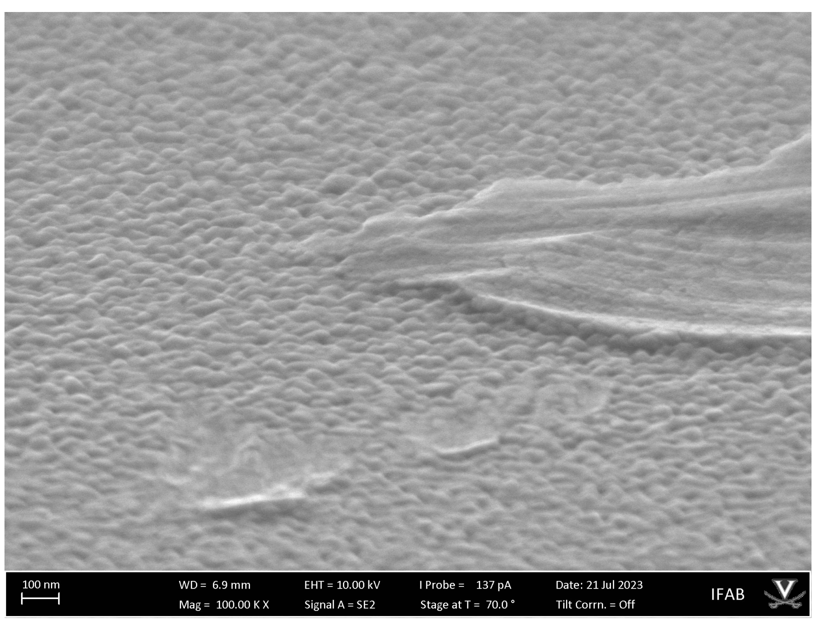

Electron-beam evaporated gold. To the naked eye this is a mirrored surface. The scratch mark was left by a 5-µm tipped tungsten needle probe used to test devices.

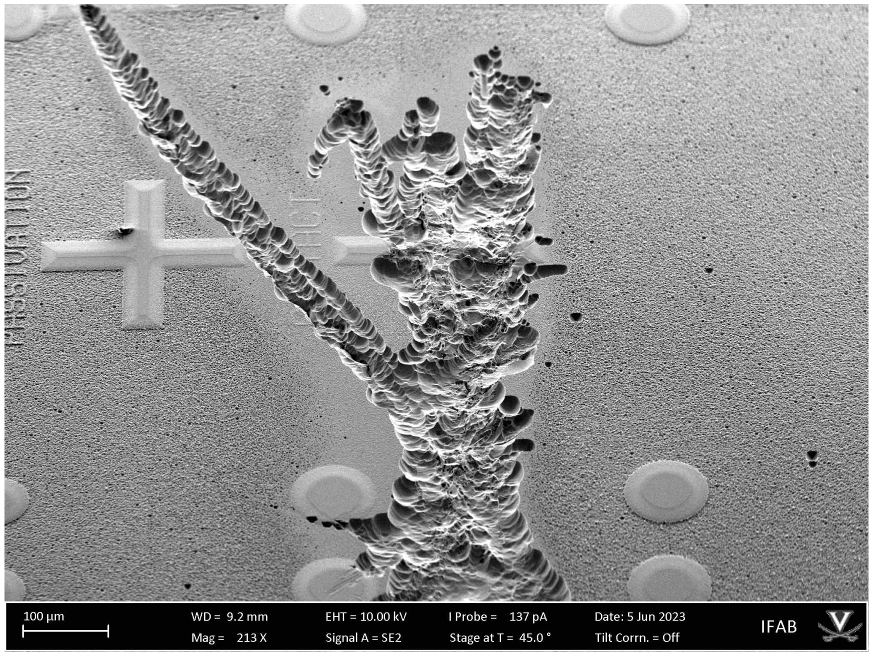

The surface of a semiconductor after being scratched with a diamond tipped scribe.

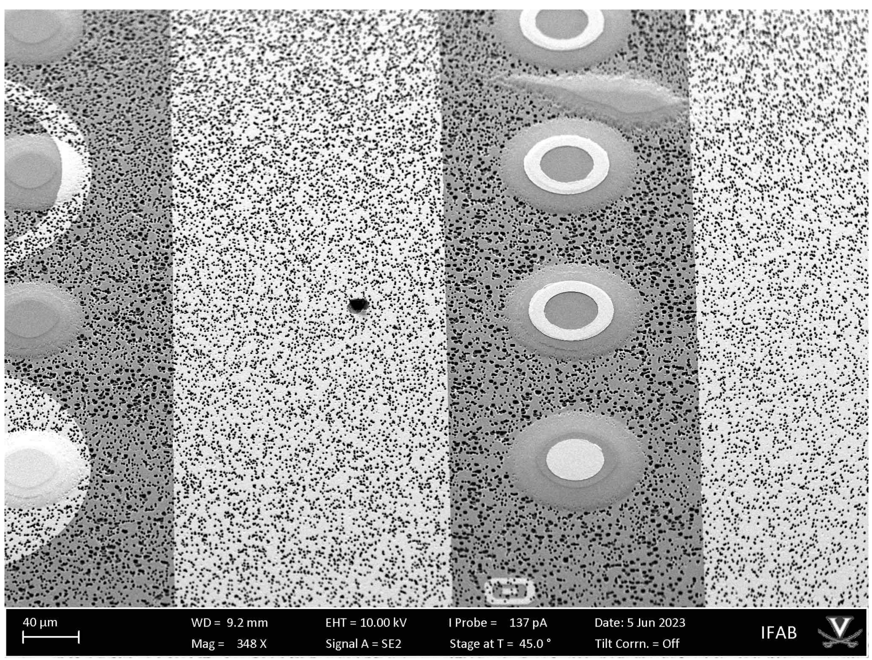

The surface of a semiconductor with many point defects (black dots).

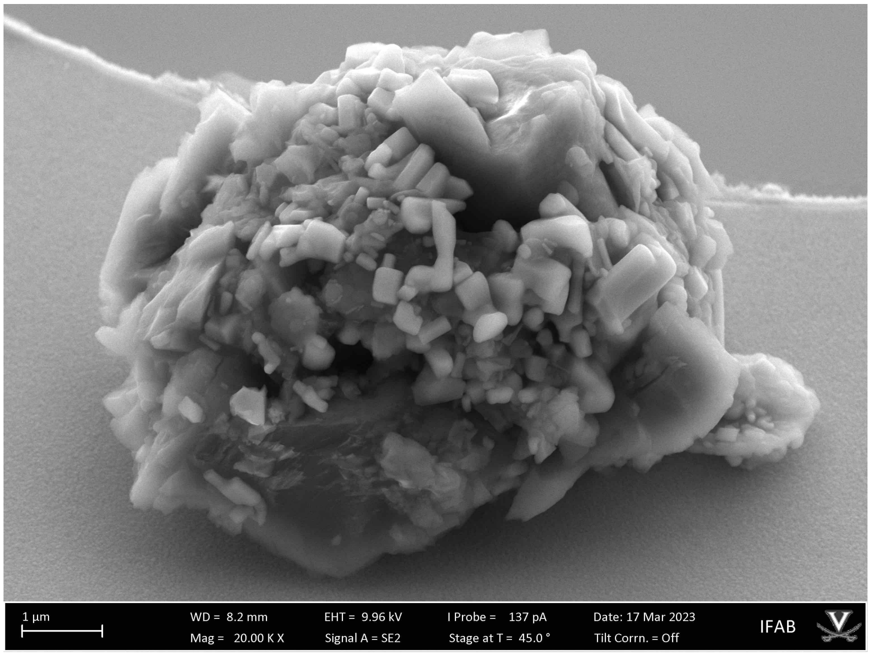

A piece of debris found on the surface of a device.

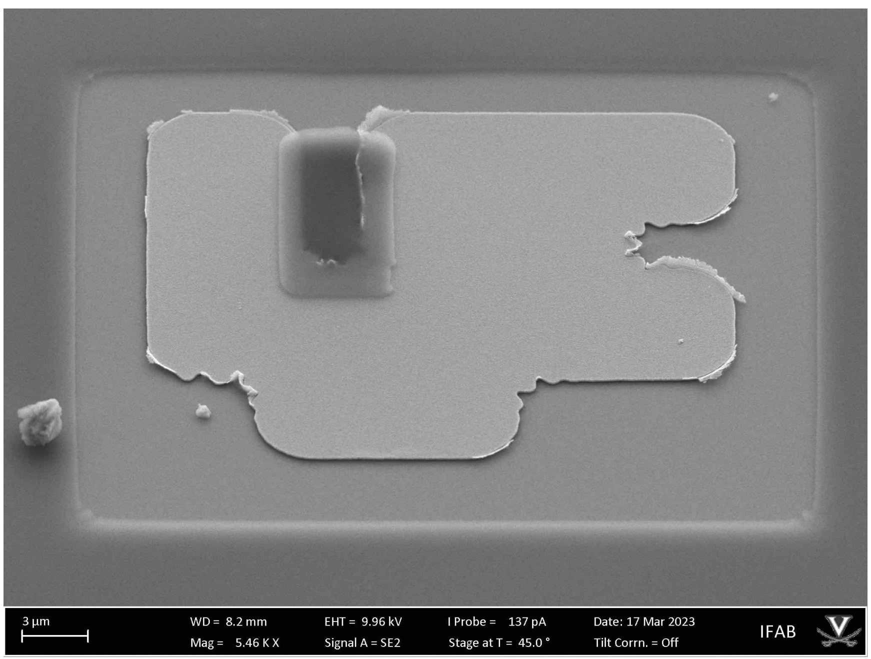

A suspicious character from a popular videogame.